Experimental Investigation of Photocatalytic Hydrogen Production with Boron-doped TiO_2 and Multi-Walled Carbon Nanotubes-TiO_2

by

Celile Zeynep Demir

A Thesis Submitted in Partial Fulfillment

of the Requirements for the Degree of

Masters of Applied Science

in

The Faculty of Engineering and Applied Science,

Mechanical Engineering Program

University of Ontario Institute of Technology

Oshawa, Ontario, Canada

April 2019

THESIS EXAMINATION INFORMATION

Submitted by: **Celile Zeynep Demir**

Master of Applied Science in **Mechanical Engineering**

Thesis title: Experimental Investigation of Photocatalytic Hydrogen Production with Boron-doped TiO_2 and Multi-walled Carbon Nanotube-TiO_2

An oral defense of this thesis took place on April 8, 2019 in front of the following examining committee:

Examining Committee:

Chair of Examining Committee	Dr. Martin Agelin-Chaab
Research Supervisor	Dr. Ibrahim Dincer
Examining Committee Member	Dr. Dipal Patel
External Examiner	Dr. Ahmad Barari

The above committee determined that the thesis is acceptable in form and content and that a satisfactory knowledge of the field covered by the thesis was demonstrated by the candidate during an oral examination. A signed copy of the Certificate of Approval is available from the School of Graduate and Postdoctoral Studies.

Abstract

This thesis investigates photocatalytic hydrogen production by performing an experimental study using a small-scale photochemical cell which splits water to hydrogen and oxygen by UV light irradiated boron-doped TiO_2 and carbon nanotube-TiO_2 semiconductor photoelectrodes. The average current densities generated under potentiostatic scan for uncoated stainless steel, boron-doped TiO_2 and carbon nanotube-TiO_2 working electrodes are observed to be 112.51 mA /cm^2, 128.43 mA /cm^{2,} and 164.73 mA /cm^2 under UV light respectively. Although amount of hydrogen produced by carbon nanotube-TiO_2 is higher than boron-doped TiO_2, boron-doped TiO_2 has the maximum energy and exergy efficiencies. Moreover, in this study, alternative reactor designs are proposed and simulated on COMSOL Multiphysics software in order to improve the flow of the hydrogen bubbles inside of the reactor. The simulation results showed that the amount of hydrogen at the beginning for the three designs $1.19\ cm^2$ drops to $0.078\ cm^2$ which shows 32.5% improvement and $0.0581\ cm^2$ which represents 34.9% improvement in hydrogen released compared to the base design for first and second proposed designs respectively.

Keywords: Solar energy; Photocatalytic hydrogen production; Photoactive materials; Boron doped TiO_2; Carbon nanotube-TiO_2.

Acknowledgments

First and foremost I would like to express my sincere gratitude and appreciation to my supervisor Dr. Ibrahim Dincer for his guidance and helpful advice during my research. This work wouldn't have been possible without his continuous motivation and support.

I would like to thank all my colleagues in the ACE 3030b lab and CERL; Aida Farsi, Anwar Hammad, Arda Yapicioglu, Burak Yuzer, Eren Sevinchan, Farid Safari, Ghassan Chehade Huseyin Karasu, Haris Ishaq, Khalid Altayed, Mohammed Ra'fat,, Magd DinAli, Murat Emre Demir, Osamah Siddiqui, Oznur Kayhan and Sherif Seif Eldin for their support and advice during my studies. I am extremely grateful for Maan Al-Zareer, Ahmed Abdel Rahman, Ahmed Hasan, and Ahmed Hasan's lovely family that have become my family and support system here and being always there for me.

I have special friends to thank; my best cheerleaders Zeynep Kuyumcu and Zisan Koker, Feyza Avcilar, Halenur Evrendilek, Neslisah Gundogan and Seda Yuksel who have been motivated me throughout my research work at a distance.

I am very lucky for having such a big and lovely family; Ufuk Demir, Bahar Demir, Fatih Demir, and Nazli Tuna Demir, my most profound love and deepest thanks are always to them, their love, blessing and endless support was the only encouragement for me to stick on the tasks of my research. My aunts Emine Comert Meral Okyar and Zuhal Yukselen, being far away was never a barrier for us, I love you guys so much and thank you for being my best friends forever. Finally, I would like to express my deep thanks to my grandparents: Arif Comert, Kevser Comert, Latif Demir and particularly Nermin Demir who I lost recently, this thesis is dedicated to you all.

Table of Contents

List of Tables

List of Figures

Nomenclature

A	Area (m^2)
E	Energy (kJ)
Ex	Exergy (kJ)
ex	Specific Exergy (kJ/kg)
$\dot{E}x$	Exergy Rate (kW)
$\dot{E}xd$	Exergy Destruction Rate (kW)
F	Faraday constant (9.6485 × 104 C/mol)
g	Specific Gibbs Free Energy (kJ/kg)
h	Specific Enthalpy (kJ/kg)
H	Enthalpy (kJ)
I	Current (A), Irradiance (W/m^2)
LHV	Lower heating value (kJ)
m	Mass (kg)
$\dot{m}$	Mass Flow Rate (kg/s)
M	Molar mass (g/mol)
N	Number of moles
$\dot{N}$	Molar flow rate, mol/s
P	Pressure (kPa)
Q	Heat (kJ)
$\dot{Q}$	Heat Rate (kW)
q	Electrical charge (A s)
T	Temperature (°C or K)

TW	Terawatt
t	Time (s)
v	Velocity (m/s)
V	Voltage
W	Work (kJ)
$\dot{W}$	Work rate (kW)

Greek letters

Δ	Change
η	Energy efficiency
λ	Wavelength (nm)
ρ	Density (kg/m^3)
ψ	Exergy efficiency

Subscripts and Superscripts

d	Destruction
EC	Electrochemical cell
en	Energy
ex	Exergy
in	Input flows
o	Ambient
s	Source
out	Output flows

Acronyms

CE	Counter electrode
CERL	Clean Energy Research Laboratory

GHG	Greenhouse Gas
Mtoe	Million tonnes of oil equivalent
OCP	Open circuit potential
PEC	Photoelectrochemical
PEM	Proton Exchange Membrane
PV	Photovoltaic
RE	Reference electrode
SMR	Steam Methane Reforming
SS	Stainless steel
WE	Working Electrode

Chapter 1: Introduction

Energy is an essential necessity for modern societies as it provides main uses such as industrial processes, transportation, mechanical power, electricity, heating, and many other activities. Increasing global energy demand due to industrial development and rapid population growth is one of the major reasons for a fossil fuel crisis. In 2040, global energy consumption rate will be 17866 million tonnes of oil equivalent (Mtoe) which is reported as 13511 Mtoe in 2017 and 8565 Mtoe in 1995 [1]. Additionaly, in the same report it is reported that expected share of renewables is 29% in 2040 which is 7 times higher than the percentage in 2017. Correspondingly, net CO_2 emissions (Gt of CO_2) is reduced from 33.4 to 18.0 between 2017 and 2040. This clearly indicates that the rising need of renewable and sustainable alternatives to fossil fuels is more acute and urgent to be able to meet with energy demand as well as to find a potential solution to environmental problems related to the consumption of nonrenewable energy resources.

1.1 Energy and Environmental Issues

Demand and the consumption of energy have been rapidly increasing over the years as a consequence of the population growth, urbanization, and economic development. Based on International Energy Agency Key World Energy Statistics 2018 report, world's total primary energy supply was 13761 million tonnes of oil equivalent (Mtoe) which is two times more than the total primary energy supply in 1973 with 6034 Mtoe [2]. In Figure 1.1, the world's primary energy supply values are given in 2004, 2008, 2012 and 2016. There is a continuous increase in total energy supply, almost 83% of it provided by fossil fuels.

On the other hand, energy supplied from renewable energy sources such as geothermal, solar, wind, heat, etc. has an increasing trend over the years. Furthermore, total CO_2 emission from oil, natural gas, and coal is 99.3% of the world's CO_2 emissions from fuel combustion in 2016 [2]. By reason of the fact that current fossil fuel resources are not expected to be available in sufficient amount to satisfy the rising energy demand and their high carbon emission rates, renewable based clean energy generation and other low carbon options should be considered to fulfill the need.

At this point, hydrogen comes into prominence as an alternative since it has significant advantages compared to other options fossil fuels with being energy carrier and storage medium and producible with zero greenhouse gas emissions using renewable energy resources [6, 7]. Hydrogen is the simplest, most abundant and lightest element in the periodic table which can be stored and used in various applications. Because hydrogen is not available by itself in nature, most of the hydrogen is generated by gasification and steam reforming using coal, oil and natural gas fossil fuels as primary energy resources. Furthermore, hydrogen can be generated by nuclear power and environmentally friendly renewable energy resources such as geothermal, biomass, solar, wind, hydro, waves and etc. [6].

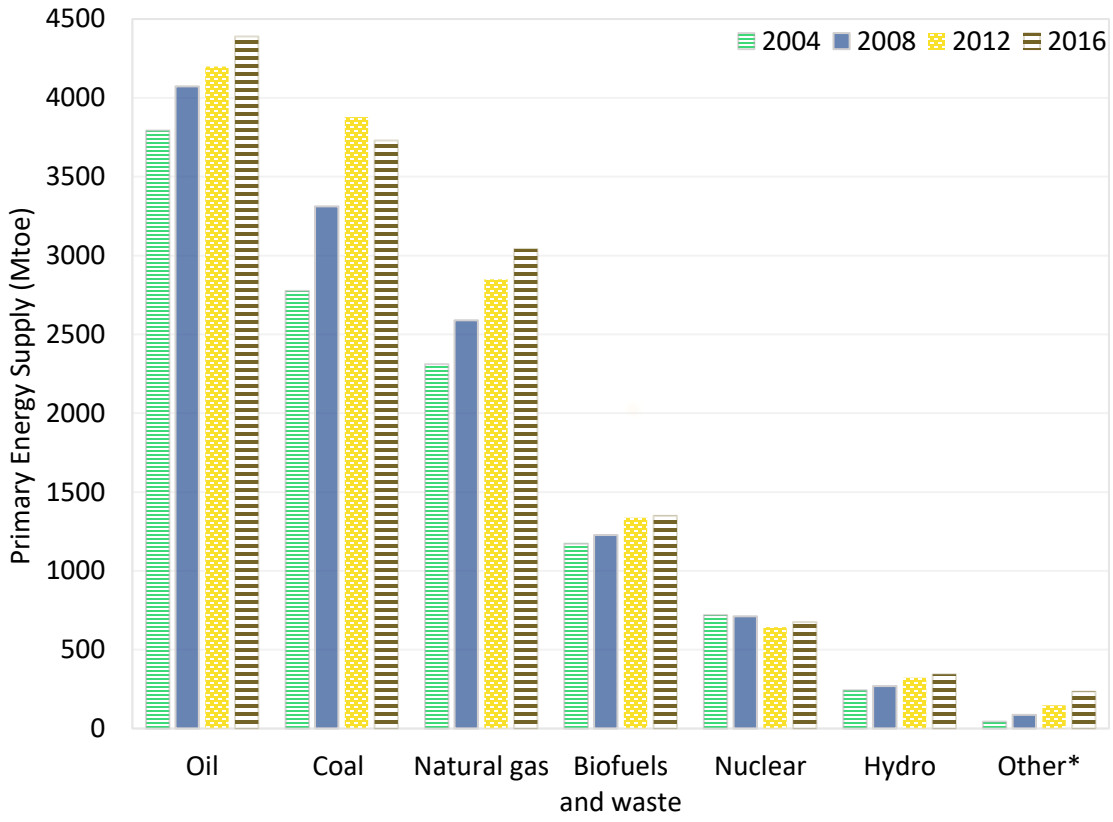

Figure 1.1 Comparative total primary energy supply values of the world in 2004, 2008, 2012 and 2016 (*includes geothermal, solar, wind, tide/wave/ocean, heat, etc.) (data from [2-5]).

Regarding renewable energy options, solar based hydrogen production one of the promising approaches to meet growing energy demand for energy since it is abundant and

sustainable energy resource and independent from issues related to region limitations. The amount of solar energy from the sun that earth receives about 3.9 x 10^{-24} MJ per year which is 10,000 times more than the world consumes in a year [8].

There are several hydrogen production methods from solar energy such as photolysis, photoelectrochemical, photocatalytic water splitting, PV electrolysis, etc. Hydrogen is easy to access and safe option when it is generated by solar water splitting because water is a clean, renewable and affordable hydrogen resource. Among these methods, photocatalytic hydrogen production via water splitting has been becoming crucial and widely studied in the literature since it needs two sources which are most available sources in the world and it has a simple process and no GHG emission [9]. For this reason, photocatalytic hydrogen production is seen as an answer to an economic and environmental problem caused by fossil fuels [9].

Photocatalytic hydrogen production requires sunlight and photocatalyst for water splitting where photons have greater energy than the band gaps of the photocatalyst for electron-hole pair generation. Most of the catalysis needs higher energy by reason of their band gap which means they can only be used solar spectrums with high energy portions [9]. Cost reduction and improvement in efficiency already have high importance for renewable energy production methods to become prominent [10] and what is more that because of the reason mentioned above, photocatalytic hydrogen production should be studied with searching for possible photocatalysts which have better conductivity, stability and efficiency and low cost [9].

1.2 Motivation

Growing energy demand and fulfilling the need with fossil fuels give rise to global warming by increasing carbon emissions. Searching out for possible solution by taking being environmentally friendly, cleanliness, renewability, and efficiency into consideration lead up to the motivation of this study which is improving the photocatalytic hydrogen production via water splitting, doping photoactive material TiO_2 with boron and carbon nanotubes in order to increase photocatalytic activity of the photoelectrode.

1.3 Objectives

The main objectives of the thesis are doping TiO_2 to enhance the photo-activity of the material and modify the electronic properties which are used to perform experiments to produce clean hydrogen by water splitting via solar energy. The specific objectives of this research are as follows:

- To design three electrode photochemical cell with graphite counter electrode, Ag/AgCl reference electrode and coated stainless steels as working electrodes for photocatalytic hydrogen production system which allows semiconductor surfaces to absorb solar energy and perform a chemical reaction and collect evolved H_2 and O_2 gases in different tubes
- To obtain two different photocatalysts boron and carbon nanotube TiO_2 by the sol-gel method the with the same molar ratio for fair comparison and coating stainless steels with these two photocatalysts to increase visible light photo-activity of TiO_2.
- To perform cyclic voltammetry, electrochemical impedance spectroscopy, chopping, and chronopotentiometry electrochemical analyses of the developed systems to be able to understand the resistance mechanism inside the cell and assess the system performance and produce hydrogen using the coated stainless steels.
- To perform energy and exergy analyses of the developed photocatalytic hydrogen production system to measure system performance in terms of energy and exergy efficiencies.
- To model and simulate the base design of the photoelectrochemical reactor which is used for previous researches in Clean Energy Research Lab (CERL) and then propose alternative reactor designs to simulate, analyze generated hydrogen bubbles behaviors with two-phase flow.
- To highlight the key findings in the experimental work and reactor designs and simulations, then recommend possible further research for hydrogen production.

Chapter 2: Literature Review

A detailed literature review on clean hydrogen production methods is comparatively provided and discussed in this chapter. First of all, an overview of possible hydrogen production methods are given and the subject is narrowed down the scope of solar hydrogen production studies. Afterward, photocatalytic hydrogen production is introduced and examples from the literature with different types of electrolyte and semiconductor materials are provided to obtain their effects on hydrogen production performance.

2.1 Hydrogen Production Methods

Human being is dependent on energy to maintain their lives for products they use, industries, housing and everything related to meet the need with their high standard lives. Hydrogen energy comes to the forefront as a potential solution to current issues related to energy transformation and usage since most of the energy systems generate harmful gases which have an effect on global climate change. Rising energy demand causes an increase in greenhouse gases (GHG) emissions in the atmosphere. Green hydrogen production is an active research area which can remove the possible environmental damages of the fossil fuels based energy production. Awad and Veziroglu specified that hydrogen has an advantage of cost-effectiveness, low transportation cost and being efficient and environmentally friendly compared to fossil fuels [11].

Green hydrogen can be produced by nuclear energy and energy recovery from industrial waste using thermal and electrical energy. Also, renewable energy resources such as wind, hydro, ocean thermal and tides and waves can be used for electrical energy to produce hydrogen. Solar energy can be used for hydrogen production using thermal, electrical, biochemical and photonic energy to produce green hydrogen. Geothermal and biomass are also available for hydrogen production. It is also possible to use different energy forms together as a hybrid method (electrical + photonic, electrical + thermal etc.) [12]. Some of the hydrogen production methods are given in Table 2.1. As an example of hybrid methods, Zamfirescu and Dincer [13] introduced a system which uses the heat generated by engine/fuel cell to produce hydrogen from Ammonia. Balta et al. [14] have investigated a geothermal hydrogen production system which includes high-temperature

steam electrolysis and came to the conclusion that efficiency of the system differs with the temperature of the geothermal inlet. In another research, Balta et al. [15] have identified geothermal hydrogen production methods working with relatively low thermochemical and hybrid cycles. Overall system efficiency of the cycles are higher than 50% and the copper-chlorine cycle is the most promising one.

Table 2.1 Classification of some of the green hydrogen methods with brief explanation (Modified from [12, 18]).

Driving Energy	**Hydrogen production method**	**Resource**	**Description**
Electrical	Electrolysis	Water	Water splitting into O_2 and H_2 by giving a current
Thermal	Thermolysis	Water	Water splitting by steam which has a minimum temperature of 2500 K
Thermal	Thermochemical	Water	Water splitting by multiple steps of chemical reactions such as Cu-Cl and S-I cycles
Thermal	Thermochemical	Biomass	Thermo-catalytic conversion of biomass such as wood sawdust and sugar cane
Photonic	PV – electrolysis	Water	Electricity generation by PV panels to run an electrolyzer
Photonic	Photo-catalysis	Water	Catalysts usage water splitting
Photonic	Photo-electrochemical	Water	Electrochemical cell usage to generate electricity which drives the water splitting process
Biochemical	Dark fermentation	Biomass	Anaerobic fermentation under no light condition
Photonic + biochemical	Bio-photolysis	Biomass and water	Bacteria and microorganisms are used

Gandia et al. [16] studied green and renewable hydrogen production-related issues such as purification, storage, and safety. They pointed out that water splitting with high temperature might be the most efficient technology but researches face some challenges related to the material used for electrolysis. Nikolaidis and Poullikkas [17] have compared 14 different hydrogen production methods from a technical and economical point of view. They found out that although SMR is the most cost-effective production method, green hydrogen production processes can dominate fossil fuel energy resources with

development in storage and transportation of H_2. Also, they demonstrated that thermochemical gasification and pyrolysis have economic advantages among the other processes and they are capable to compete with fossil fuel-based methods. Dincer et al. [18] have reviewed and compared sustainable hydrogen production methods based on energy and exergy efficiencies, production cost, global warming potential, the social cost of carbon and acidification potential and they have concluded that among the photonic energy based hydrogen production methods photocatalysis has highest ranking because of its low production cost.

2.2 Solar Hydrogen Production

There are various ways to use solar energy to produce hydrogen which can be mainly collected under four types: photovoltaic (PV), photobiological, photo-electrolysis and thermal energy [19]. Photobiological, photovoltaic and photo-electrolysis are low-temperature applications while thermal energy can be utilized in both low and high-temperature applications [19]. Classification scheme can be seen in Fig. 2.1 which is given with a detailed explanation below.

Photovoltaic electrolysis is a hydrogen production method that uses electricity produced by PV cells for water electrolysis to generate hydrogen and oxygen as the end products. System needs are PV panels, electrolyzers, power unit and storage for H_2 produced [20]. Although it has an advantage of zero GHG emission during the process, because the setup needed for PV electrolysis is costly, further research is a necessity [19]. There are many research available in the literature [21-23], as well as PV integrated system analysis. Yilanci et al. [24] has analyzed PV-hydrogen fuel cell hybrid system using different paths and found that the system's max overall energy and exergy efficiencies 9.7% and 9.3% respectively. Hogerwaard has integrated production of PEC H_2 and PV electricity by single solar source using a spectrum-splitting mirror where PEC reactor has 71.5% overall energy efficiency and 69.7% overall exergy efficiency [25].

The concentrated thermal energy has several methods for solar based hydrogen production both from fossil fuel and renewable options. Thermolysis is basically thermal decomposition of water in a single step with a temperature source above 2500 K.

Thermochemical cycle is another approach using metal oxide redox reaction which doesn't need an extra high temperature step to separate H_2 and O_2 gases because they are formed in different steps [19]. High-temperature electrolysis by thermal energy has the capability of high production rate compared to low-temperature electrolysis since the high temperature of the cell cause an increase in the amount of water split. Additionally, running the high-temperature electrolysis in the steam phase gives considerably higher thermal efficiencies of 40-50% [28]. Ozturk et al. have thermodynamically analyzed the solar based multi-generation system which generates hydrogen by high-temperature steam electrolysis, hot water, cooling, heating with an exergy efficiency of 57.35 % [29]. Steinfeld [30] has produced hydrogen from solar water splitting with two-step thermochemical cycle which hydrogen and oxygen generation occurs in different steps in order to reduce the process for high-temperature gas separation.

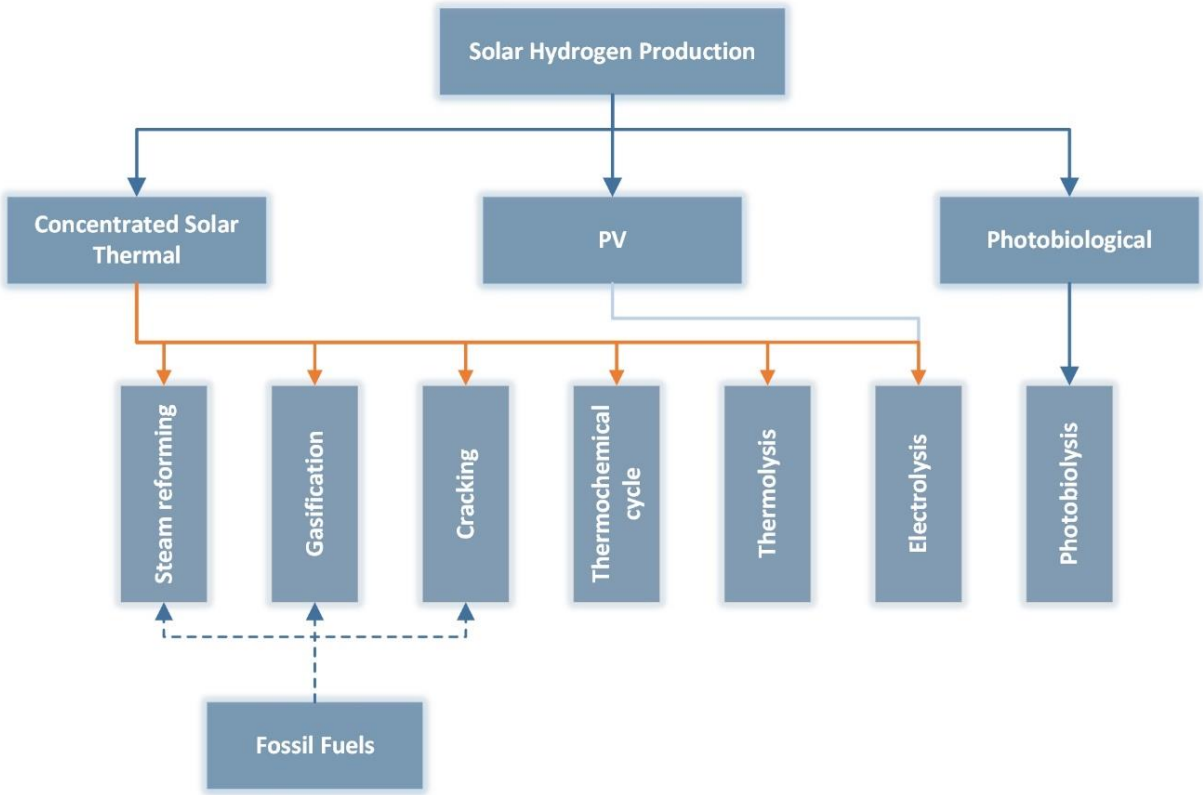

Figure 2.1 Solar hydrogen production methods (Modified from [19]).

Photo-biological hydrogen production uses solar energy and microorganisms to obtain final by-product H_20 to convert into hydrogen. The process still has some challenges

and under development for improvement in bio-reactors, culture resistance to stress conditions and feedstock availability and cost [31, 32].

2.3 Photocatalytic Hydrogen Production by Water Splitting

Photonic energy from solar sources can be used for photocatalysis and photoelectrochemical hydrogen production methods. In photocatalytic hydrogen production, photocatalyst particles prepared from semiconductor material inside the cell starts generating electrons and holes by excited band-gap in the conduction and valence bands. These created carriers drive reduction and oxidation reactions. Alternatively, in photoelectrochemical hydrogen production, semiconductor coated electrodes can be placed in the electrolyte solution in an electrochemical cell where electrolyte solution transfers accepted electrons from a semiconductor electrode while the Fermi level of the semiconductor material is lower than the reduction potential of the electrolyte [33]. The water splitting reaction from solar energy can be written as follows:

$$H_2 0 + hv \rightarrow H_2 + \frac{1}{2} O_2 \, , \Delta G = 238 \frac{kj}{mol}$$

The three major steps for photocatalysis on semiconductor materials are [34]:

1. Absorption of photons (hv) with energy that's more than the semiconductor bandgap which causes the generation of electrons (e^-) and hole (h^+) pairs on the semiconductor
2. Transportation of the photo-generated and excited carriers on the semiconductor.
3. Chemical reactions occur on the surface between the carriers and $H_2 0$.

In addition, to be able to split water efficiently, there are various key criterions [35]:

- Generating sufficient voltage for water splitting by semiconductor material,
- Having a narrow band gap value to absorb a high portion of the solar spectrum,
- Band edge potentials should straddle the hydrogen and oxygen redox potential levels,
- The photochemical system components should have long term stability to prevent corrosion in the electrolytes,

- Between the surface of the semiconductor material and electrolyte, the charge transfer should be easy to keep energy loses at the minimum and be selective for hydrogen and oxygen evolution reactions.

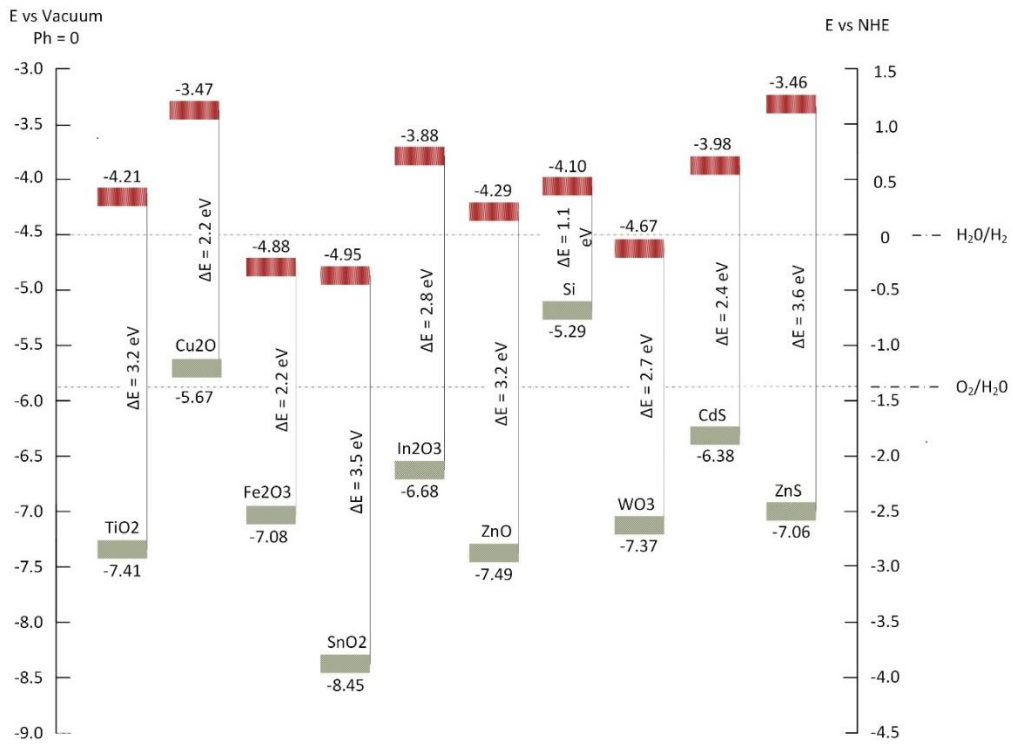

Figure 2.2 Band edges positions (conduction lower and valence top) and bandgap values of the several semiconductor materials (Modified from [36, 38]).

The band edges positions (green color for the valence band and red color for the conduction band) and bandgap energies (electron volts) of the several semiconductor materials at pH 0 are given in Figure 2.2 taking the normal hydrogen electrode (NHE) and the vacuum level as a reference. Theoretically, water dissociation needs minimum band gap energy of 1.23 eV, conduction band position should be higher than the redox potential of hydrogen and valance band position should have a lower value than the oxidation potential of water [39] which are shown in Figure 2.2.

Photocatalytic hydrogen production using semiconductor materials has attracted attention since it has great potential for clean H_2 production by water splitting using solar energy. Brattain and Garrett [40] measured the potential between p-type and n-type germanium in different electrolytes in 1954. Fujishima and Honda [41] have started the

emerging trend in TiO_2 photocatalyst based hydrogen production after their work on photoelectrochemical hydrogen production by water splitting using solar energy in 1972. The research on several photoactive materials and their properties, characterization, and applications for water splitting under UV and visible light illumination has gained attention and prominence from then on.

Zamfirescu et al. [42] have reviewed several photoelectrochemical and photocatalytic systems comprehensively. Acar et al. [9] have compared the 49 chosen TiO_2 based photocatalysts available in the literature, in terms of hydrogen production rate per unit area and per unit mass of photocatalyst. Hydrogen production rate based on per mass is the highest for Au-TiO_2 with 7200 µmol H_2/h g catalyst while Bi-$NaTaO_3$ has the lowest rate with 0.86 µmol H_2/h g. On the other hand, hydrogen production rate based on per area is the highest for Au-CdS with 472.26 µmol H_2/h m^2 catalyst while Sb_2TiO_5 has the lowest rate with 0.33 µmol H_2/h m^2 catalyst. Ni et al. [43] have presented a review to compile the latest developments using TiO_2 on photocatalytic hydrogen production and they found that implementing metal-ion and dye sensitization increase activation of TiO_2 in UV light. Fujishima et al. [44] have reviewed TiO_2 photocatalysis and studied TiO_2 related surface and they came to the conclusion that beside the sample's natural characteristics, the preparation method, handling, storage, chemical, and physical features should be explained because these are all significant to understand the behavior of the material during the experiments. According to Li et al. [45], the photoelectrochemical performance of the photoelectrodes can be improved using doping materials to increase absorbed UV light if the semiconductor has a wide bandgap. They also state that nanostructured photoelectrodes have an advantage of shortened transfer time and enhanced light absorption.

Boron-doped TiO_2 and hydrogen production using it as a photocatalyst first studied by Moon et al. [46] using the sol-gel method to obtain B-doped TiO_2 powders. They have found that photocatalytic activity was much higher when the light irritation given from the top instead of the bottom and photocatalytic activity of TiO_2 was increased by boron modification. There are many types of research on photocatalytic activity of boron-doped TiO_2 nanoparticles [47, 48] and nanotubes [49-52] prepared by various methods such as chemical vapor deposition, sol-gel, dip coating in the literature. Good stability,

enhancement in the UV light activity, lower band gap energy are some of the highlighted common results of the experiments with boron doped TiO_2. Zaleska [53] has reviewed heterogeneous photocatalysis, dopants, preparation and doping methods for doped titanium dioxide and mentioned that the main problem with nonmetal doped TiO_2 such as boron doped TiO_2 is that photocatalytic activity is lower under visible light compare to UV light.

Recently, there is substantial attention has been given to semiconductor and carbon nanotube-based materials. Since the generation and transportation of the electrons are easier, the lifetime of generated electron and hole pairs is longer. Xu et al. [54] proposed a new wet impregnation method for TiO_2/MWCNT nanocomposite which is simpler than the available methods in the literature. Shahrezai et al. [55] have presented TiO_2/MWCNT for wastewater treatment and they found out the photocatalytic activity of TiO_2 and the removal efficiency increased when carbon nanotube ratio is increased because CNT can absorb organic molecules and it has a good capability of charge separation. Nguyen et al. [56] studied photocatalytic properties of TiO_2 CNT Nano-hybrid material and they indicated that photocatalytic activity of the Nano-hybrid is better to compare to pure TiO_2 and CNT. They obtained the highest results with a ratio of 5 to 1 [TiO_2/CNT] due to electron-hole recombination fast which increases the photon absorbed.

Moreover, there are many review papers on photoreactors and photocells for water splitting since reactor design has significant importance to increase efficiency. Xing et al. [57] have summarized some of the photoreactor designs for both photocatalytic and photoelectrochemical water splitting and indicate that the three electrodes photoelectrochemical reactor is the best configuration for lab scale research. They also find it crucial to state that it is an urgent need to standardize the evaluation methods and decrease the production cost of the photoreactors. In addition, according to Minggue et al. [58], because the geometry of the photoreactor is usually built based on photoelectrode assembly, it is difficult to design an efficient and stable photoreactor. Their opinion is that the ideal design should consider the management of the produced gases and movement of the ions during the water splitting.

2.4 Main Gaps in the Literature

Throughout the literature review, it has seen that there are quite a few reviews and studies which mainly focus on the development of alternative photocatalyses and features of the semiconductor materials for water splitting [59]. However, very few studies are actually using existing semiconductors and previously proposed photocatalyses and preparation methods for photocatalytic hydrogen production.

During the investigation of hydrogen production with CNT-TiO_2 nanocomposite, the photocatalyses are synthesized by hydration and dehydration techniques and hydrothermal process and used as a photocatalytic reactant solution in the literature [60, 61]. Also, Carmichael et al. [62] have performed photocatalytic water splitting with boron doped TiO_2 which is obtained by chemical vapor deposition using photodiode. In both cases, electro-analysis techniques are not applied to understand the mechanism of the chemical reactions within the cell. This study aims to generate CNT-TiO_2 and B doped TiO_2 coated stainless steels with using the sol-gel method and dip coating for both photocatalyses and perform electroanalytical methods to investigate the mechanism of the chemical reactions inside the cell.

Additionally, based on the literature review, only a few researchers have included the design of the PEC reactor in terms of how generated hydrogen bubbles travel, how and where exactly the hydrogen bubbles accumulate within the reactor. Carver et al. [63] are one of the researchers that have considered the design of the PEC reactor. However, in their work, the simulation is based on the continuous flow of the electrolyte in order to understand the flow pattern is uniform inside the reactor. In this thesis work, the novel designs of PEC reactor are simulated considering the hydrogen bubbles' flows and collection by using two-phase flow phenomena.

Chapter 3: Experimental Apparatus and Procedures

In this chapter, the experimental setup is explained with the apparatus and procedures used during the experiments.

3.1 Experimental System Description

Figure 3.1 is given as a representation of the system components of the experiments, carried out at the Clean Energy Research Laboratory (CERL) in UOIT, compose of a photochemical cell, a solar simulator, a potentiostat/galvanostat and a software controlled by a computer. A solar simulator is used as a light source which provides photon energy for excitation of the electrons on the surface of photoelectrode in photochemical cell. The cell is consist of electrolyte, counter electrode, working electrode and reference electrode where all the electrodes are connected to potentiostat to be able to measure the voltage/current. Finally, potentiostat is connected to the computer to be able to control the system and analyze the obtained data.

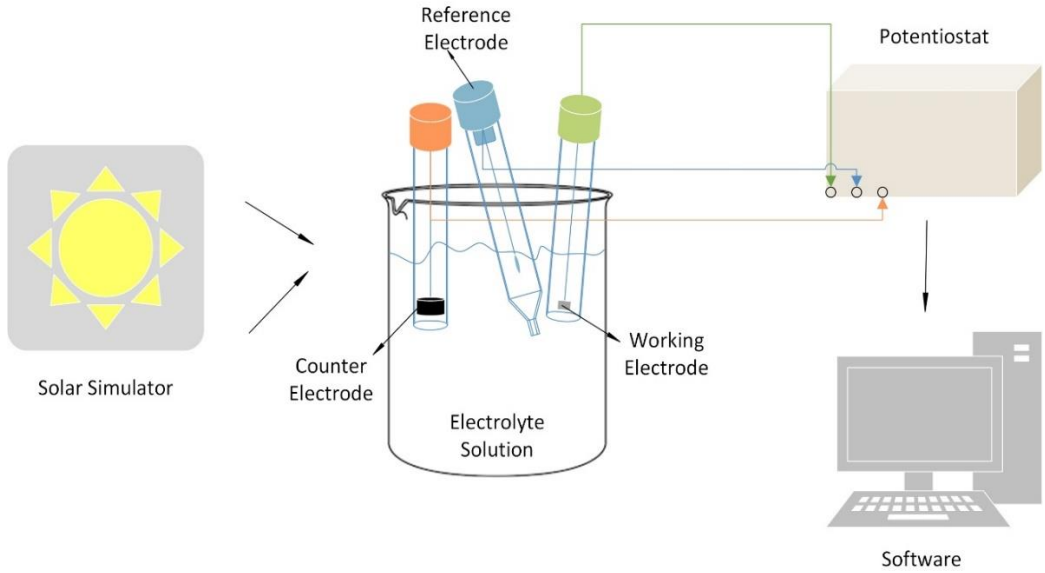

Figure 3.1 System description of the experimental setup.

3.2 Photocatalysis Preparation

In this section, the followed methodologies for preparation of boron and carbon nanotube doping of TiO_2 and coating of the stainless steels plates are given and explained.

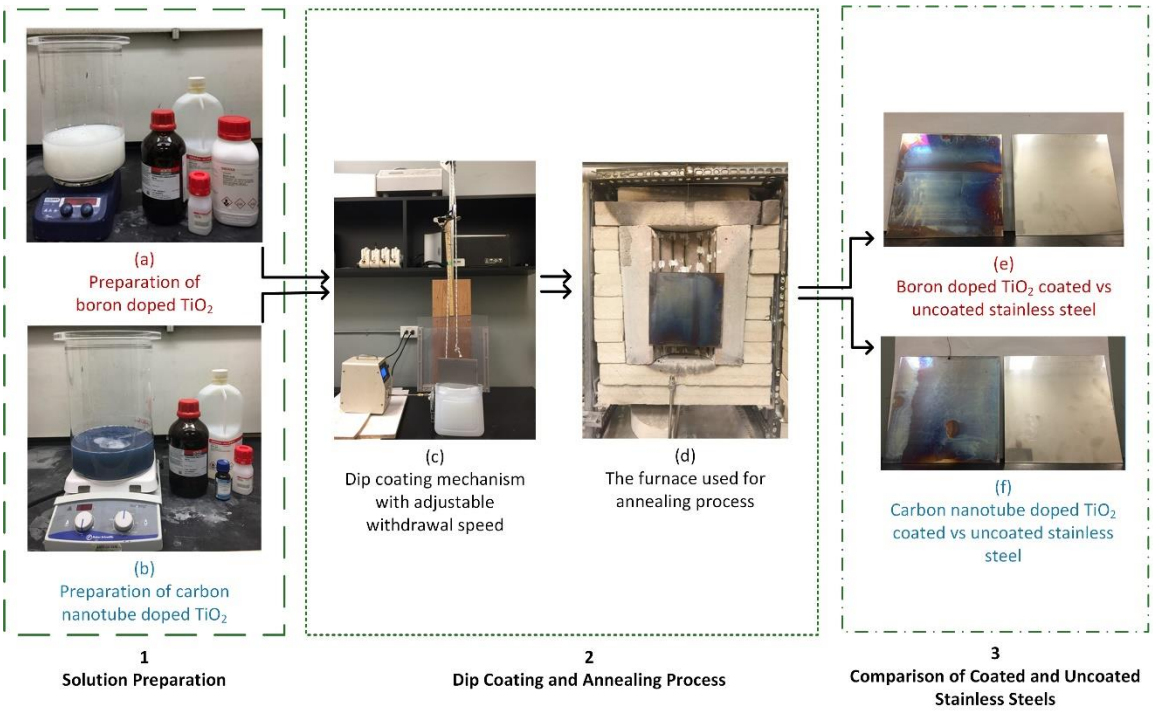

Figure 3.2 The process of solution preparation, coating and annealing for boron doped TiO_2 and carbon nanotube-TiO_2.

3.2.1 Boron-doped TiO_2

Boron-doped TiO_2 is prepared with sol-gel method using Titanium (IV) isopropoxide ($C_{12}H_{28}O_4Ti$, 98+%, Acros Organics), acetic acid (HNO_3, ACS reagent, ≥99.7%, Sigma-Aldrich), nitric acid (CH_3CO_2H, ACS reagent, 70%, Sigma-Aldrich), boric acid (H_3BO_3) and isopropyl alcohol. For the preparation of TiO_2 sol-gel, the method presented by Chedade et al. is followed [64]. At first, TiO_2 sol is produced by mixing 1500 ml distilled water with 75 ml Titanium (IV) isopropoxide and 15 ml acetic acid. Then 10.5 ml nitric acid is added to the solution. After the solution is heated and kept the temperature constant at 80 °C for 30 minutes by using a temperature controller, it is stirred at the room temperature for 2 h [64].

In the meanwhile, to be able to obtain boron doping, the process which is studied by Jeong et al. [65] is implemented. 0.393 g boric acid is dissolved in 100 ml isopropyl alcohol via magnetic stirrer. Boric acid-isopropyl alcohol mixture is added to TiO_2 sol-gel and it is stirred for 2 h to obtain B-doped TiO_2 [65]. Figure 3.2 (a) shows boron doped TiO_2 on the stirrer, color it takes after 2 hours and chemical used for the preparation.

As a next step, a custom-made dip coating machine with adjustable withdrawal speed which is available in the lab for previous researches [66] is used for dip coating as shown in Figure 3.2 (c). Before applying boron doped TiO_2, stainless steel is waited in 1 molar sulfuric acid for half an hour and washed with distilled water. Cleaned stainless steel plate is coated with a withdrawal speed 2.5 mm/s by dipping 100 times, washed with distilled water again and left for drying for 2 h at room temperature.

Lastly, the coated stainless steel is put in the temperature controlled furnace for annealing process for 3 hours as shown in Figure 3.2 (d). The initial temperature of 50 °C is raised by 15 °C/min to 500 °C. In Figure 3.2 (e), the surface difference between uncoated and boron doped stainless steel after the annealing process can be seen.

3.2.2 Carbon nanotube TiO_2

Carbon nanotube TiO_2 is synthesized by sol-gel method. First of all, following by previously mentioned process [64], TiO_2 sol is produced by mixing 1500 ml distilled water with 64 ml Titanium (IV) isopropoxide ($C_{12}H_{28}O_4Ti$, 98+%, Acros Organics), and 13 ml acetic acid (HNO_3, ACS reagent, ≥99.7%, Sigma-Aldrich). Then 9 ml nitric acid is added to the solution. After the solution is heated and kept the temperature constant at 80 °C for 30 minutes by using a temperature controller, it is stirred at the room temperature for 2 h [64].

Another solution is prepared based on Akhavan et al. [67] with 3 ml nitric acid (CH_3CO_2H, ACS reagent, 70%, Sigma-Aldrich) and 0.5 g CNT (multi-walled carbon nanotube powders of 95% purity) and added dropwise to 10 ml ethanol (Reagent Alcohol, LabChem) TiO_2 solution. After the solution was stirred for 4 h, it was left for 24 h at the room temperature of 22 °C (as seen in Figure 3.2 (b)). For dip coating and annealing processes, above-stated steps in boron doped TiO_2 preparetion part are followed with the difference of that CNT-TiO_2 stainless steel is heat treated in the furnace at 450 °C. The final form of the coated stainless steel is presented in Figure 3.2 (f).

3.3 Electrochemical Cells

An electrochemical experiment needs various components as shown in Figure 3.1. A potentiostat/galvanostat records the data of the reactions occurring while supplying the need voltage or current. It can be controlled by specific software for the potentiostat in use on the computer. An electrochemical cell body is where current flows between working electrode (WE) and counter electrode (CE) where the reference electrode (RE) is located between them. All electrodes are connected to the potentiostat/galvanostat via different leads. The working electrode may vary and the reference electrode stays stable as a reference to measure the applied voltage. The counter electrode should be chosen from corrosion resistant material such as platinum or graphite.

There are several electrode configurations to perform electrochemical experiments and hydrogen production from water splitting. The basic setup contains two electrodes in electrolyte solution where one or both of them can be photoactive. The electrolyte solution should be transparent which allows light to reach the photoelectrode (WE). Three electrode cells where the reference electrode is included preferred to measure the efficiency of a photon to current [58]. In this work, three electrodes configuration is designed for the experiments.

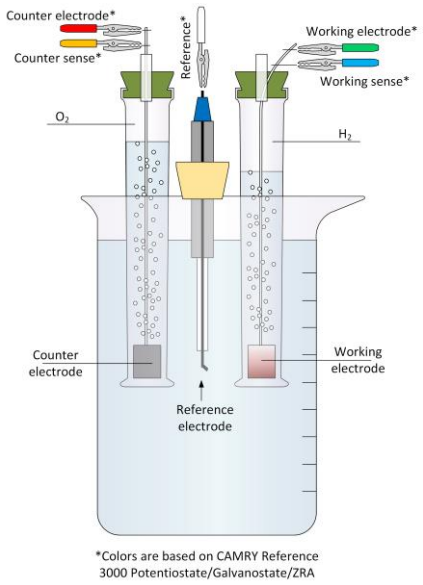

Figure 3.3 Experimental setup of the electrochemical cell for hydrogen production (*colors are based on [68]).

There are various photoreactor designs and shapes to split the water using photon energy available in the literature [58]. The most basic cell for lab scale experiments is an open vessel which is a transparent glass to be able to allow. UV light is seen by three electrodes. Photoreactor with ports allows to separate each electrode and keep stable the electrode positions for each experiment. Photoreactor vessel with gas separation is another model where the electrolyte is separated or small tubes are used for each electrode. When small tubes are used, because the generated gas will flow upward, natural separation occurs. Also, there is an available photocell design where the area of the photoelectrode is fixed by only allowing the certain area of the photoelectrode to have access to UV light.

An example of an electrochemical cell used in this experiment for hydrogen production is shown in Figure 3.3. An open vessel with gas separation is designed for the experiments. As it is mentioned before, since the gas flows up, it is a natural H_2 and O_2 separation. Area of the small sample working electrodes is measured and fixed to 0.35 cm^2. A cell contains a working electrode (WE), a reference electrode (RE) and a counter electrode (CE). RE is chosen Silver/Silver Chloride (Ag/AgCl) which contains solid silver chloride coated silver wire inside of the KCI solution filled glass and specifications related to the RE is given in Table 3.1. The WE is the coated samples being studied which are carbon nanotube-TiO_2 and boron doped TiO_2 coated stainless steel in this case. The CE is used to complete the electrical circuit that starts applying a potential to the WE. In this experiment, CE is chosen as a piece of graphite. In order to minimize polarization effects and the ohmic drop (IR drop), Silver/Silver Chloride (Ag/AgCl) RE is kept at a minimum distance and fixed position to WE during the experiments which help to get more accurate results [69]. Ideally, CE should have bigger surface area compared to the working electrode to restrain any limitation caused by size of the CE [70]. Therefore, during the experiments surface area of the graphite counter electrode is 10 times bigger than WE. Thermometer, gas bubbler tube and stirrer may be used to control the experimental cell environment which is not included in these experiments.

The positioning of the electrodes is arranged according to Figure 3.4 (a) for the electrochemical experiments. As described above, the reference electrode is set between the counter electrode and the working electrode where the reference electrode is stands

about two tip diameter of reference electrode away from working electrode and counter electrode is far away from working electrode. During the experiments, a reference electrode, a working electrode, and counter electrode positions need to be kept stable when design and the electrolyte are changed for the experiment since a small change in the position can cause an error on the experimental results.

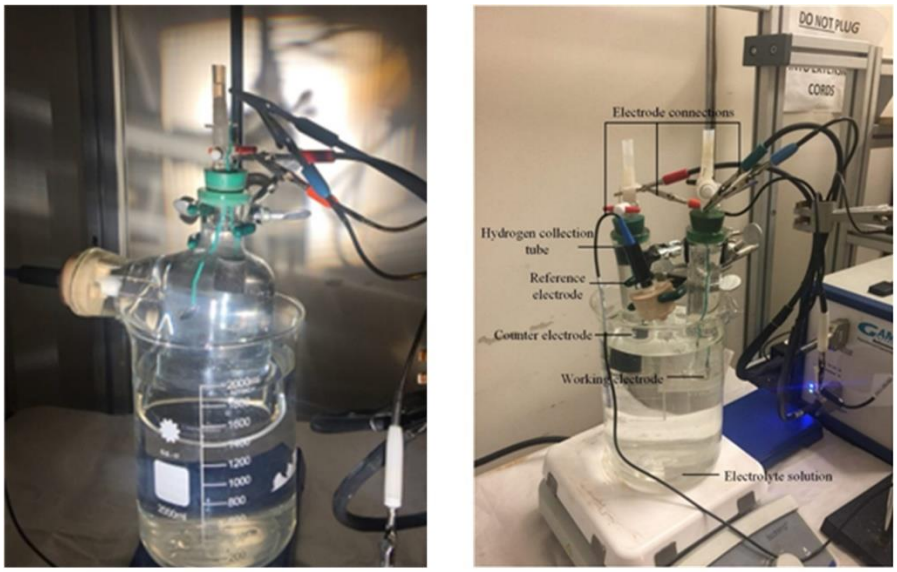

(a) Electrochemical cell design under UV light illumination

(b) Photocell for hydrogen production with gas collection tubes

Figure 3.4 Photocell design with three electrode configuration both for electrochemical experiments and hydrogen production.

Table 3.1 Specifications of the reference electrode used in the electrochemical cell [71].

Electrode Type	Single junction
Electrode Body Material	Glass
Reference Electrolyte	Ag/AgCl
Max Temperature (°C)	100
Connector	Reference pin
Diameter (mm)	12
Length (mm)	154
Offset (Asymmetry Potential)	0 mV +/- 25 mV
Response Time	< 10 s (95% response)
Stability	< 3 mV drift / 24 h

It can be seen, an electrochemical cell in Figure 3.4 (a) which is used for electrochemical experiments is redesigned and made prepared to collect hydrogen for

hydrogen production experiment as in Figure 3.4 (b). The working electrode and graphite counter electrode inserted into separate glass tubes to be able to collect produced hydrogen and the reference electrode is placed between working and counter electrodes. The cables are connected between the electrodes and potentiostat to the color-coded places based on Gamry Reference 3000 Operators Manual [68].

Also, instruments used in the experiments are shown in Figure 3.5 which includes Gamry Reference 3000 Potentiostat/Galvanostat [72] and Trisol Solar Simulator [73].

Figure 3.5 Instruments for the experimental setup: Gamry Reference 3000 and OAI Solar Simulator.

3.4 Experimental Uncertainty Analysis

In order to confirm the accuracy of the results, an uncertainty analysis is performed. The total uncertainty can be written as follow:

$$U_y = \sqrt{\sum_i \left(\frac{\partial y}{\partial x}\right)^2 U_x^2} \tag{3.1}$$

Where $U = \text{Uncertainty of variable}$

The experimental uncertainty consists of random and systematic errors as written below.

$$U_i = \sqrt{S_i^2 + R_i^2} \tag{3.2}$$

where $S_i = \text{Systematic errors}$ and $R_i = \text{Random errors}$

Relative standard deviation

$$RSD = \frac{s}{\bar{x}} 100\% \tag{3.3}$$

where $S = \text{Systematic errors}$ and $\bar{x} = \text{Mean of results}$

The accuracy of the experimental devices given in Figure 3.11 are also given in Table 3.2.

Table 3.2 Accuracy of the experimental devices ([79, 73])

Variable	Device	Range	Device Accuracy	Applied Accuracy	Measured Accuracy
Potential	Gamry Reference 3000 Potentiostat	$\pm$15 V	$\pm$0.003 V	$\pm$1 mV $\pm$ 0.2 % of setting	$\pm$1 mV $\pm$ 0.2 % of reading
Current	Gamry Reference 3000 Potentiostat	$\pm$3 V	$\pm$0.007 V	$\pm$5 Pa $\pm$ 0.5% of range	$\pm$0.2% of value (3 A - 3 nA)
Irradiance	Trisol Solar Simulator TSS-208	600 – 1200 W/m^2	$\pm$20.28 W/m^2	-	-

Chapter 4: Analysis and Modelling

In this chapter, thermodynamic concept for energy and exergy analyses of the experimental study is modeled and the modeling approach for the simulation of reactor design is explained with methodology and the physics used for the simulation.

4.1 Energy and Exergy Analyses

The following section represents the general balance equations of the proposed system, including the mass, energy and exergy balance equations:

The mass balance of the water splitting system analyzed in this thesis can be defined as follows:

$$\dot{m}_{H_2O} = \dot{m}_{H_2} + \dot{m}_{O_2} \tag{4.1}$$

where the $\dot{m}_{H_2O}$ is the mass flow rate of the water input into the system, and $\dot{m}_{H_2}$ and $\dot{m}_{O_2}$ are the mass flow rates of the produced hydrogen and oxygen.

The general energy balance equation can be written as follows:

$$\dot{Q}_{in} + \dot{W}_{in} + \sum \dot{m}_{in}\left(h + \frac{v^2}{2} + gz\right)_{in} = \dot{Q}_{out} + \dot{W}_{out} + \sum \dot{m}_{out}\left(h + \frac{v^2}{2} + gz\right)_{out} \tag{4.2}$$

Here, the left side of the energy balance equation represents the thermal energy rate entering the system, the work rate entering the control volume, and the energy associated with the mass entering the system. The right side represents the energy associated with the mass leaving the system, along with the thermal energy rejected by the system, and the work rate produced by the system.

The energy balance of the water splitting system that was analyzed in this thesis is derived from the general balance equation (4.2) and it can be defined as follows:

$$\dot{m}_{H_2O}h_{H_2O} + \dot{W}_{elec} + I_{solsim}\,A_{WE} = \dot{m}_{H_2}h_{H_2} + \dot{m}_{O_2}h_{O_2} \tag{4.3}$$

where $\dot{W}_{elec}$ is the power provided to the system, h_{H_2O} is the enthalpy of the water input into the system, and h_{H_2} and h_{O_2} are the enthalpies of the produced hydrogen and oxygen at STP. As for I_{solsim} it is the defined as the solar irradiance generated by the solar simulator

and received by the working electrode, and solsim denotes solar simulator, where A_{WE} is the area of the working electrode. It should be noted that I_{solsim} is only applicable when light is present.

The general exergy balance equation can be written as follows:

$$\sum \dot{E}x_{\dot{Q}_{in}} + \sum \dot{E}x_{\dot{W}_{in}} + \sum \dot{E}x_{flow_{in}} = \sum \dot{E}x_{\dot{Q}_{out}} + \sum \dot{E}x_{\dot{W}_{out}} + \sum \dot{E}x_{flow_{out}} + \dot{E}x_d \quad (4.4)$$

Here, the left side of the exergy balance equation represents the thermal exergy rate entering the system, the work rate entering the system, and the exergy associated with the mass flow entering the system. The right side represents the exergy related to the mass leaving the system, along with the thermal exergy rejected by the system, and the work rate produced by the system, and the exergy destruction rate.

The exergy balance of the water splitting system that was analyzed in this thesis can be defined as follows:

$$\dot{m}_{H_2O} ex_{H_2O} + \dot{W}_{elec} + I_{Solsim} A_{WE} \left(1 - \frac{T_0}{T_s}\right) = \dot{m}_{H_2} ex_{H_2} + \dot{m}_{O_2} ex_{O_2} + \dot{E}x_d \quad (4.5)$$

where $\dot{W}_{elec}$ is the power provided to the water splitting system, ex_{H_2O} is the chemical exergy of the water inputted into the system, ex_{H_2} and ex_{O_2} are the chemical exergies of the produced hydrogen and oxygen at STP. I_{Solsim} is the solar irradiance in $(\frac{W}{m^2})$ received by the working electrode, T_0 is the ambient temperature (K) and T_s is the temperature of the sun (K), although the solar irradiance was generated by the solar simulator which means that the source temperature is the solar simulator temperature. However, here the sun temperature is used since the solar simulator simulate the solar irradiance when it is at a certain distance from the working electrode, meaning that it simulate the sun irradiance when it reaches that distance. Thus, the sun temperature is used.

The analyses include the overall exergy destruction rates, exergy, and energy efficiencies for the system. The thermodynamic analyses were taken at steady state conditions. The electrochemical cell overall energy and exergy efficiencies will be defined as follows:

where η_{EC} is the energy efficiency of the electrochemical cell, LHV_{H_2} is the lower heating value of hydrogen at 1 atm in (J/kg) and $\dot{W}_{elec}$ in (W).

As for the exergy efficiency ψ_{EC} it can be defined by the specific chemical exergy of hydrogen, ex_{H_2}, multiplied by the mass flow rate of hydrogen produced by the electrochemical cell, $\dot{m}_{H_2}$.

The energy and exergy efficiencies for the electrochemical cell with light conditions (the electrode is subjected to the solar irradiance generatated by the solar simulator), the relations are seen in Eq. 4.6 and Eq. 4.7. In the following relations energy inputted by the solar energy ($A_{WE} \times I_{Solsim}$) was taken into account in addition to electrical work ($\dot{W}_{elec}$).

$$\eta_{EC} = \frac{\dot{m}_{H_2} \times LHV_{H_2}}{\dot{W}_{elec} + A_{WE} \times I_{Solsim}} \tag{4.6}$$

$$\psi_{EC} = \frac{\dot{m}_{H_2} \times ex_{H_2}}{\dot{W}_{elec} + A_{WE} \times I_{Solsim}(1 - \frac{T_0}{T_s})}. \tag{4.7}$$

From the exergy efficiency one can define the exergy destruction rate as seen in equation 4.8.

$$\dot{E}x_d = (1 - \psi_{EC})\left(\dot{W}_{elec} + A_{WE} \times I_{Solsim}\left(1 - \frac{T_0}{T_s}\right)\right) \tag{4.8}$$

4.2 Electrochemical Analyses

A brief description of the governing equations and the main electrochemical reactions that occur in the water splitting system are presented in this section. In this thesis the working electrode is made of TiO_2 plus boron and carbon nanotubes were used to increase the efficiency of the semiconductor material. The reaction that occur when the semiconductor (TiO_2) absorbs the photon energy can be written as follows:

$$TiO_2 + hv \rightarrow TiO_2(e^-) + TiO_2(h^+) \tag{4.9}$$

Here, the hv presents the amount of energy the photon has, which should be either equal or higher than the semiconductor bad gap potential, which is 3.2 eV for TiO_2. The reactions occur on the working electrode and counter electrode for generation of hydrogen and oxygen can be written as follows:

$$2H^+ + 2e^- \rightarrow H_2 \tag{4.10}$$

$$2H_2O + 4h^- \rightarrow O_2 + 4H^+ \tag{4.11}$$

Adding the reduction and oxidation reactions with equations (4.9), leads to the overall water splitting reactions as follows:

$$H_20 + hv \rightarrow H_2 + \frac{1}{2}O_2\ ,\ \Delta G = 238\frac{kJ}{mol} \tag{4.12}$$

Analyzing the electrochemical cell performance, which is in this case is the water splitting system can be done by assessing its Faraday's efficiency. The amount of the gas produced with hydrogen production is directly related with the electrical charge consumed by the electrochemical cell which can be defined by Faraday's law:

$$N = \left(\frac{1}{nF}\right)q \tag{4.13}$$

$$\dot{m} = \frac{NxM}{t} \tag{4.14}$$

where N is electron per hydrogen production, M (g/mol) is the molar mass of hydrogen, t is the operation time of the experiment and F is the Faraday constant with the value of (96485 A s/mol and $\dot{m}$ (g/s) is hydrogen production rate. N shows the electron per hydrogen production which can be find with using n hydrogen production (mol), F faraday constant (96485 A s/mol) and q electrical charge (A s). Generally, high current value apply lower mass transfer lost which means higher efficiency. Efficiency can be define as:

$$\eta_F = \frac{HV_{H_2}\ x\ \dot{m}_{H_2}}{\dot{W}_{elec}} \tag{4.15}$$

4.3 Modeling Approach and Simulation

This section discusses the system description of the proposed designs including the boundary conditions and the simulation settings for each design including the base design proposed by Acar and Dincer [52].

There are two different ways of simulating the flow and the collection of the produced hydrogen. The first example of simulating the continuous flow of the electrolyte as was presented by Carver et al. [63], which is not a direct two-phase flow modeling and simulation. In their model of assessing the reactor design was done through ensuring a maximum activity across the whole surface of the electrodes and making sure that the flow pattern is uniform as well across the reactor. So the models aim mainly as a fluid flow model that considers the hydrogen and the oxygen through their diffusion coefficient in water as well as the changing concentration of hydrogen and oxygen with respect to temperature. However, the first model lacks the study of the two-phase flow phenomena, which has high importance for the design of the reactor as well the studies in this work will show later on. The main problem with the design is the accumulation of hydrogen bubbles at the various points through the reactor leading to degradation in the safety and performance of the reactor as mentioned earlier. The accumulation of the bubbles and the formed hydrogen at various location within the reactor can be investigated with a two-phase flow modeling and here where the proposed second modeling methodology comes in.

The second modeling methodology, which is also used in this work is simulating the flow of the generated hydrogen as zero velocity bubbles located at a certain height from the bottom edge of the reactor considering the dimensions of the membrane. So in the proposed design, the two-phase flow modeling is considered to simulate the natural flow of the bubbles due to buoyancy, which is usually the case for a small PEC reactor with a low hydrogen production rate. Note that further simulations can be considered at a higher production rates of hydrogen that the inlets and the outlets have to be set with a water and electrolyte supply rate that might affect the flow, however the worst case scenario is the low production rate was the makeup electrolyte and water is very low that its effect on the bubble collection can be neglected. So in the two-phase flow model, the inlet is not

considered and the outlet is considered at a specified pressure point constrain, which is the atmospheric pressure in the considered case. Gravity is considered to simulate the buoyancy of the bubbles. Finally, all the walls are set to no-slip condition and the geometry is cut in the line of symmetry of the geometry and half of the proposed geometry is simulated as shown in section 5.2. Final important point within the simulation is that all the simulations are run transient for 2 seconds, however once the system reaches a steady state, which will happen when the all the bubbles reach the collection channel or when the bubbles stop from moving either reached the collection channel or have got stuck and they can't escape anymore. Note that the main aim of the simulations is to compare the different designs on the same basis. The size of the bubbles is selected be 0.1 in, where the size of the hydrogen bubbles is not a determining factor since if the surface tension was not able to hold such size, it would break to bubbles with a size the surface tension at the water and hydrogen interaction surface able to hold.

4.3.1 Physics Used in the Simulation

Several pairs of equations can be used to define the flow type based on the type of flow which is substantial step due to the fact that analyses taken from fluid flow study are used to solve for the other physical interferences used in the simulations. Additionally, making simple and accurate assumptions for the initial and boundary conditions for fluid flow is the critical part of reducing the computational time.

The Computational Fluid Dynamics (CFD) modules give a better understanding and a chance to improve devices and processes in engineering application for both closed and open systems by designing, predicting and analyzing the fluid flow phenomena which consider flow patterns, pressure losses, forces on objects, temperature distribution a variation of fluid composition. In the simulation presented in this study, laminar flow interference was used to solve for pressure and velocity in the laminar flow region. As long as Reynold's number is below a critical value, the flow remains laminar and there is no tendency to cause transitions to turbulence. Reynold's number depends on the model and the geometry, but it's going to be shown later that it's low enough to assume laminar flow. Laminar flow interference supports all the three type of compressibility depending on the fluid properties and flow regime, namely: incompressible flow, weakly compressible flow,

and compressible flow. For all the three compressibility options, Navier-Stokes equations for conservation of momentum and the continuity equations for conservation of mass are being solved. However, for the incompressible option in which the density is a function of both reference pressure and reference temperature, the incompressible form of Navier-Stokes equations are used. However, for the weakly compressible option in which the density of the fluid depends only on the temperature and the pressure has a negligible effect on the density, the compressible form of Navier-Stokes equations are used. The last option is the compressible flow in which the compressible form of Navier-Stokes equations are used as well. Laminar flow interference also supports both stationary and time-dependent analyses.

Level set interference is used to track the interaction between two fluids in multiphase applications by solving transport equations for the level set function. As long as the level set inference is used in any simulation, the time-dependent study should be conducted since the interaction between different fluids depends on history and can never be stationary.

Chapter 5: Results and Discussion

In this chapter, experimental results for electrochemical analysis, hydrogen production results of the coatings and thermodynamic analysis of the systems are presented and analyzed. At the end of the chapter, the results of the PEC reactor design simulation is presented and discussed.

5.1 Experimental results

In this section, experimental results regarding the characterization and photocatalytic hydrogen are presented. Table 5.1 summarizes the error percentages for the measurements associated with the devices used during the experiments for recording and measurements of the data.

Table 5.1 Experimental uncertainty analysis.

Variable	Device	Ref. Value	Bias Error	Rel. Bias Error %	Statistical Uncertainty %	Absolute Uncertainty %
Potential	Gamry Reference 3000 Potentiostat	2 V	0.006 V	0.3	2.13	2.15
Current	Gamry Reference 3000 Potentiostat	0.3 A	±0.06 A	0.20	0.67	0.70
lrradiance	Trisol Solar Simulator TSS- 208	1000 W/m^2	±20.28 W/m^2	2.03	0.23	2.04

5.1.1 Cyclic Voltammetry

Cyclic voltammetry is a commonly used technique in the field of electrochemistry, which specifically used to interrogate the chemistry and the physics at the interface between the electrochemical cell electrode and electrolyte where the electrolyte can be a saline solution. The interface between the electrode and the electrolyte is referred to as the electroactive surface, which can be found in various electrochemical devices such as batteries and fuel cells. To this day with advancement in the fuel cells, electrolyzers and batteries the interface between the electrode and electrolyte of the cell is not fully understood and still under continuous research by the industry and academia.

As mentioned earlier, the interface between the electrode and the electrolyte has a critical importance and cyclic voltammetry can be an essential step in the verification and design of such electrochemical devices, since a single scan of the interface using the cyclic voltammetry results in a great deal of valuable information that characterizes the chemical and physical behavior of the electrochemical system. The importance of the cyclic voltammetry can be summarized in the great virtue its massive and diverse information it provides for the interface between the electrode and the electrolyte. The information cyclic voltammetry provides shows the competition between the rate of transport of the reacting chemical species to the electrode surface by diffusion and the rate of the electrolysis at the electrode surface [74]. In addition, it also provides information on the rates and the mechanism of the chemical reactions in the solution of the cell. The cyclic voltammetry runs on different scan rates, where each of the scan rates is the rate of change of the voltage in time is altered, where it can result in different system timescales and as a result different physical phenomena.

The cyclic voltammetry graphs show the applied voltage vs the response which is the resulting amount of current flow per unit cross-sectional area of the working electrode. The scan rate specifies the linearly changing potential at the speed of 20,40,60,80,100 and 200 mV per second. Applying higher scan rates causes a decline in the diffusion layer size which results in observation of higher currents.

As mentioned above, the reason for applying several scan rates for the applied voltage is to understand the time scale of the chemical reactions to be able to measure them with cyclic voltammetry. Figure 5.1 and Figure 5.2 shows the cyclic voltammetry graphs for uncoated stainless steel photoelectrode. It is an evident that using a smaller scan rate for the applied voltage damages the equilibrium at photoelectrode/electrolyte interface which removes anodic and cathodic peaks. In addition, when the electrochemical time scale is shortened to a scan rate of 20 mV/s, the voltammogram lines are almost irreversible compare to higher scan rates. One anodic and one cathodic current peaks could be observed in the cycles. It is noted that when the scan rate of 200 mV/s is used, the anodic peaks are around -9 mA/cm^2 and -11 mA/cm^2 for no light and light conditions, respectively.

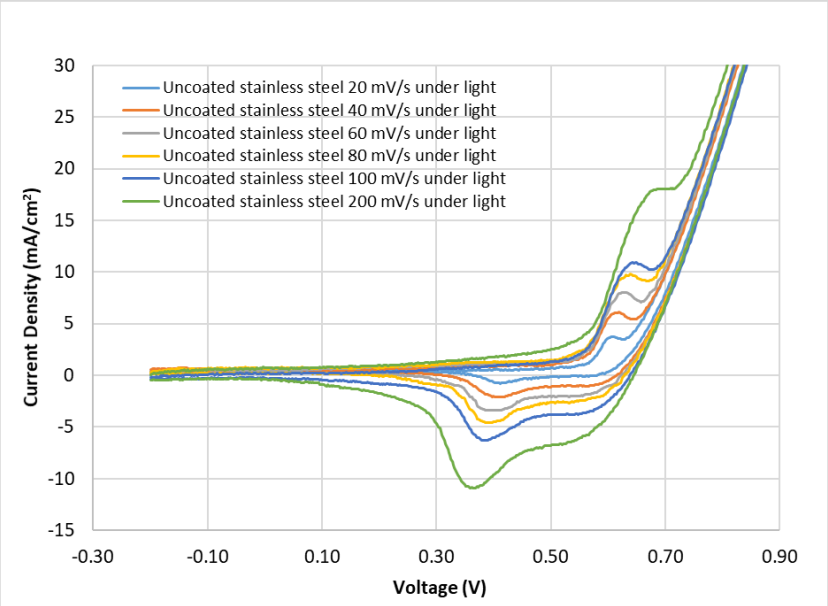

Figure 5.1 Cyclic voltammetry graph for uncoated stainless steel with light.

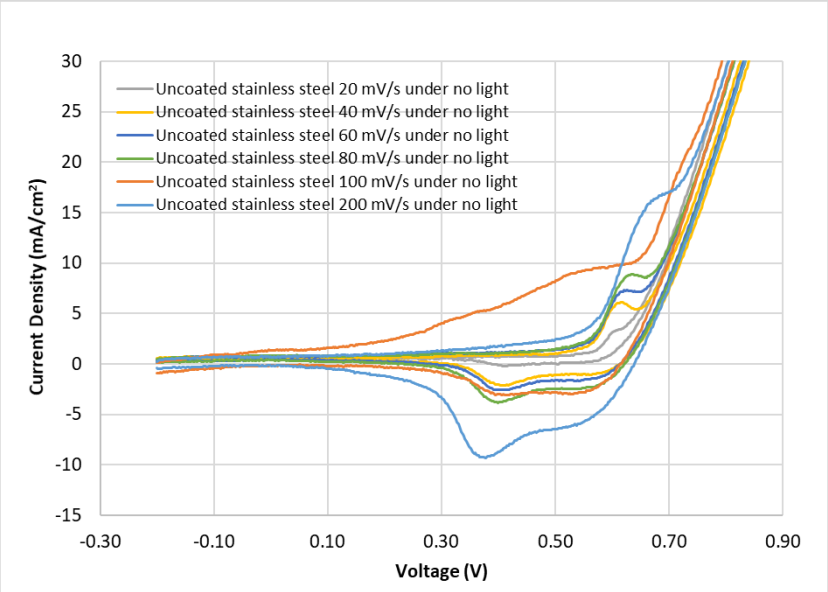

Figure 5.2 Cyclic voltammetry graph for uncoated stainless steel with no light.

The main distinction between semiconductor coated photoelectrodes and standard metal electrodes is that semiconductor coated photoelectrodes have an ability of absorption of light which causes chemical reactions which generate electricity. Since hydrogen production is related to reduction process, for boron-doped TiO_2 and carbon nanotube-TiO_2, irreversible cyclic voltammetry applied to observe reduction processes by changing the reduction potential with different scan rates while oxidation reduction is kept constant.

It can be seen that redox potential of the carbon nanotube-TiO_2 with 200 mV/s scan rate is around -10 mA/cm^2 shown in Figure 5.4 which shows better performance compared to boron doped TiO_2 which has -6 mA/cm^2 at the same scan rate which is shown in Figure 5.3.

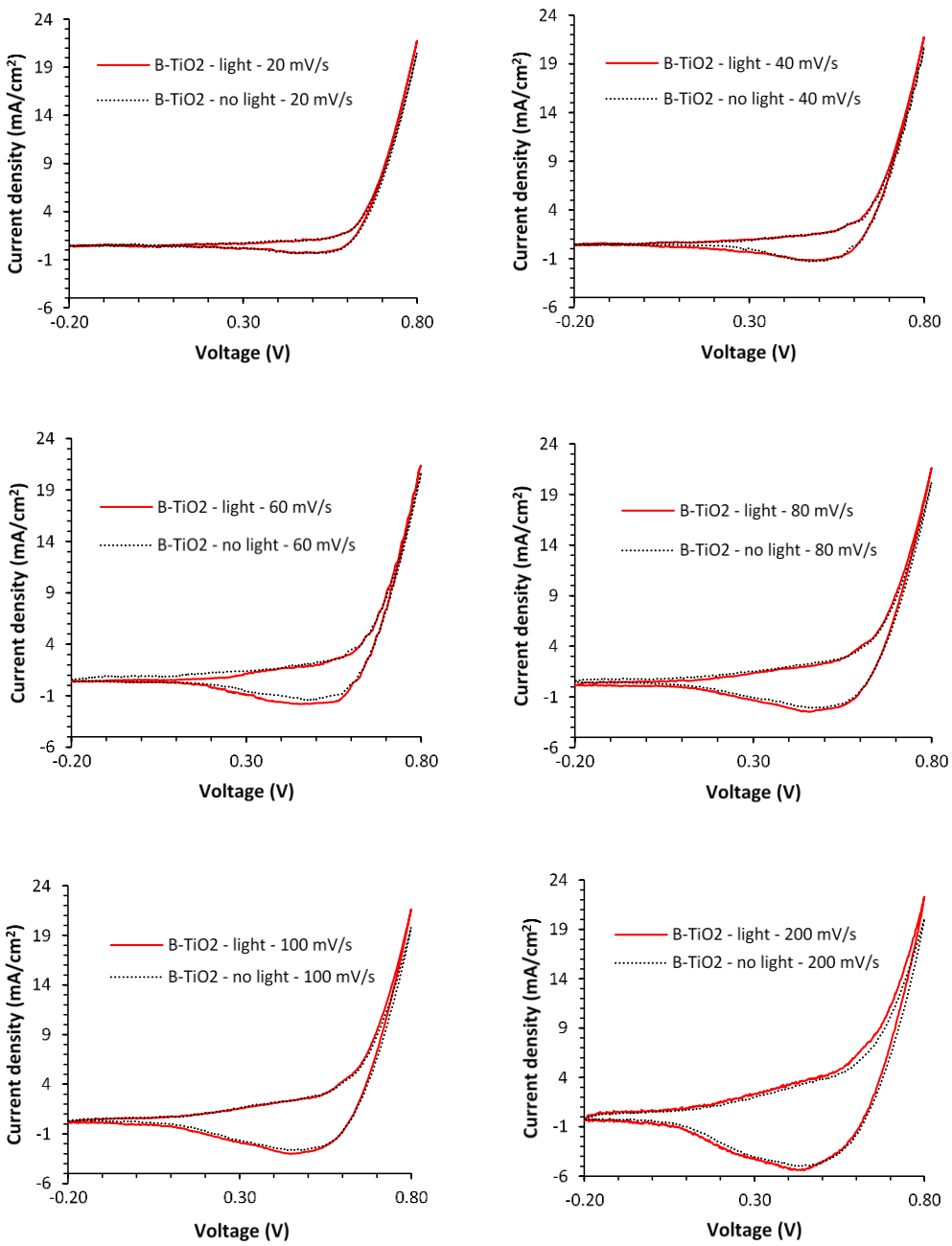

Figure 5.3 Cyclic voltammetry graph for B-TiO_2 at a scan rate 20,40,60,80,100 and 200 mV/s from -0.2 to 0.8V with light and no light conditions

Moreover, Boron doped TiO_2 have a great performance under light condition having a positive shift in the current density for both oxidation and the reduction processes. On the other hand, carbon nanotube-TiO_2 has more oxidation at 20 mV/s, 40 mV/s, 60 mV/s and more reduction at higher scan rates.

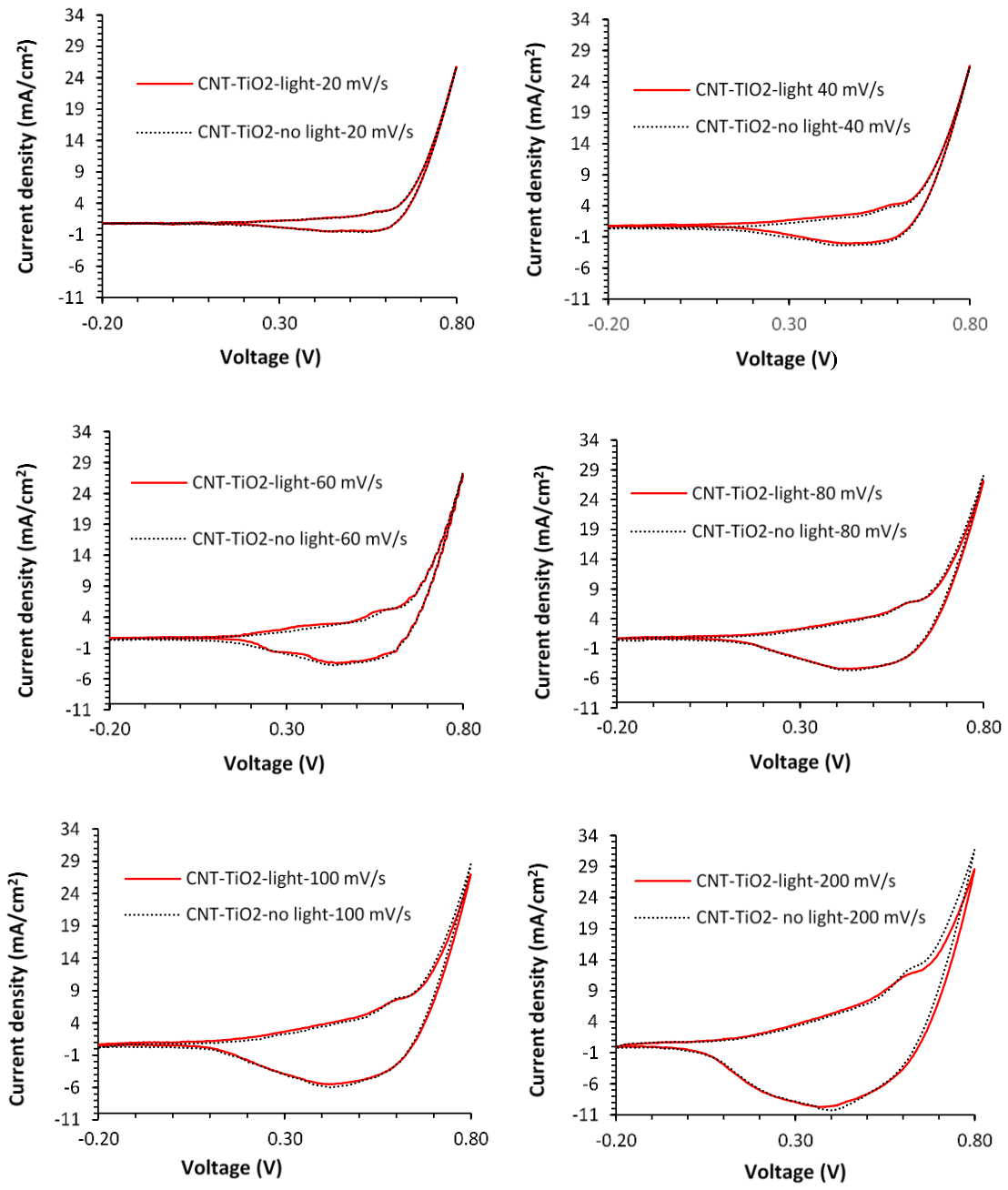

Figure 5.4 Cyclic voltammetry graph for CNT-TiO_2 at a scan rate of 20,40,60,80,100 and 200 mV/s from -0.2 to 1V with light and no light conditions

5.1.2 Electrochemical Impedance Spectroscopy

Electrochemical impedance spectroscopy (EIS) is an electro-analysis method to investigate the resistance mechanism and their effects on the impedance of the electrochemical cell. Oliver Heaviside was the first to introduce the concept of electrical impedance in the 1880s. Later on, A. E. Kennelly and C. P. Steinmetz developed his concept in terms of complex numbers and complex diagrams [75]. Since then, scientific advancements and a wide range of practical applications in the field of electrochemistry used this technique.

In order to characterize impedance measurements, Nyquist and Bode plots are usually used. In Nyquist plot, the x-axis represents the real part of the impedance while the y-axis represents the imaginary part of the impedance. Every point in Nyquist plot resembles the impedance at a specific value of the frequency. One main disadvantage of Nyquist plot is that the information represented by the plot is not complete, specifically the frequency cannot be determined by looking at the plot. In other words, the frequency for every point at which the impedance is measured cannot be specified. Also, finding the low impedance values that are usually found at very high frequencies are not easy to be found in Nyquist plot. On the other hand, Bode plots clearly show frequencies values reveals low impedance values at high frequencies. Bode plots show the total value of the impedance (logarithm of impedance magnitude) and the phase shift angle in the y-axis as a function of the frequency (logarithmic frequency) in the x-axis. [76, 77]

Electrical resistance is defined as the ability of an element in a circuit to resist the flow of electricity. Similar to resistance, capacitance is also defined as the ratio between the input voltage over the output current which is represented by the real part of the impedance. However, it also takes into account the ability of the circuit to store electrical energy which is represented by the imaginary part of the impedance. In addition, Impedance takes into account the phase difference between input voltage and output current and that's why it's a more general concept that pure resistance or pure capacitance.

The real and the imaginary portions of the degree of impedance are written as $|Z| = \sqrt{z_r^2 + z_j^2}$ and the phase angle can be written as $\varphi = \tan^{-1} Z_j/Z_r$. The responses of the impedance can be written as $Z_R = R$ for the resistor, $Z_L = j\omega L$ for inductors and $Z_C =$

$\frac{1}{j\omega C}$ for the capacitor. The impedance of a perfect resistor is real and the in phase with the potential through it. However, the impedance of a perfect capacitor is imaginary which decrease with increase in frequency.

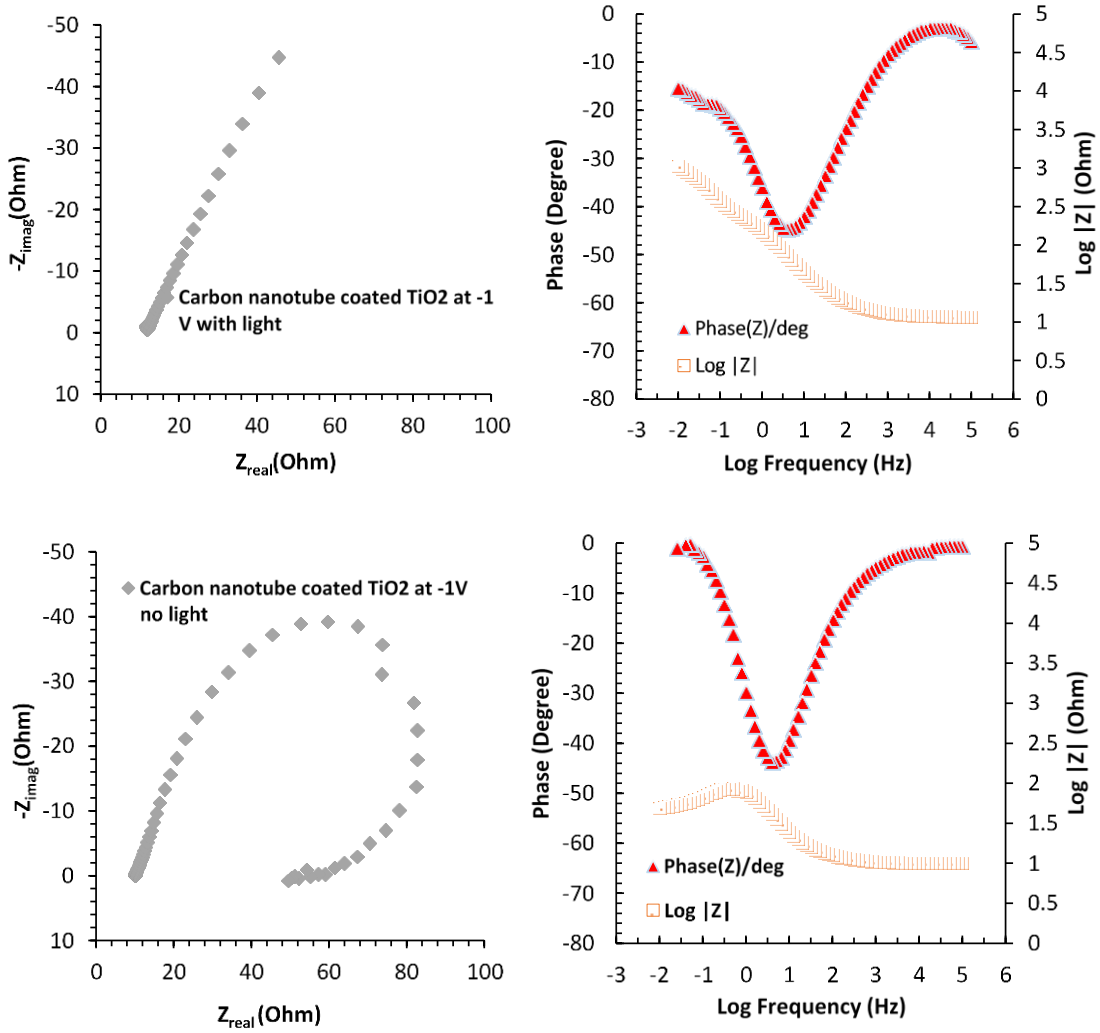

Figure 5.5 Electrochemical impedance spectroscopy of CNT- TiO_2 coated stainless steel at AC voltage of 5 mV and DC voltage of -1 vs OCP at frequency scan from 100 kHz to 0.01 Hz with 10 points per decade.

Electrochemical impedance spectroscopy (EIS) measurements are also done with applied measurement technique potentiostatic EIS to study electrochemical properties of the electrodes and internal process of the cell which are presented through Nyquist and Bode diagrams at both alternating current (AC) voltage of 5 mV and direct current (DC) voltage of -1 vs open circuit potential (OCP) and AC voltage of 5 mV and DC voltage of

0 vs OCP under light and no light conditions. Frequency scan from 100 kHz to 0.01 Hz with 10 points per decade.

The semicircles are caused by anode and cathode activation resistance in the Nyquist plots can be seen in Figures 5.5-5.10 under no UV light conditions. Note that the hydrogen oxidation reaction activation loses can be identified by the diameter of the semicircles at high frequencies which are not easy to detect under UV light since lost lesser activation [77]. On the other hand, at the medium frequencies, the semicircles are results of oxygen reduction reaction activation losses [78].

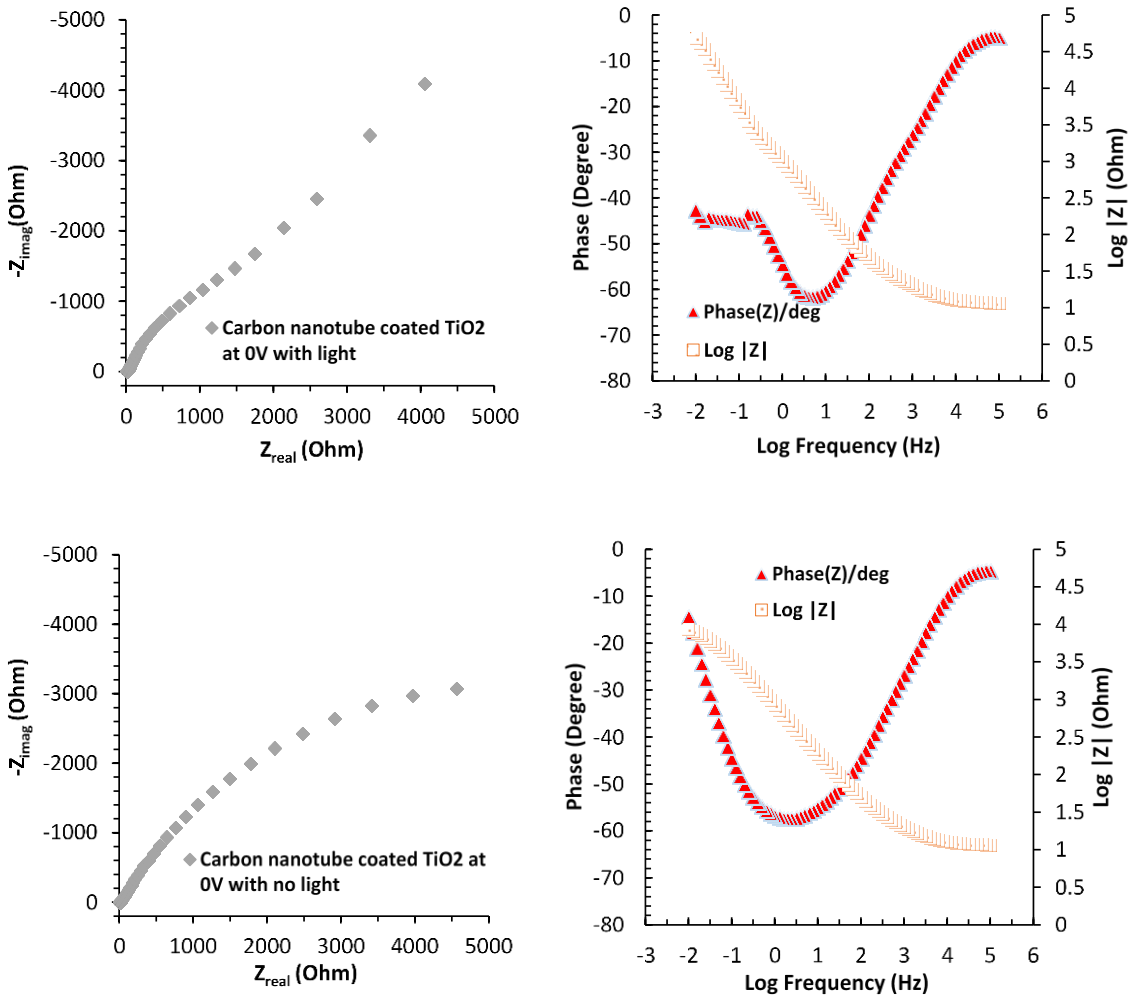

Figure 5.6 Electrochemical impedance spectroscopy of CNT- TiO_2 coated stainless steel at AC voltage of 5 mV and DC voltage of 0 vs. OCP with light and no light condition at frequency scan from 100 kHz to 0.01 Hz with 10 points per decade.

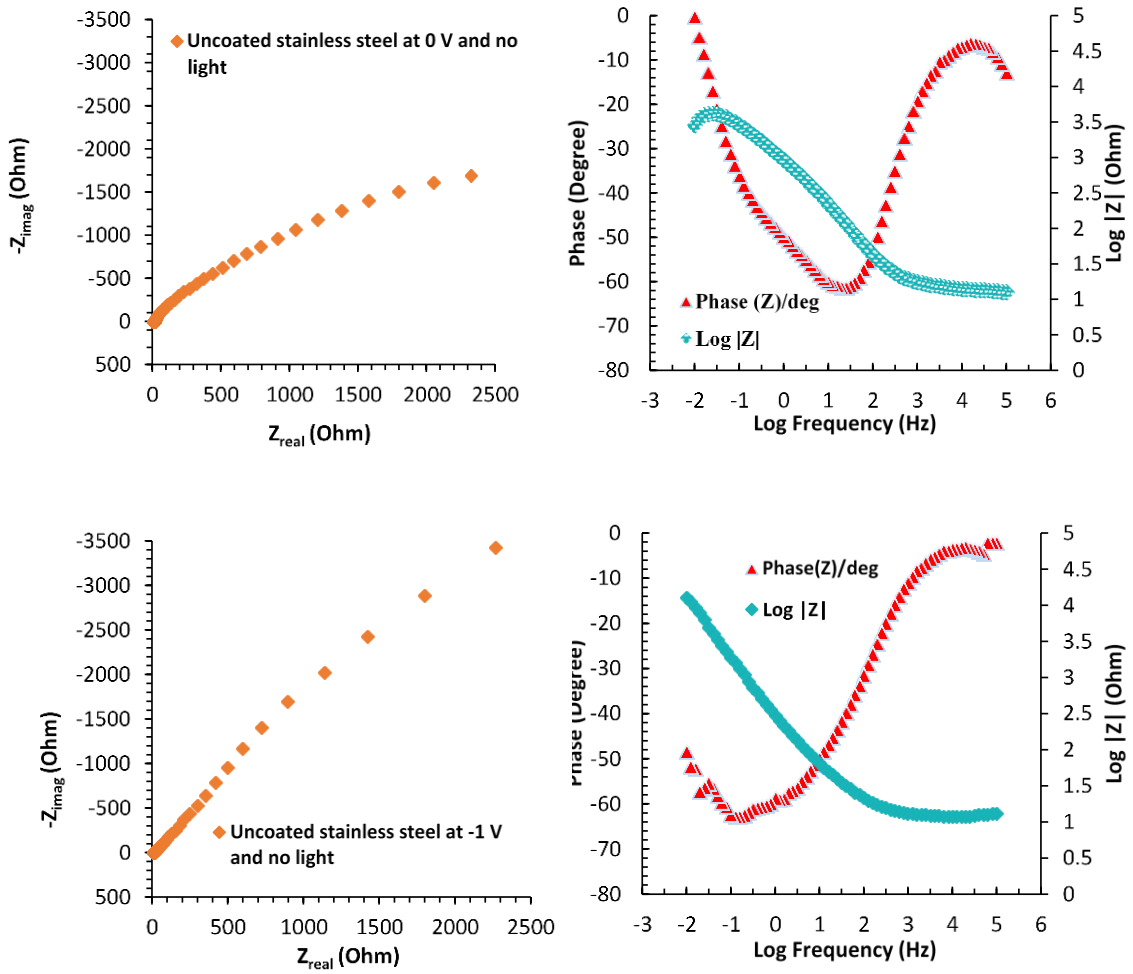

Figure 5.7 Impedance spectra of uncoated stainless steel electrode without light conditions at frequency scan from 100 kHz to 0.01 Hz with 10 points per decade.

It can be seen that when the DC voltage is decreased to -1 mV from 0 mV, a high activation resistance is observed for uncoated stainless steel, boron doped TiO_2 and carbon nanotube-TiO_2. The main reason for the difference is that each reaction needs a certain amount of energy to be driven. As observed in the Nyquist and Bode plots of Carbon nanotube-TiO_2 photoelectrode in Figure 5.6 and Figure 5.7, impedance spectrum is highly affected by the applied UV light and there is a quite difference between impedance spectra under no light and light conditions. As shown in Figure 5.6, the arc radius under light condition is almost 45 degrees. No arc in the graphs means that there is no diffusion and if there are two arcs, it represents that diffusion is available. Moreover, if the arc gets closer to the real part at low frequency, it means that a finite diffusion in the photocell [77].

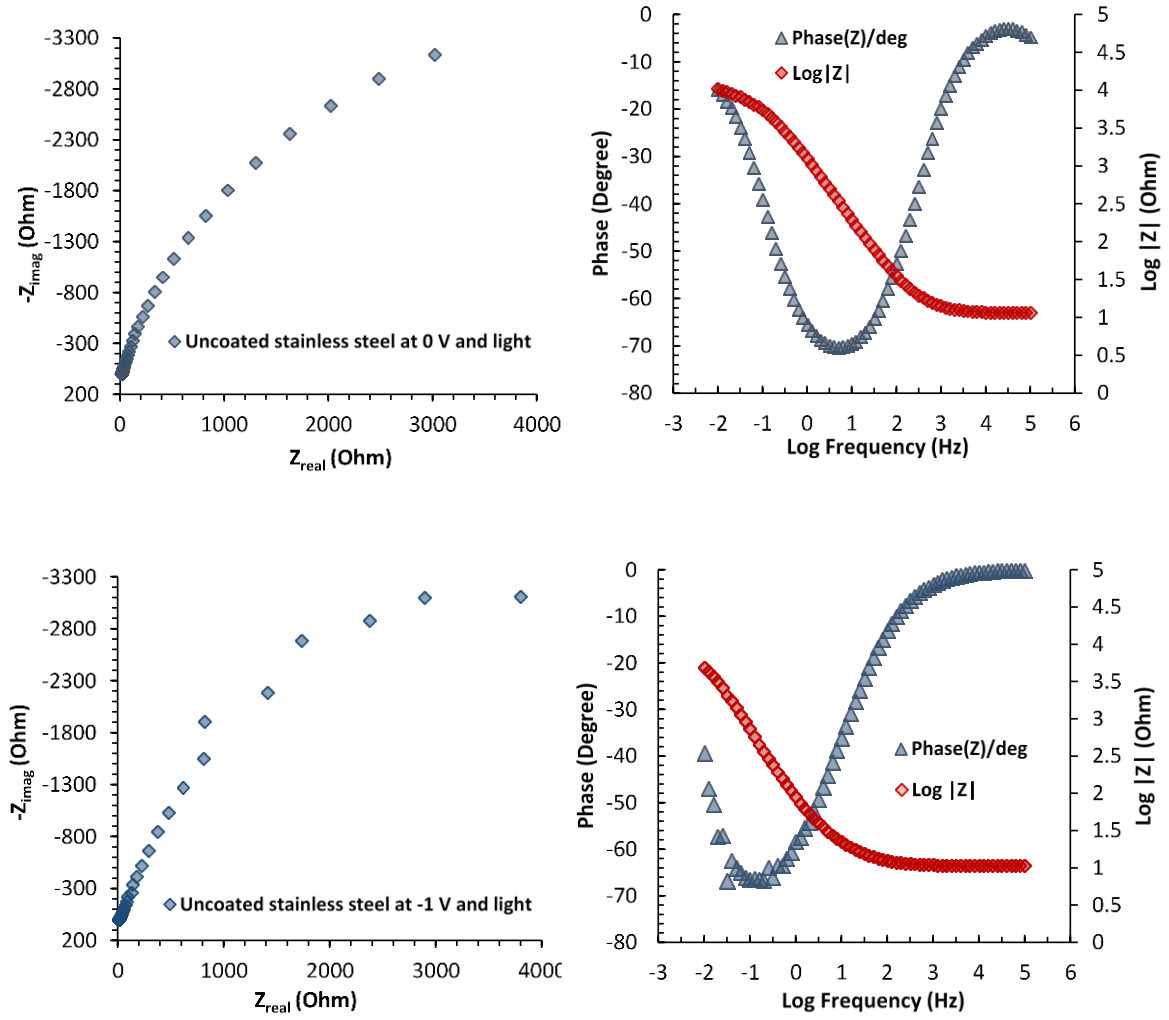

Figure 5.8 Impedance spectra of uncoated stainless steel electrode at AC voltage of 5 mV and DC voltage of 0 mV vs OCP with light and without light conditions at frequency scan from 100 kHz to 0.01 Hz with 10 points per decade.

If uncoated stainless steel impedance spectroscopy plots in Figure 5.7 and Fig. 5.8 are compared with boron doped TiO_2 and carbon nanotube-TiO_2 graphs; it is seen obviously that both under light and no light conditions impedance of the stainless steel in Figure 5.7 and Figure 5.8 are considerably higher than the other photoelectrodes in Figure 5.5, Figure 5.6, Figure 5.9 and Figure 5.10.

In Figures 5.9 and 5.10, the impedance spectroscopy of boron doped TiO_2 photoelectrode is presented under no light and light condition with DC voltage of 0 mV

and -1 mV, respectively. As expected, real and imaginary parts of the impedance is smaller under no light condition which means interfacial resistance is reduced under light condition. As shown in Figures 5.9 and 5.10, the arc radius of the photoelectrode under light condition is slightly smaller than with no light condition in Nyquist plots which indicates that charge transfer rate is faster [79]. Considering carbon nanotube TiO_2 impedance spectroscopy plots, it can be concluded that boron-doped TiO_2 has higher resistance. Note that when DC voltage is decreased impedance in the circuit is increased.

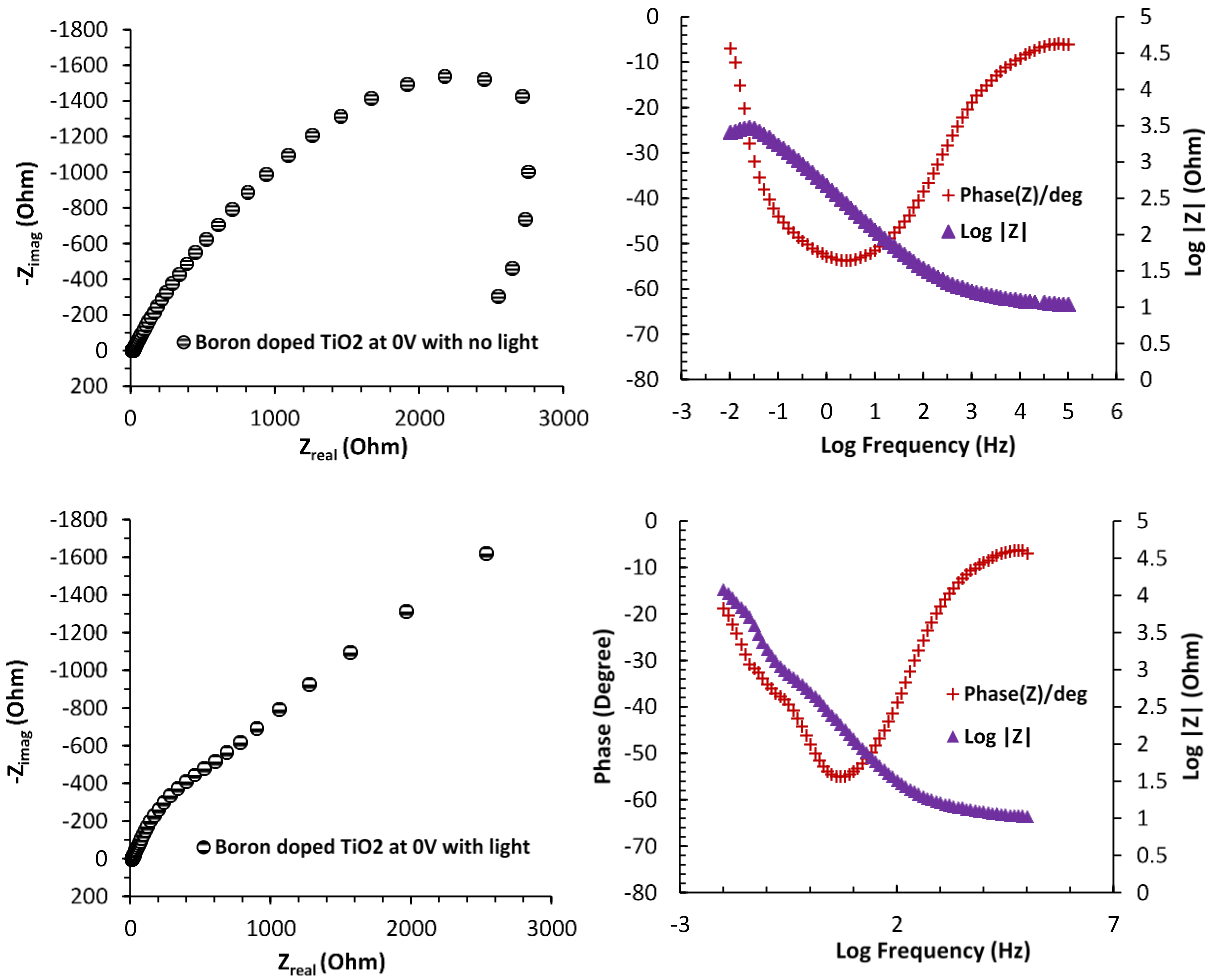

Figure 5.9 Impedance spectra of boron doped TiO_2 stainless steel electrode at AC voltage of 5 mV and DC voltage of 0 mV vs OCP with light and without light conditions at frequency scan from 100 kHz to 0.01 Hz with 10 points per decade.

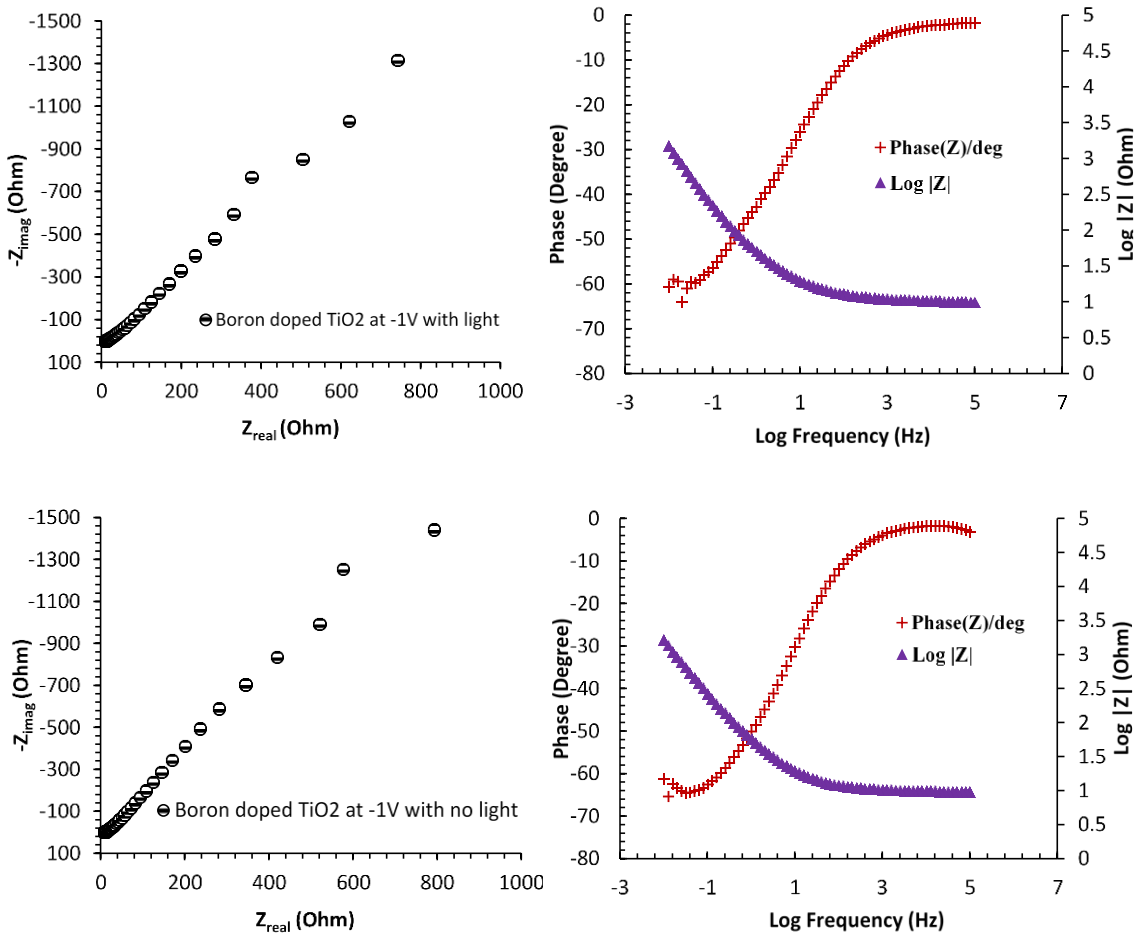

Figure 5.10 Impedance spectra of boron doped TiO_2 stainless steel electrode at AC voltage of 5 mV and DC voltage of -1 mV vs OCP with light and without light conditions at frequency scan from 100 kHz to 0.01 Hz with 10 points per decade.

5.1.3 Chopping

The photocurrent response of the coated materials are studied in chopping (UV light source switched on-off periodically) which are consistent with photocatalytic activity in hydrogen production. When the applied current zero, the potential between the reference electrode and working electrode can be observed with the open circuit potential (OCP) plots. Rapid change in open circuit potential after UV light is switched on means that photocurrent gives fast response to light. Figure 5.11 and Figure 5.12 show the open circuit potential scan of B-doped TiO_2 and CNT-TiO_2 working electrodes using graphite counter electrode under manual UV light chopping.

Under manual chopped light cycles, both samples have good photo-responses. Both photoelectrodes generates negative photovoltage which have a gradual positive shift in OCP under light which indicates that the materials used shows p-type conductivity and accumulates positive charge [35]. When light is off the open circuit potential values have negative shift and takes smaller values while the potential sharply increases to higher values when the light is on because generated electron-hole pairs cause an increase in electric potential [80].

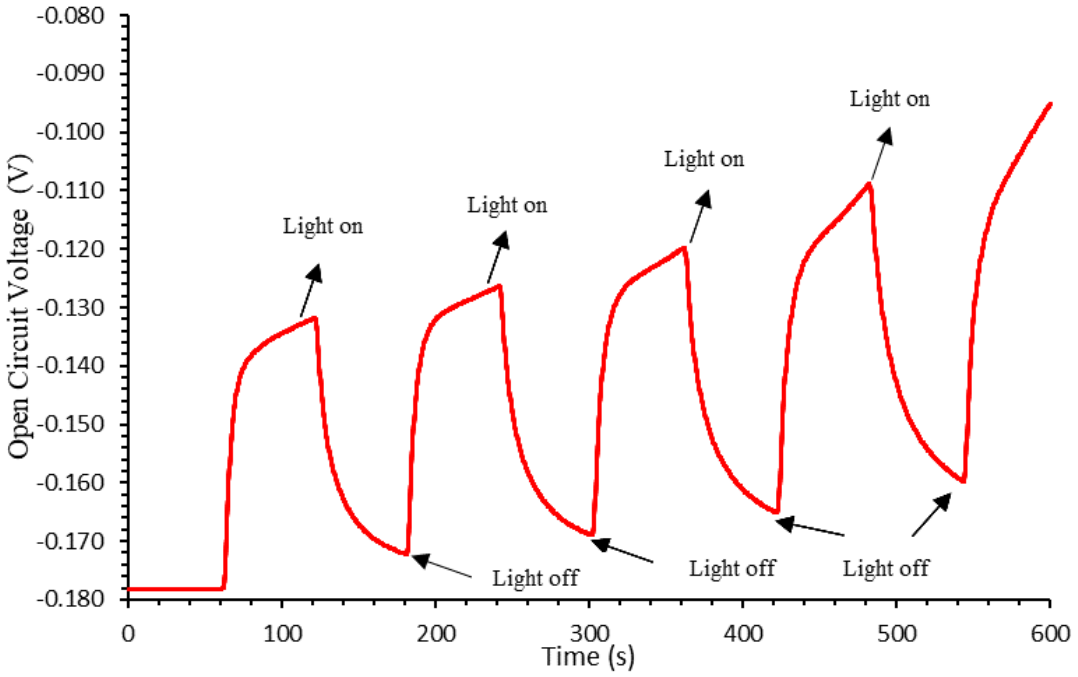

Figure 5.11 Open circuit potential vs time profile of CNT-TiO_2 photocatalyst in 0.05 M NaOH electrolyte solution under manual UV light chopping

Also, in Figure 5.11 the difference between OCP under light (-0.110 V vs Ag/AgCl) and the OCP under no light (-0.164 V vs. Ag/AgCl) for CNT-TiO_2 shows that photovoltage (V_{ph}) of 0.054 V. Similarly, in Figure 5.12 the difference between OCP under light (-0.076 V vs Ag/AgCl) and the OCP under no light (-0.100 V vs. Ag/AgCl) for B-doped TiO_2 shows that photovoltage (V_{ph}) of 0.024 V. In Figure 5.12, the reason behind a downward trend in the voltage can be that the photoelectrode's resistance to the corrosion and the action of the electrolyte is low [77]. It can be concluded that CNT-TiO_2 performs better photocatalytic activity compare to boron doped TiO_2.

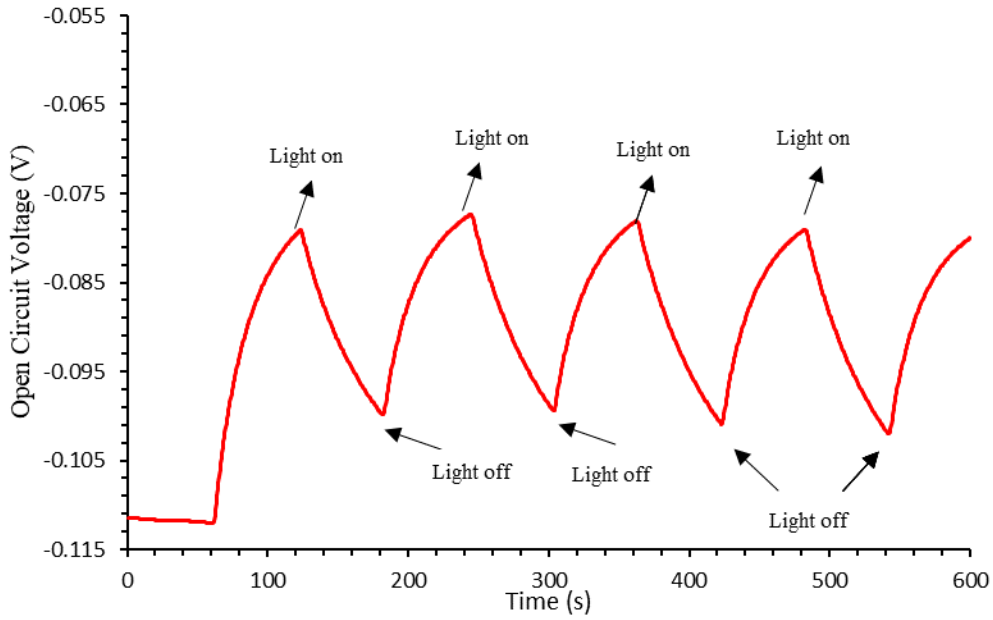

Figure 5.12 Open circuit potential vs time profile of B doped TiO_2 photocatalyst in 0.05 M NaOH electrolyte solution under manual UV light chopping

5.1.4 Chronopotentiometry

Chronopotentiometry is one of the chronometric techniques to analyze the kinetics of chemical reactions which operates under a constant current flowing through the cell stepped by initial current zero to measure the potential between the working and reference electrode as a function of time [82]. Moreover, the current can be reversed between two different current steps for a specified number of cycles to expand the scope of the technique which is called cyclic chronopotentiometry. The potential change is large and easy to observe.

Figure 5.13 shows chronopotentiogram of the CNT-TiO_2 for 1500 seconds in total applied step current of 0.75mA for 120 s and 0 mA for 180 s with a total of 10 cycles. The range of voltages was from −0.45 V to -17 V. Clearly, the UV light irradiation effectively enhanced the electrochemical properties since there is a shift between no light and with light conditions. Note that when the step current is decreased to 0.35 mA in Figure 5.14, plateau potential rise up to positive potential value of 0.63 mA.

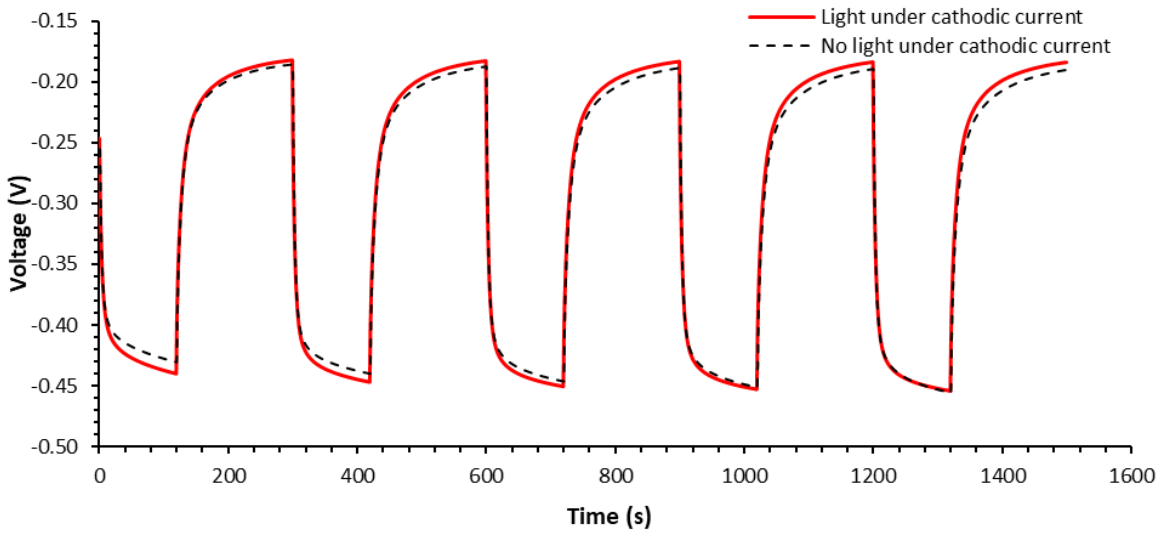

Figure 5.13 Constant current charge/discharge of CNT-TiO_2 electrode at an applied step current of 0.75 mA for 120 s and 0 mA for 180 s with a total of 10 cycles under light and no light condition

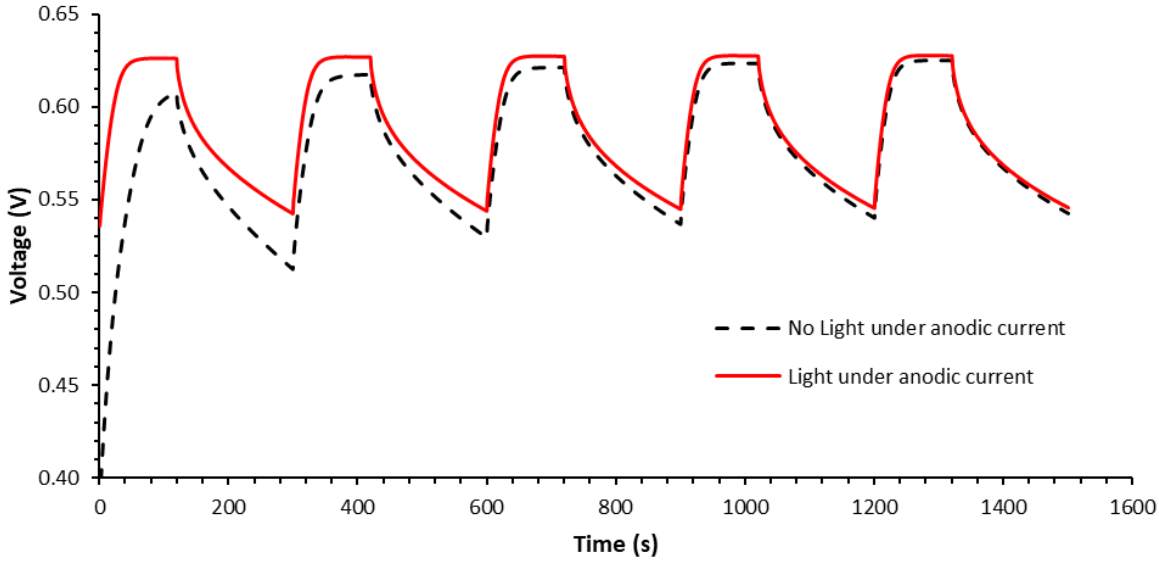

Figure 5.14 Constant current charge/discharge under light and no light condition for CNT-TiO_2 electrode with an applied step current of 0.35 mA for 120 s and 0 mA for 180 s with a total of 10 cycles

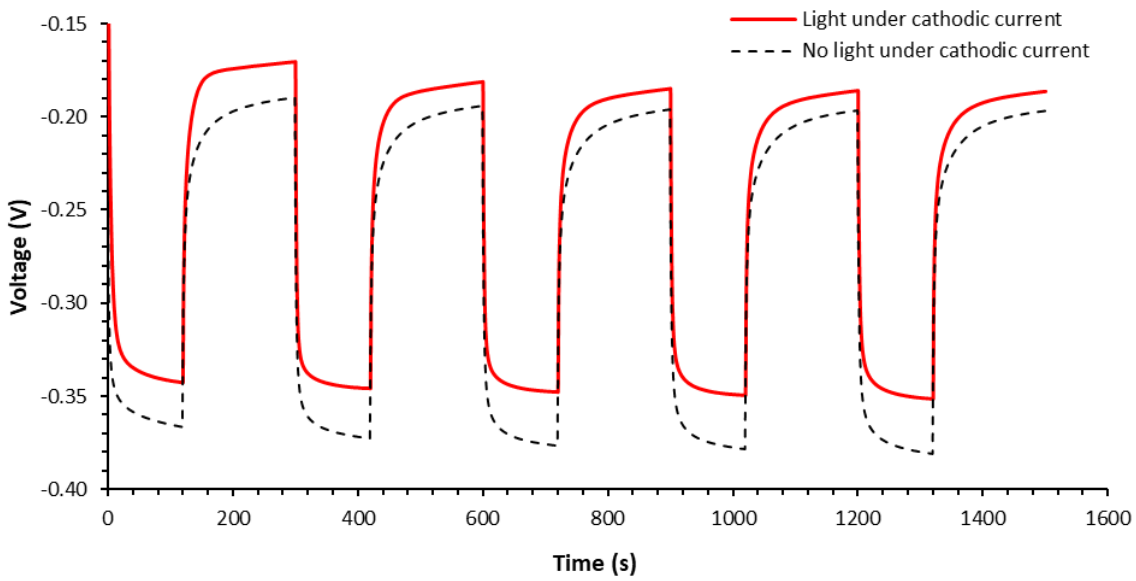

Figure 5.15 Constant current charge/discharge under light and no light condition for B doped TiO_2 electrode with an applied step current of 0.35 mA for 120 s and 0 mA for 180 s with a total of 10 cycles

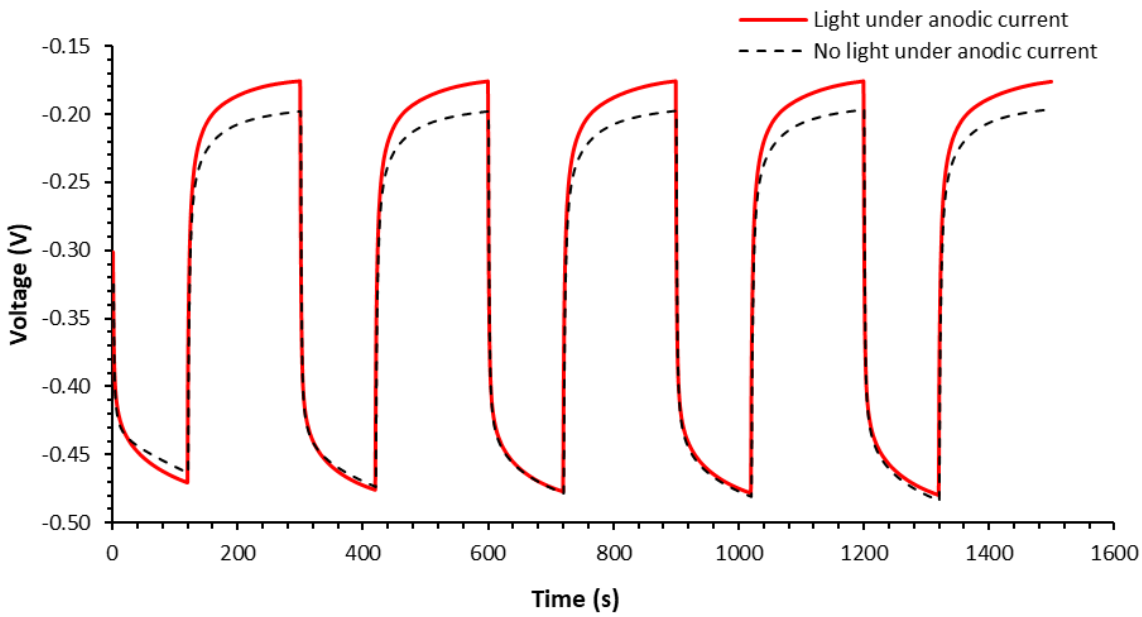

Figure 5.16 Constant current charge/discharge under light and no light condition for B doped TiO_2 electrode with an applied step current of 0.75 mA for 120 s and 0 mA for 180 s with a total of 10 cycles

Figure 5.15 illustrates chronopotentiometric graph of boron doped TiO_2 photoelectrode with a step current of 0.35 mA for 120 s and 0 mA for 180 s. The positive shift of 3 V is observed under light conditions. Similar behaviors are seen in Figure 5.16 when the step current is changed to 0.75 mA. The only difference is that discharge voltage stays at the same level for both light and under light conditions. The possible cause of this might be an experimental error since the system is charged from previous experiments. The voltage range is between -47 V and -18 V which is very similar to Carbon nanotube-TiO_2. As a result, it can be noted that in chronopotentiometric graphs shows stable charge-discharge behavior and proves that both of the photoelectrodes have good photo-response.

5.1.5 Potentiostatic scan

A potentiostatic scan is an electrochemical measurement technique which applies a continual potential to the working electrode and records the current as a function of time [66]. Figure 5.16 – 5.20 represents the potentiostatic scan test results for B-doped TiO_2, CNT-TiO_2, and stainless steel. Hydrogen is generated on the working electrode under a potentiostatic voltage of 1.8 V vs. Ag/AgCl under light and no light conditions for 30 minutes. It is observed that the response of the stainless steel working electrode to the applied potentiostatic voltage of 1.8 V under no light condition is almost the same with under light condition as expected in Figure 5.16 with an average current density of 111.45 mA /cm^2 and 112.51 mA /cm^2 respectively. Figure5.17 illustrates the response of the B-doped TiO_2 working electrode for potentiostatic scan at an applied voltage of 1.8 V vs Ag/AgCl during 30 minutes. The average current densities were calculated as 128.43 mA /cm^2 and 118.21 mA /cm^2 under light and no light conditions, respectively. It is seen that photocurrent generated under solar irradiance is higher compared to no light condition. Figure 5.18 shows the response of the CNT-TiO_2 working electrode for potentiostatic scan at an applied voltage of 1.8 V vs Ag/AgCl for 30 minutes. The average current densities were calculated as 164.73 mA /cm^2 and 152.33 mA /cm^2 under light and no light conditions, respectively. It is seen that photocurrent generated under solar irradiance is higher compared to no light condition. Figure 5.19 is presented to compare the coatings based on the amount of generated electric currents per unit area of cross section and it is clearly seen that CNT-TiO_2 shows better photocatalytic activity than B-doped TiO_2.

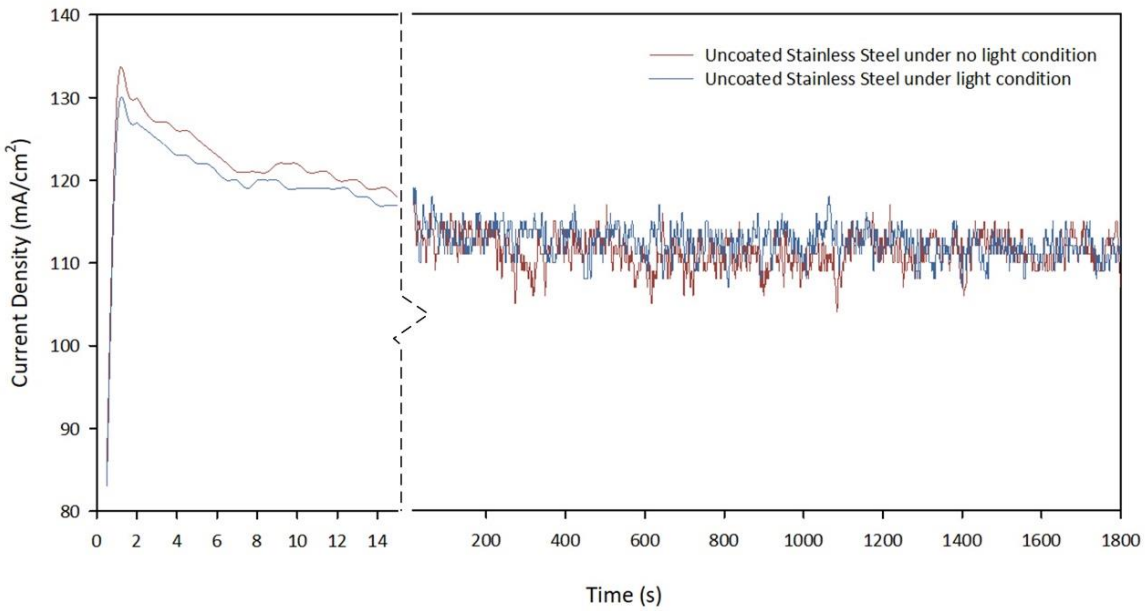

Figure 5.17 Potensiostatic curve for hydrogen production for stainless steel electrode in 0.05 NaOH solution at an applied voltage of 1.8 V vs Ag/AgCl under light and no light condition for 30 min.

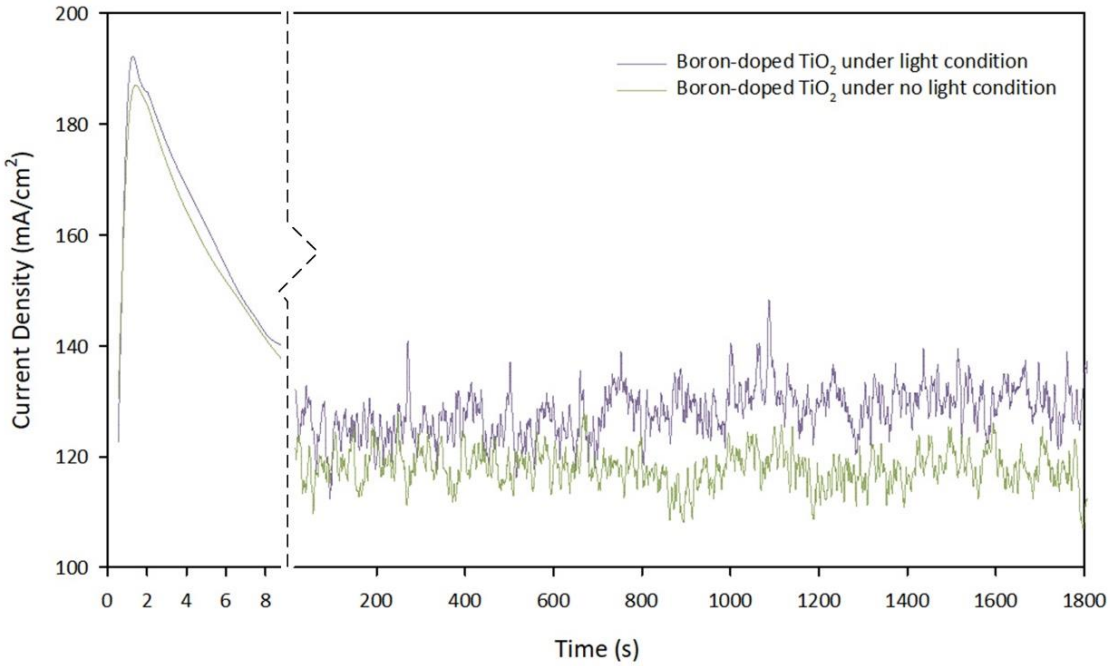

Figure 5.18 Potensiostatic curve for hydrogen production for B-doped TiO_2 electrode in 0.05 NaOH solution at an applied voltage of 1.8 V vs Ag/AgCl under light and no light condition for 30 min

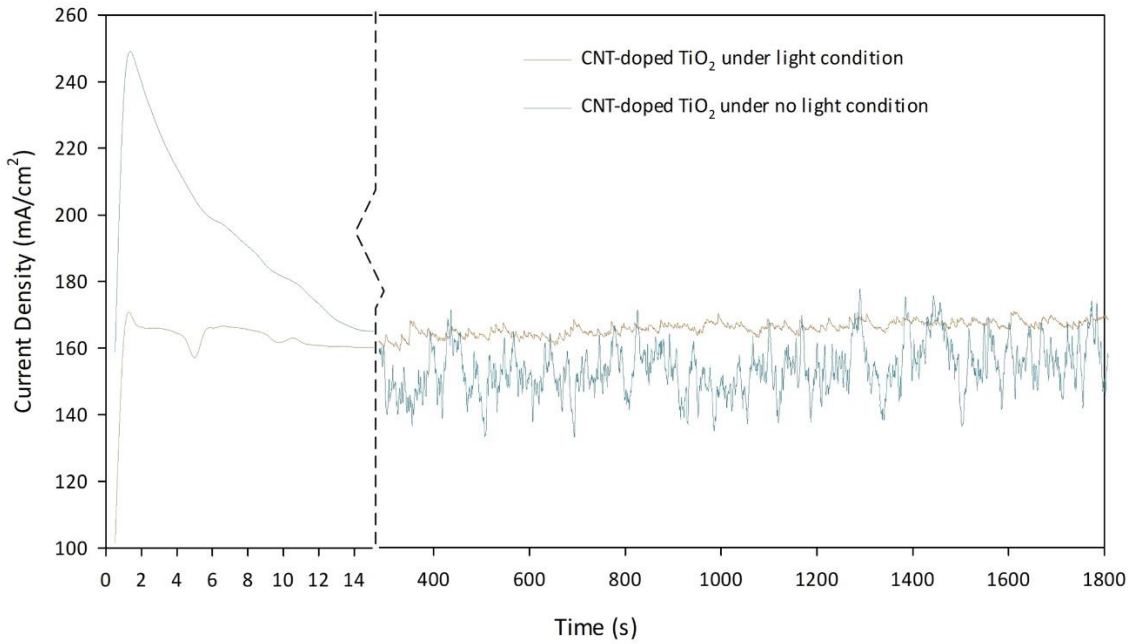

Figure 5.19 Potensiostatic curve for hydrogen production for CNT-TiO_2 electrode in 0.05 NaOH solution at an applied voltage of 1.8 V vs Ag/AgCl under light and no light condition for 30 min.

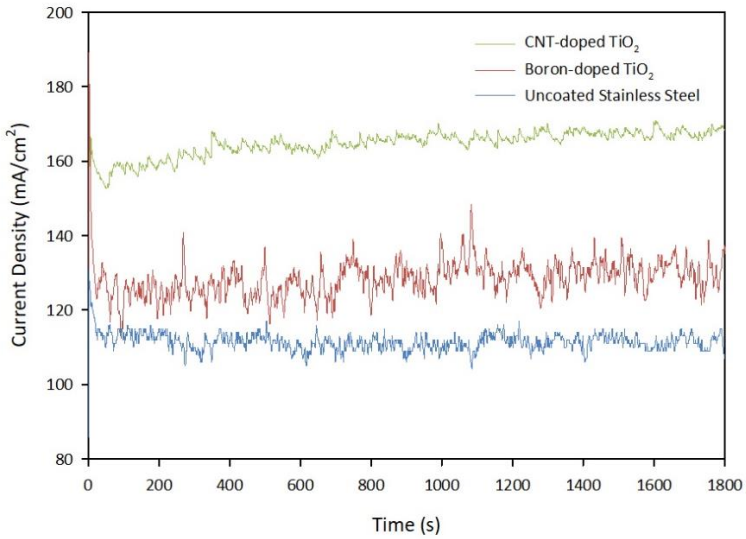

Figure 5.20 Comparison of the potensiostatic curve for hydrogen production of B-doped TiO_2, CNT-TiO_2 and stainless steel electrodes in 0.05 NaOH solution at an applied voltage of 1.8 V vs Ag/AgCl under light condition for 30 min.

Fig. 5.20 illustrates the measured hydrogen production rates under potentiostatic mode with light and no light conditions. It is noted that the amount of hydrogen produced under light condition is higher compared to no light condition for all samples. Also, the

amount of hydrogen produced by CNT-TiO_2 is 9.5 ml while it is 7.4 ml for B-doped TiO_2 and 4.4 ml for uncoated stainless steel under light condition after 30 minutes.

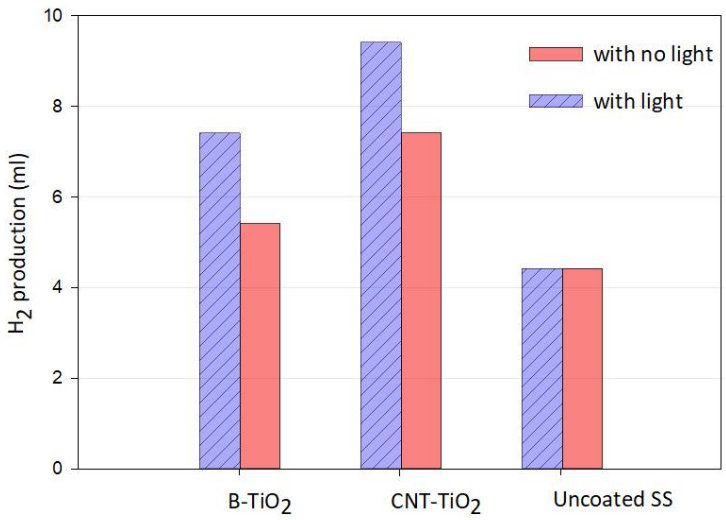

Figure 5.21 Hydrogen production rate for B-doped TiO_2, CNT-TiO_2 and stainless steel electrodes in 0.05 NaOH solution at an applied voltage of 1.8 V vs Ag/AgCl for 30 min. under light and no light conditions

5.1.6 Energy and Exergy Analyses Results

Figure 5.22 displays the results of the energy efficiency of the three different photoelectrode used in the experiments under UV light irradiation. It is found that boron doped TiO_2 and carbon nanotube TiO_2 have almost the same energy efficiency value with 54%. The uncoated photoelectrode (stainless steel) showed 37% energy efficiency. Although carbon nanotube-TiO_2 produced more hydrogen compared to boron doped TiO_2, its energy efficiency is almost the same with boron because the power consumed to produce that amount of hydrogen is also higher compared to boron. Faraday efficiency of the photoelectrochemical cell also calculated and it is found 69.7% for the three photoelectrode seniors because the faraday efficiency depends on the voltage and in this work the applied voltages are the same for each experiments. Energy efficiency of the photoelectrochemical cell cannot be higher than the theoretical value of the faraday efficiency so it can be concluded that the energy efficiencies of the hydrogen production experiments have lower value than the found faraday efficiency.

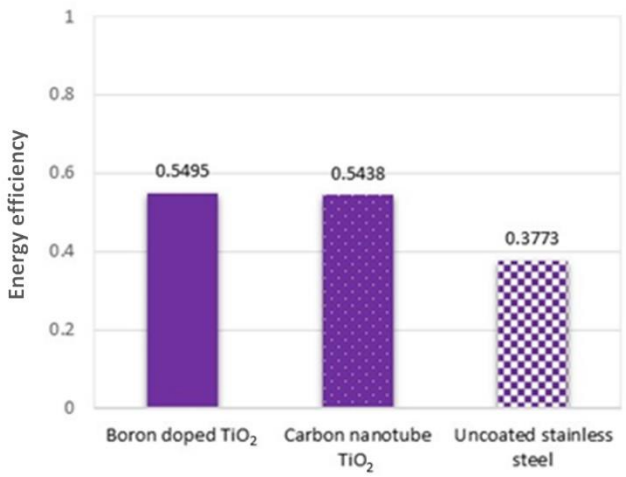

Figure 5.22 Energy efficiency of the considered electrodes.

Figure 5.23 shows the exergy efficiency results of the energy efficiency of the three different photoelectrodes used in the experiments under UV light irradiation for hydrogen production. Figure 5.23 shows that the cell that achieved the highest exergy efficiency is the cell with the boron doped TiO_2 coated electrode with 53.7%. Exergy efficiency of the carbon nanotube TiO_2 has an exergy efficiency of 53.2% while the exergy efficiency value of the uncoated stainless steel is 37.7%. The graph also shows that the photoelectrodes showed a great performance having a very close energy and exergy efficiencies when the operating and structural conditions are considered in this work, which leaves the coated electrodes with a higher range of improvement giving it more importance in the water splitting cell development and enhancement.

As a validation for the study we can see that the uncoated sample experience negligible change in performance under light and no light operations during the experiments which was the initial observation that have lead to the investigation of the reactors and the performance of the coated structures. Finally, as shown in Figure 5.22 and Figure 5.23 shows that although the CNT-TiO_2 coated electrode cell has produced the highest hydrogen production, it still performs the poorer than boron-doped TiO_2. The low performance of the CNT-TiO_2 coated cell can be referred to the high current density the cell operating at.

Figure 5.24 shows the exergy destruction rate of the electrolysis cell for the three different photoelectrodes under light condition. Figure 5.24 shows that the cell achieved

the highest exergy destruction rate was the cell with the CNT-TiO_2 coated electrode which was found to be 87.36 W. The lowest exergy destruction rate was achieved by the B doped TiO_2 coated electrode with 67.51 W. As for the benchmark uncoated electrode (stainless steel), the exergy destruction rate was found to be 79.81 W.

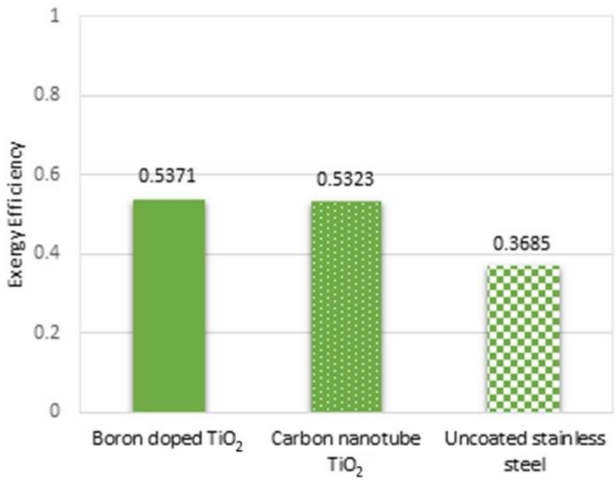

Figure 5.23 Exergy efficiency of the considered electrodes.

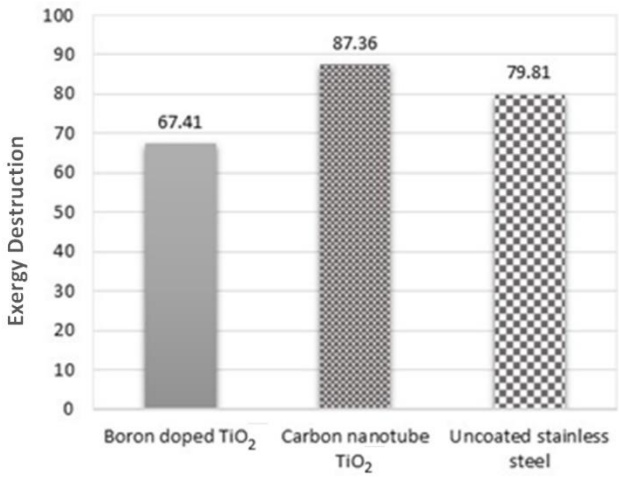

Figure 5.24 Exergy distraction rate of the considered electrodes.

5.2 Reactor Designs and Simulations

In this section, multiple reactor designs are being proposed based on the design methodology of increasing the flow of the formed hydrogen bubbles out of the reactor outlet. The chapter starts with simulating the current PEC reactor proposed and developed by Acar and Dincer [83] Bicer and Dincer [84], Hogerwaard [25], and Demir [66]. Then based on the results of the base design, new different designs are proposed and simulated

using COMSOL Multiphysics software which allows to design and simulate several engineering applications [85]. Finally, the best performing design in terms of accumulation of hydrogen and leaving the reactor is recommended for new PEC reactor.

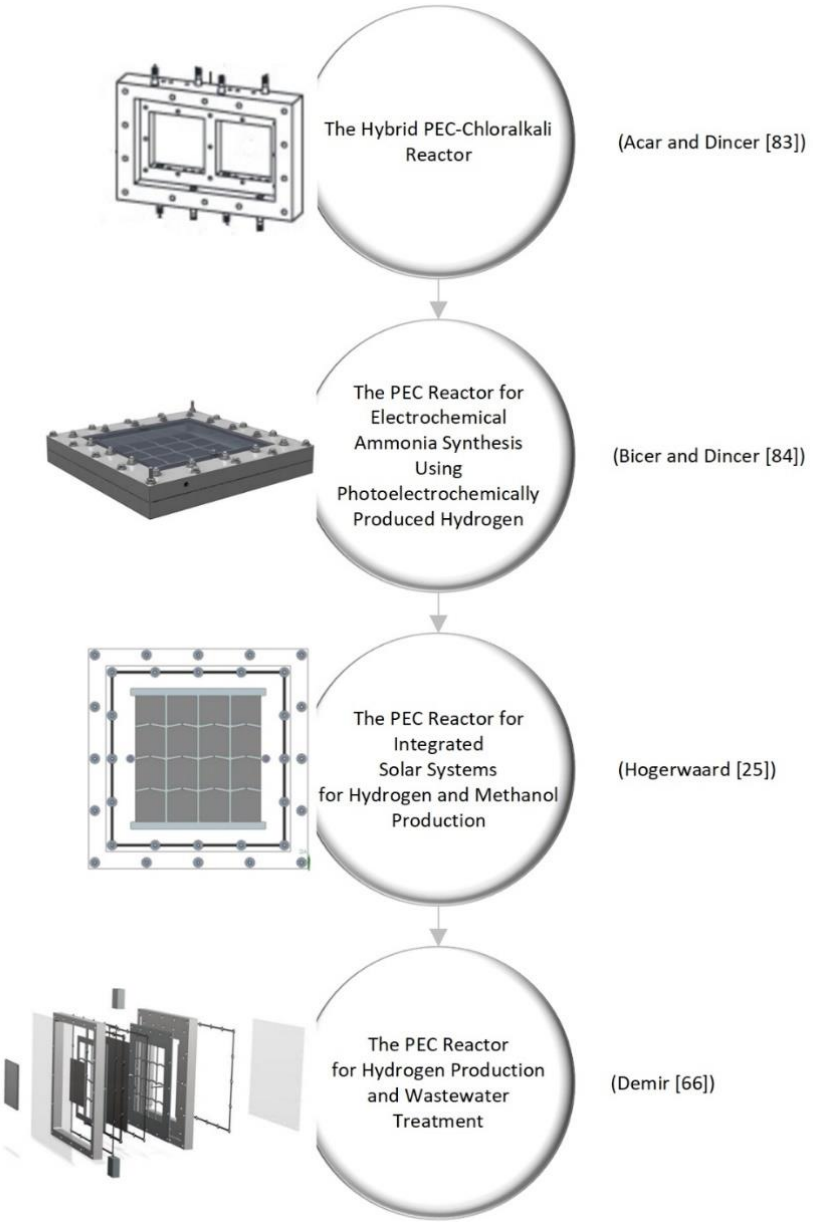

Figure 5.25 Photoelectrochemical hydrogen production researches using different PEC reactors built at the Clean Energy Research Laboratory (CERL) in UOIT.

The design of the electrolyzers is important in terms of allowing the hydrogen to leave the reactor as soon as it is generated and to avoid having the hydrogen forming

clusters that will interfere with the efficiency of the electrolyzers as well as the safety once it is being maintained [86].

Electrolyzers are independent on light to excite the coated electrodes, which means designing them is not dependent on having the coated electrode being accessible to light. Based on the design requirements of having the light accessible to the coated electrode different designs were considered for the PEC reactor.

Acar and Dincer [83] proposed a rectangular chamber based geometry where is a single output at each chamber. Furthermore, similar geometry for PEC reactor is used by Ghosh [86] and the disadvantage that was mentioned in these works were that the accumulation of hydrogen gas at the corners and the upper surface of the hydrogen production rectangular chamber side. The accumulation of hydrogen reduced the performance of the PEC reactor as well as proposed a safety concern when carrying maintenance on the reactor. Further studies considered upscaling the reactor as Bicer and Dincer [84], Hogerwaard [25] and Demir [66] have proposed a novel reactor design for photoelectrochemical water splitting for several applications as it can be seen in Figue 5.25. However, based on the literature review, few researchers considered the design of the PEC reactor in general in terms of the flow of the hydrogen formed bubbles within the reactor and how the hydrogen is collected. One of the few studies that considered the design of the PEC reactor is Carver et al. [63] With the new immerging technology of the PEC reactor this parts of the thesis work on filling the gap in the novel designs of PEC reactors considering the flow of the generated hydrogen bubbles and the collection of these bubbles as the produced hydrogen.

5.2.1 Mesh development of the two-phase flow study

In this section, the development of the mesh of the simulated geometry is presented. For the reactor modeling and the bubble flow simulation, the mesh has to be set so that accurate flow simulation of the natural raise of the bubbles is achieved without having extensive computational cost. The flow of the hydrogen bubbles upward through the reactor is simulated as a two-phase flow through the use of the laminar flow module and the level set module as presented in the model description presented earlier in the chapter.

For two-phase flow that is based on the level set method, the mesh selection should not violate the Courant Friedrichs Lewy (CFL) condition. The Courant Friedrichs Lewy condition, which was introduced by Courant, Friedrichs, and Lewy is that the time step set to solve the two-phase flow with the level set method should be set that the distance the bubble or a particle in a single time step is less than the dimension of the smallest element in the mesh as presented in the CFL condition as follows [88]:

$$CFL = \frac{|\vec{u}|\Delta t}{\Delta x} < 1 \tag{5.1}$$

Here, $|\vec{u}|$ denotes the absolute velocity of the bubble of the particle, Δt the time step of the simulation, and Δx presents the dimension of the mesh element. The time here defines the interval time length for the Navier Stokes convection step. In order to determine an acceptable mesh accuracy for the simulation, while minimizing the computational time especially since it a two phase flow problem, which is greatly time consuming process an iterative approach is considered to determine an appropriate mesh size for the simulated domain. By applying a force balance on a single bubble the resulting force balance is as follows:

$$F_B - m_{bu}g = m_{bu}a_{bu} \tag{5.2}$$

Here, F denotes force, m denotes mass, a is the acceleration and g is the gravitational acceleration. The subscript B refers to buoyancy and bu refers to the bubble. By solving for the acceleration of the bubble for the first moments since it is where the velocity will reach its maximum for the case where there is more than bubble and a surface on top of the bubble, which is concluded from the different iterations conducted to run the simulation. Based on the calculated maximum velocity at the first instant during the rise of the center bubbles the resulting mesh properties are presented in Table 5.2 Note that to support the selection of the final used mesh, it is first used in all three different designs and since the simulation is done for comparison purpose then it is accepted to use that mesh based on [88]. Note that the maximum element growth rate is set to accommodate the curved corners of the reactors with the curvature factor.

Table 5.2 The selected mesh properties and the time stepping method.

Property	Value or selected method
Maximum mesh element size	0.05 in
Minimum mesh element size	0.04 in
Maximum element growth rate	1.15
Curvature factor	0.3
Refined mesh option	ON
Maximum time step	0.01 s
Minimum time step	0.0001 s CFL = 0.612 at the maximum achieved velocity
Auto time stepping	ON
Method	BDF
Maximum/minimum BDF order	2/1
Consistent initialization	Backward Euler

5.2.2 Base design

The base design of the PEC reactor that was proposed and used in Acar and Dincer [83] has a rectangular chamber, the rectangular chamber is where the hydrogen is being formed as shown in Fig. 5.26. The reactor chambers have a single outlet for the hydrogen side and a single outlet at the other side of the membrane where the oxygen is being formed. The location, the size and the number of the outlets is one of the main determining steps in the design of the electrolyzer and play an important role in determining the flow of the formed hydrogen and its collection. For the reasons of comparison, all proposed designs will have a single collection channel as the previous generation of the proposed reactor.

Note that Figure 5.26 includes the considered mesh structure for simulated the design as well as the boundary conditions selected. Before explaining the selection of the boundary conditions, first the modeling of the simulated phenomena is explained.

As it can be seen clearly, almost all of the hydrogen bubbles reach the top of the reactor surface area whiting the first second. However, most of the hydrogen mass is getting trapped at the upper surface of the reactor and they are not flowing outside of the reactor through the pipe connected in the top middle area to be collected. This is mainly due to the poor design of the reactor by having sharp edges in the geometry not allowing for smooth traveling of the hydrogen bubbles out of the reactor instead of having hydrogen

accumulation at the top edge of the reactor which is considered a safety hazard and it affects the performance of the reactor.

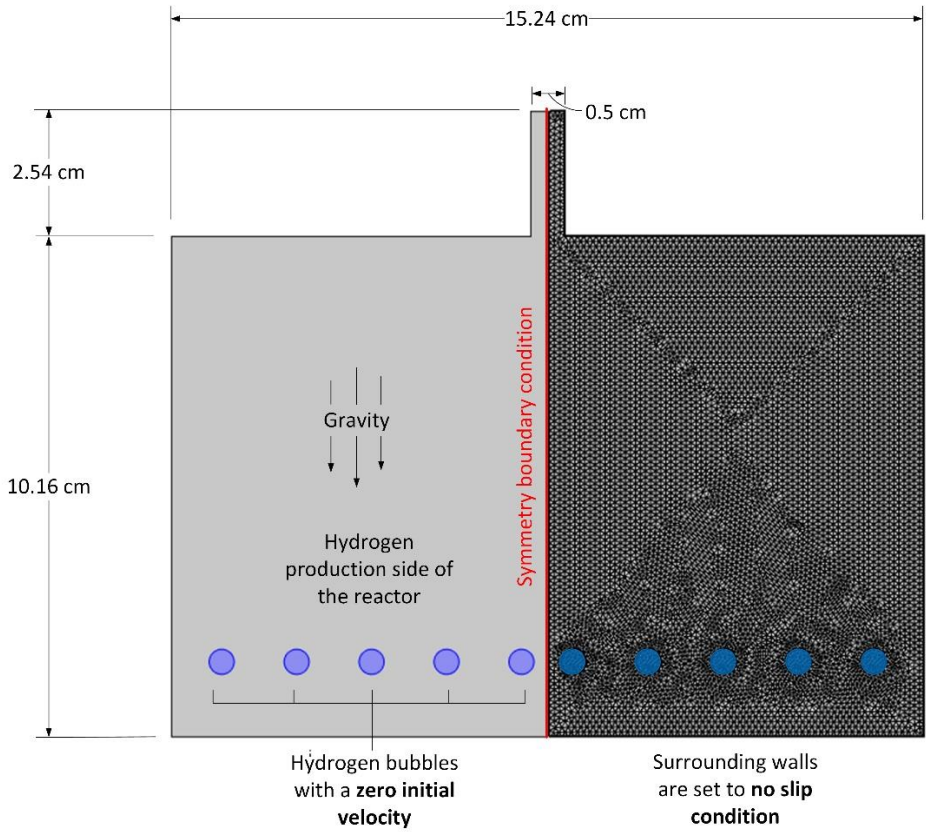

Figure 5.26 The selected boundary conditions and the detailed dimensions of the base design for the PEC reactor.

Fig. 5.30 shows the surface plot of the magnitude of the velocity at different points in time of the entire surface of the reactor during the total duration of the simulation of 2 seconds. The maximum velocity is 0.73 m/s when hydrogen bubbles first exit at second 0.1 and the velocity always has the minimum value at the bottom corners. As it can be seen after 1 second, vortices of relatively high speed are formed at the top edge of the rector which are the main cause of the accumulation of hydrogen bubbles in that area of the reactor because some of the separated flow comes about halfway back of the reactor. This might raise the risk of causing vibration within the reactor other than affecting the productivity of hydrogen bubbles since they are getting accumulated inside the reactor rather than being collected. That why the new design of the reactor is essential to allow for a smooth path for the formed hydrogen bubbles in the reactor to be extracted.

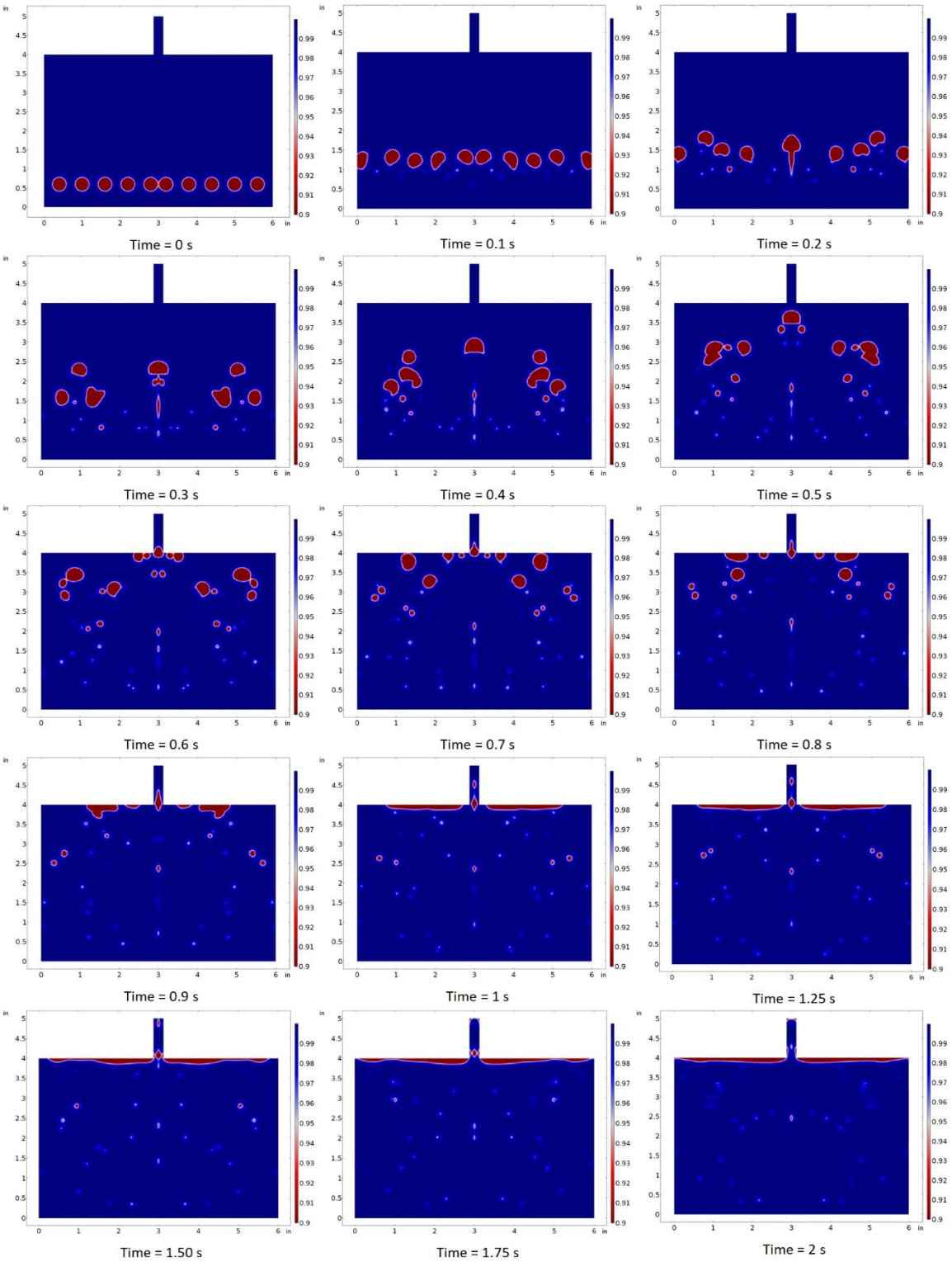

Figure 5.27 Surface plot of water volume fraction of the base (square) design at 0, 0.1, 0.2, 0.3, 0.4, 0.5, 0.6, 0.7, 0.8, 0.9, 1.0, 1.25, 1.50, 1.75 and 2.0 seconds.

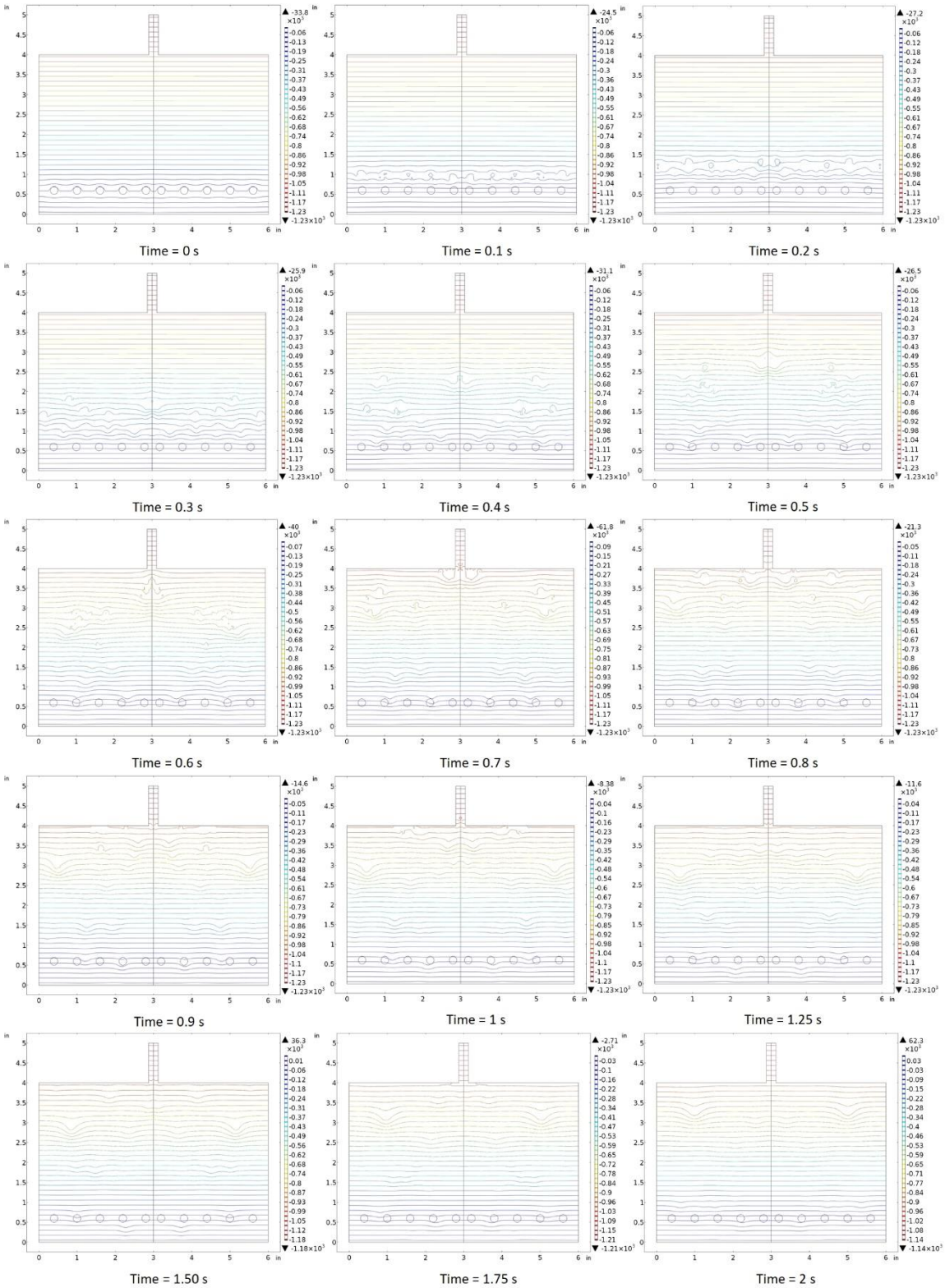

Figure 5.28 Contour plot of pressure (Pa) of the base (square) design at 0, 0.1, 0.2, 0.3, 0.4, 0.5, 0.6, 0.7, 0.8, 0.9, 1.0, 1.25, 1.50, 1.75 and 2.0 seconds.

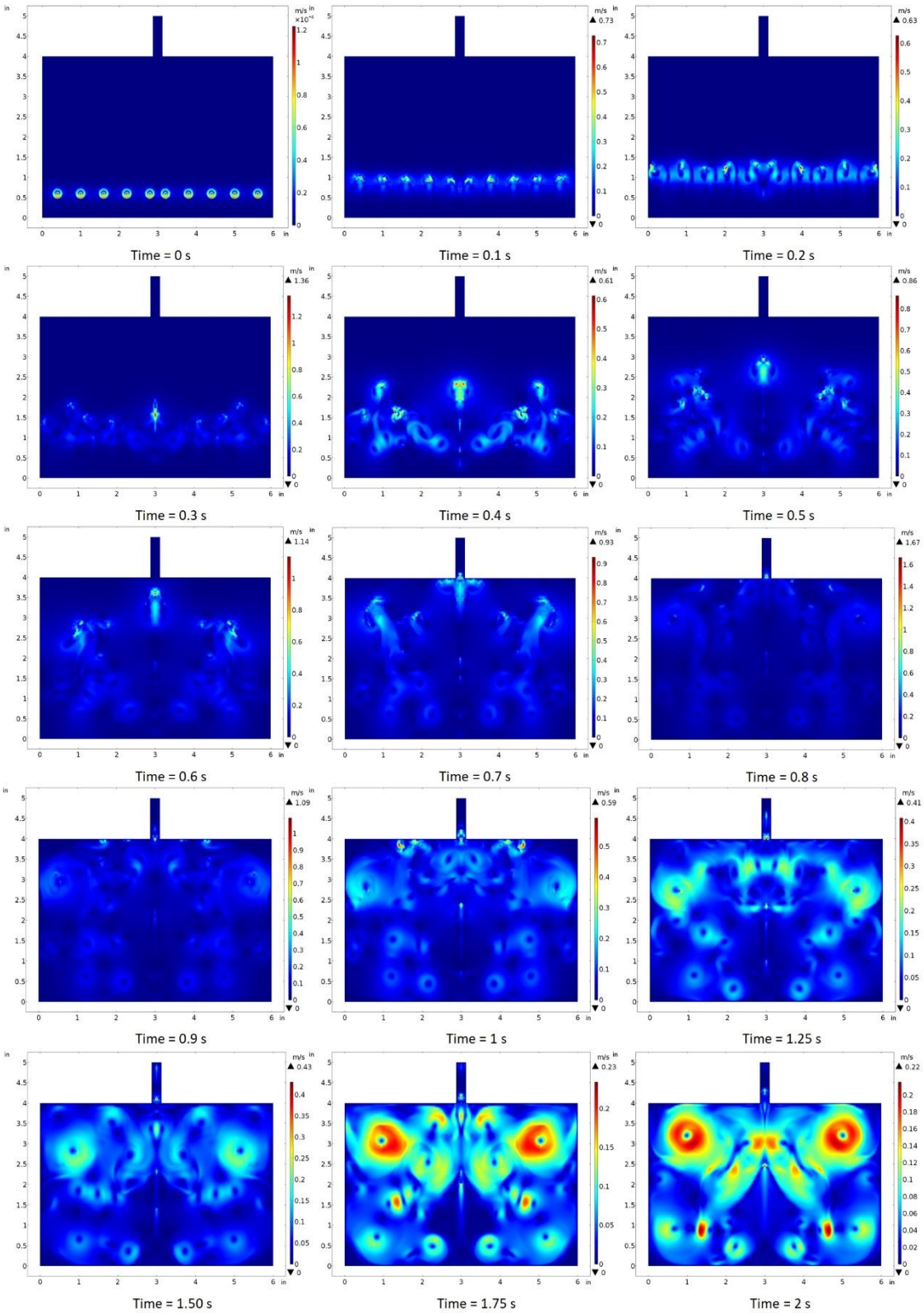

Figure 5.29 Surface plot of velocity magnitude (m/s) of the base (square) design at 0, 0.1, 0.2, 0.3, 0.4, 0.5, 0.6, 0.7, 0.8, 0.9, 1.0, 1.25, 1.50, 1.75 and 2.0 seconds.

5.2.3 Proposed designs

This section introduces the proposed designs modeling methodology and boundary conditions. The section also includes the designing methodology of the different proposed designs and how the various designs are being developed.

The designs are being developed through investigating the original design and then to change the geometry in the aim to minimize the trap of bubbles at different locations through the reactor. The work aims to achieve optimum design through two iterations and then provide a recommendation on how to further enhance the model for future work.

5.2.3.1 First iteration design

After the results of the base design presented earlier, the first iteration of the proposed design is developed and it is shown in Fig. 5.31.

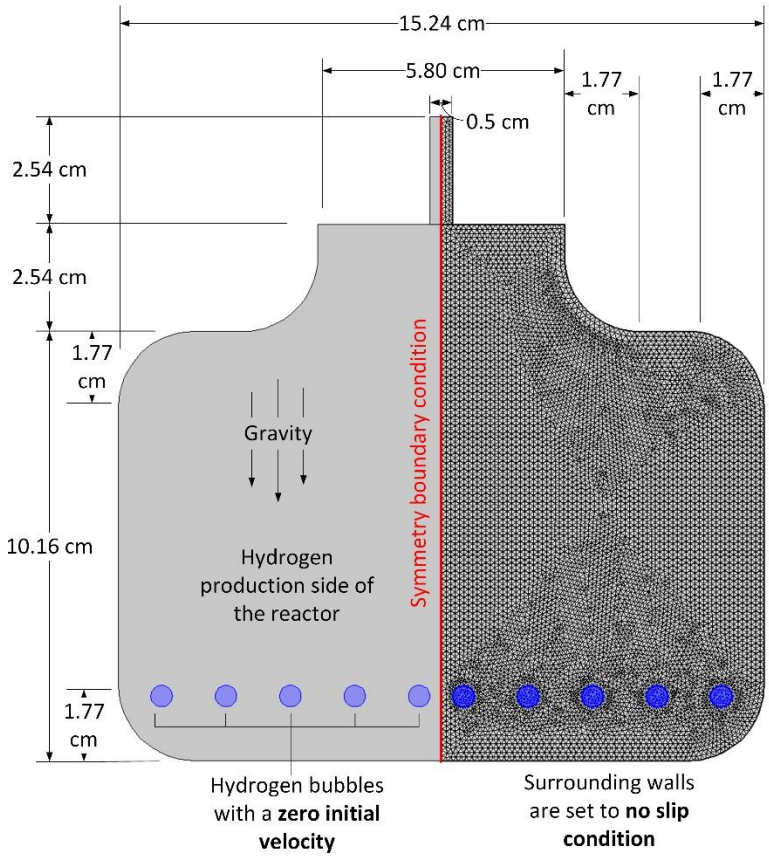

Figure 5.30 The selected boundary conditions and the detailed dimensions of the first iteration of the proposed designs for the reactor.

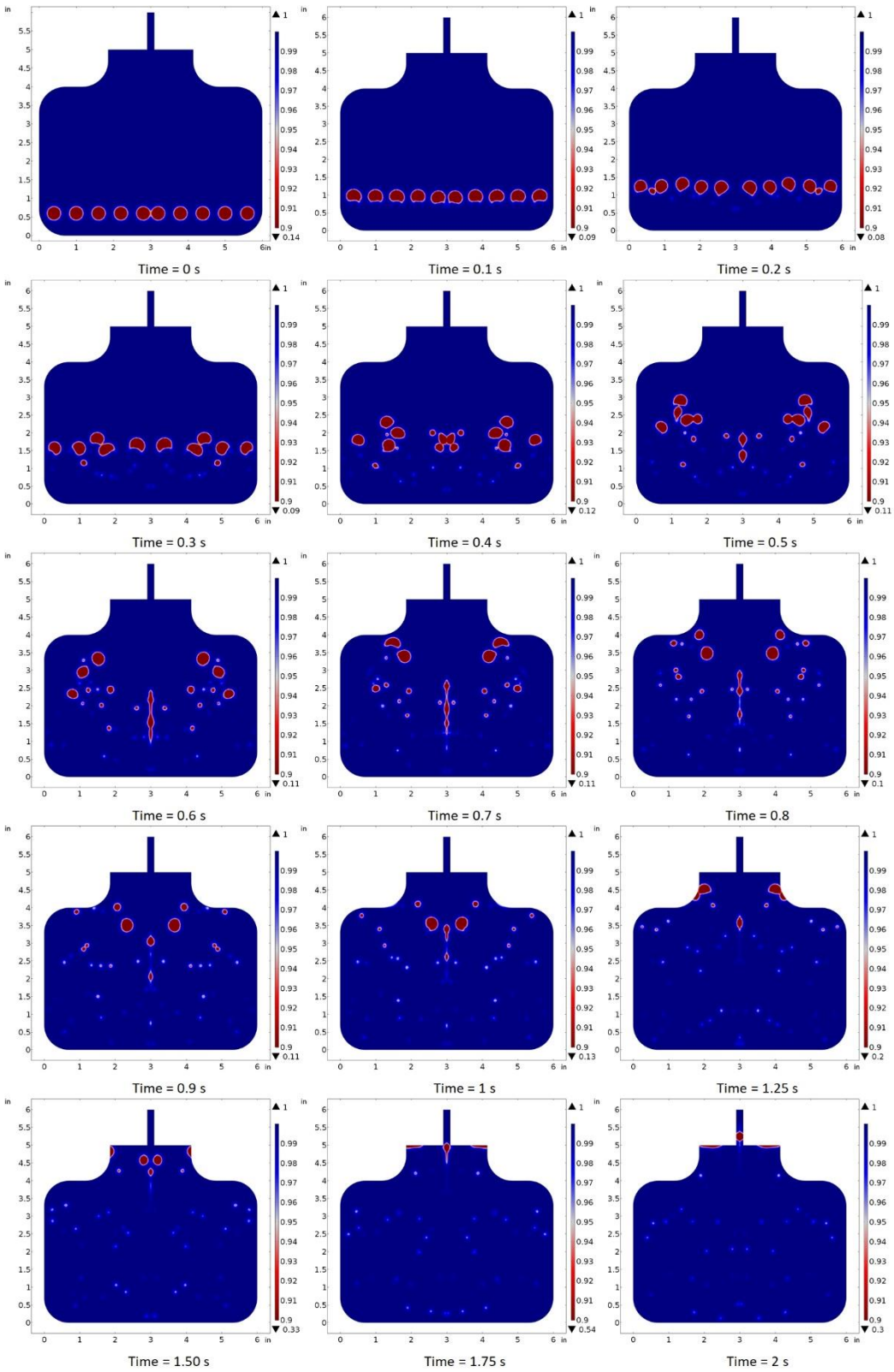

Figure 5.31 Surface plot of water volume fraction of the first iteration design at 0, 0.1, 0.2, 0.3, 0.4, 0.5, 0.6, 0.8, 0.9, 1, 1.25, 1.50, 1.75 and 2 seconds.

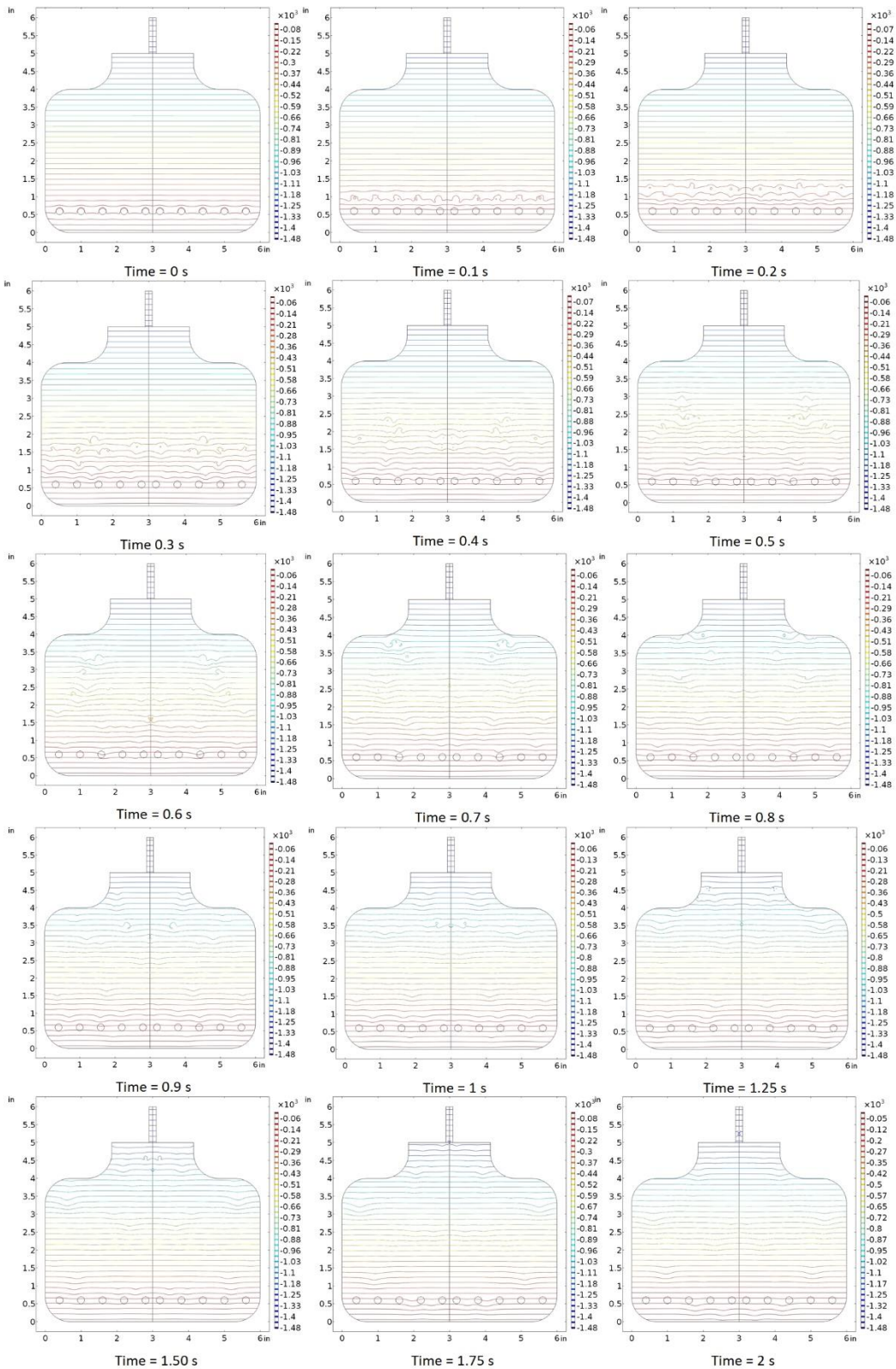

Figure 5.32 Contour plot of pressure (Pa) of the first iteration design.

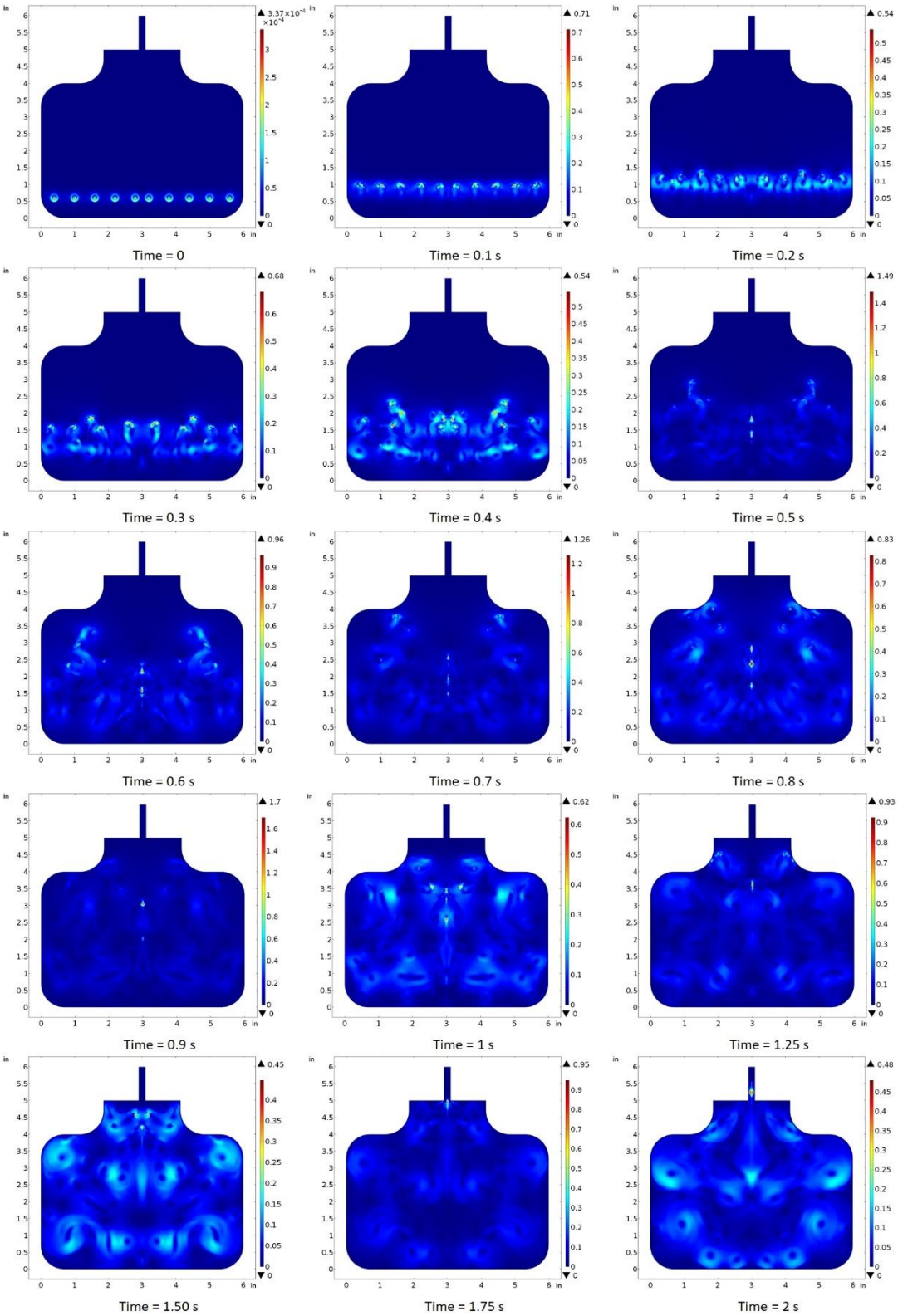

Figure 5.33 Surface plot of velocity magnitude (m/s) of the first iteration design.

Figure 5.32 shows the flow of the bubbles at different points in time by plotting the phase fraction of the entire surface of the reactor during the total duration of the simulation which is 2 seconds. It's clear that compared to the base design, this suggested geometry helps is aiding most of the initial hydrogen mass within the reactor to travel outside of it by having smooth top corners instead of the sharp ones in the base design. After 1.75 seconds, almost all of the hydrogen bubbles are being collected through the opening on the middle top part of the reactor. However, it's obvious from the movement direction of the hydrogen bubbles in the velocity graphs that after 2 seconds, some of the hydrogen bubbles are being trapped at the sharp corners of the exit in which the hydrogen should flow through since they have sharp edges.

Figure 5.34 shows the surface plot of the magnitude of the velocity at different points in time of the entire surface of the reactor during the total duration of the simulation of 2 seconds. The maximum velocity is 0.71 m/s when hydrogen bubbles first exit at second 0.1 which is almost the same with the base design and the velocity always has the minimum value at the bottom corners and the upper edges. Comparing the first 2 seconds with the base design shows clearly how much improvement is made in terms of having a smooth transition flow of the hydrogen inside the reactor to the outlet that's possible by the new design. However, vertices again start to from after that cause some hydrogen bubbles to be trapped at the edges of the reactor outlet. Even though they are not as bad as the vertices formed inside the reactor of the base design. So, we can conclude in order to improve the design further, those corners must be again either eliminated or made smoother to improve the collection of more hydrogen within a shorter period of time.

5.2.3.2 Second Iteration Design

The second iteration is the improved reactor design based on understanding the results and the disadvantages we found in the first iteration. Fig. 5.35 illustrates the selected boundary conditions and the detailed geometry design of the second iteration.

Fig. 5.36 shows the flow of the bubbles at different points in time by plotting the phase fraction of the entire surface of the reactor during the total duration of the simulation which is 2 seconds. It's evident that when comparing this iteration with the first one that

by looking at the phase fraction figures after 1.5 seconds, less hydrogen is still presented in the reactor design of the second iteration compared to the first one, which means less time required to collect the hydrogen outside of the reactor. In addition, it's noticeable that less hydrogen mass will be trapped at the top surface of the reactor after 2 seconds for the second iteration design compared to the first. Fig. 5.38 shows the surface plot of the magnitude of the velocity at different points in time of the entire surface of the reactor during the total duration of the simulation of 2 seconds. Similar to the behavior shown in Fig. 5.34 for the first iteration design, vortices start to form after 1.75 seconds. However, the magnitude of the velocity inside the reactor of the second iteration design is lower that the first iteration design as shown in the surface plots figures for the velocity magnitude. For example, the maximum value of the magnitude of the velocity for the second iteration design is 0.26 m/s compared to 0.48 m/s in the first iteration design at 2 seconds.

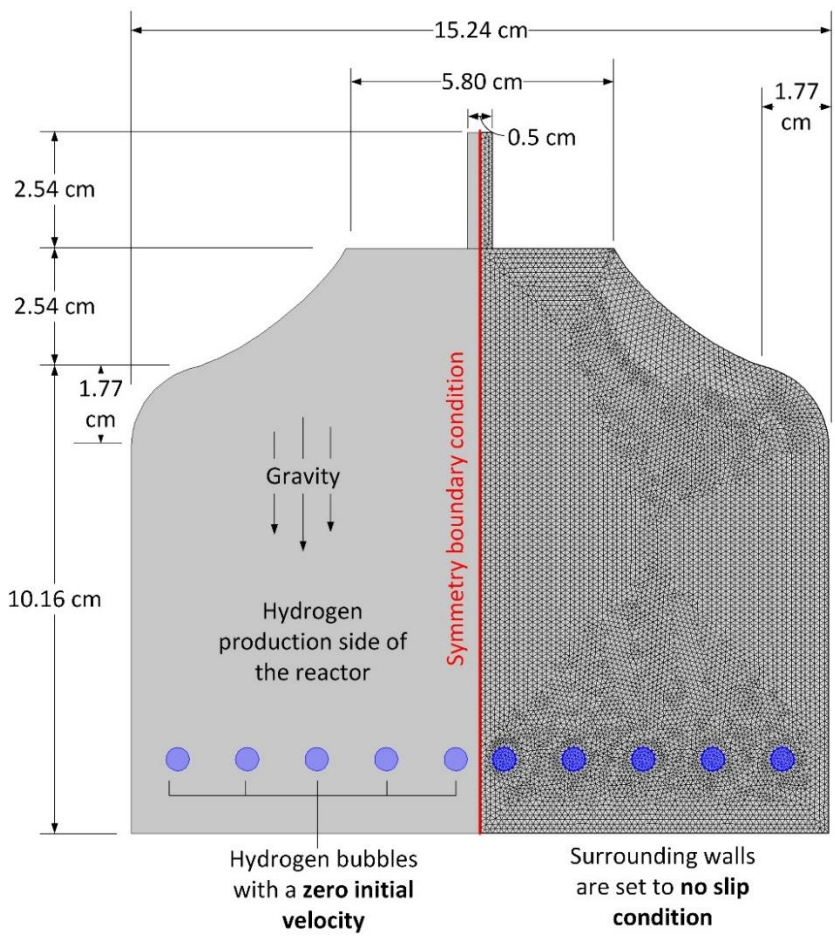

Figure 5.34 The selected boundary conditions and the detailed dimensions of the second iteration of the proposed designs for the reactor.

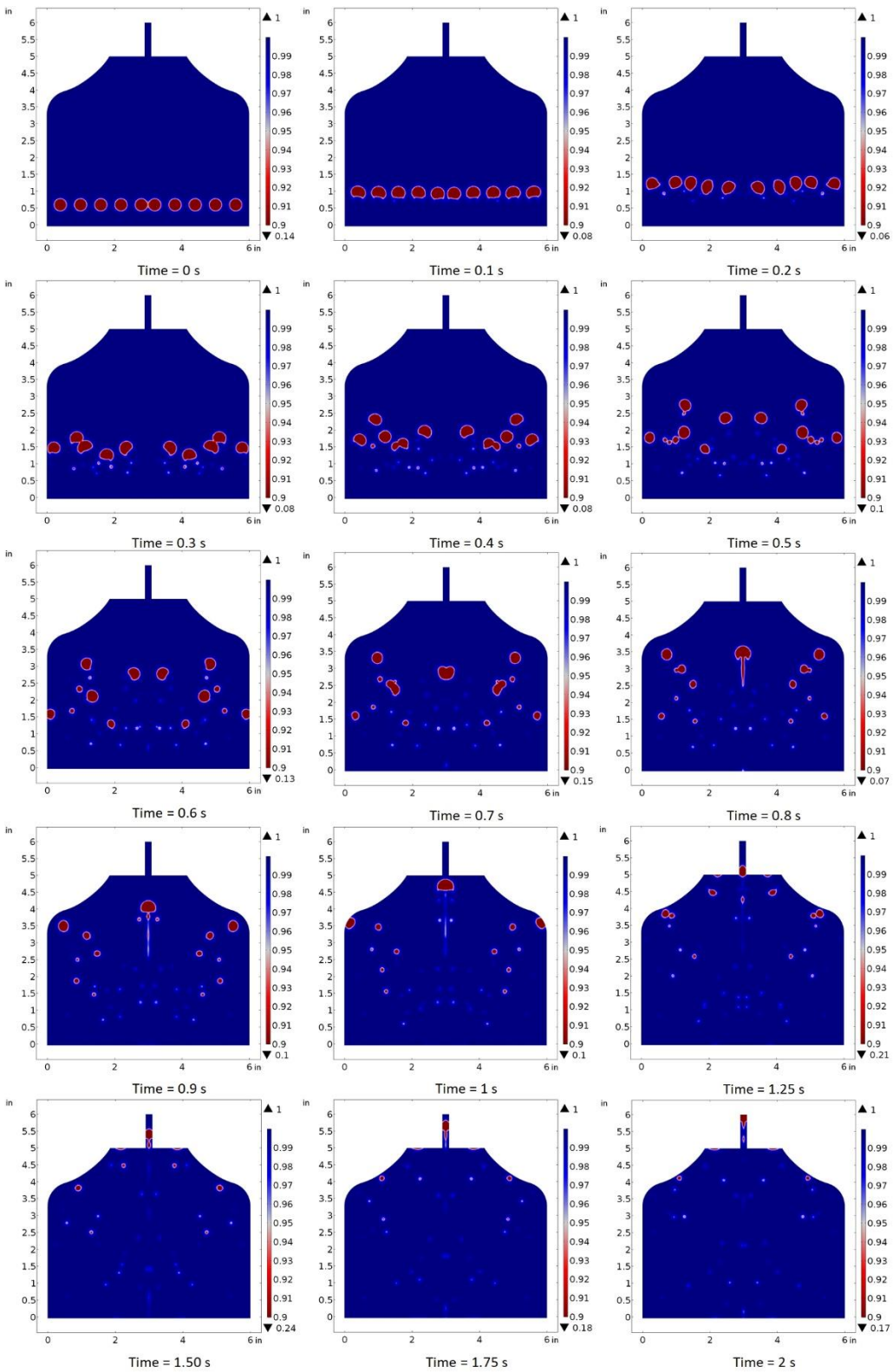

Figure 5.35 Surface plot of water volume fraction of the second iteration design at 0, 0.1, 0.2, 0.3, 0.4, 0.5, 0.6, 0.8, 0.9, 1, 1.25, 1.50, 1.75 and 2 seconds.

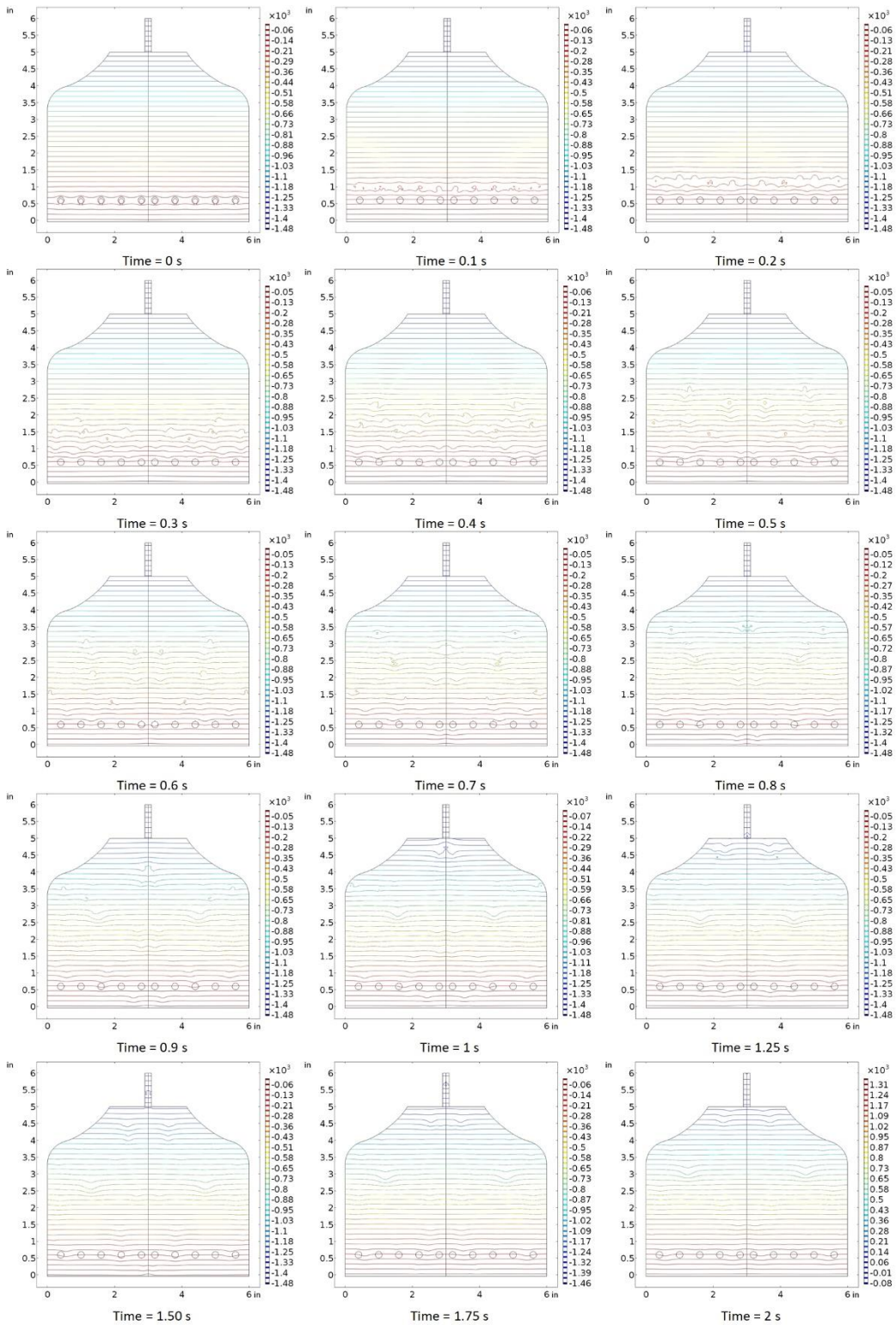

Figure 5.36 Contour plot of pressure (Pa) of the second iteration design.

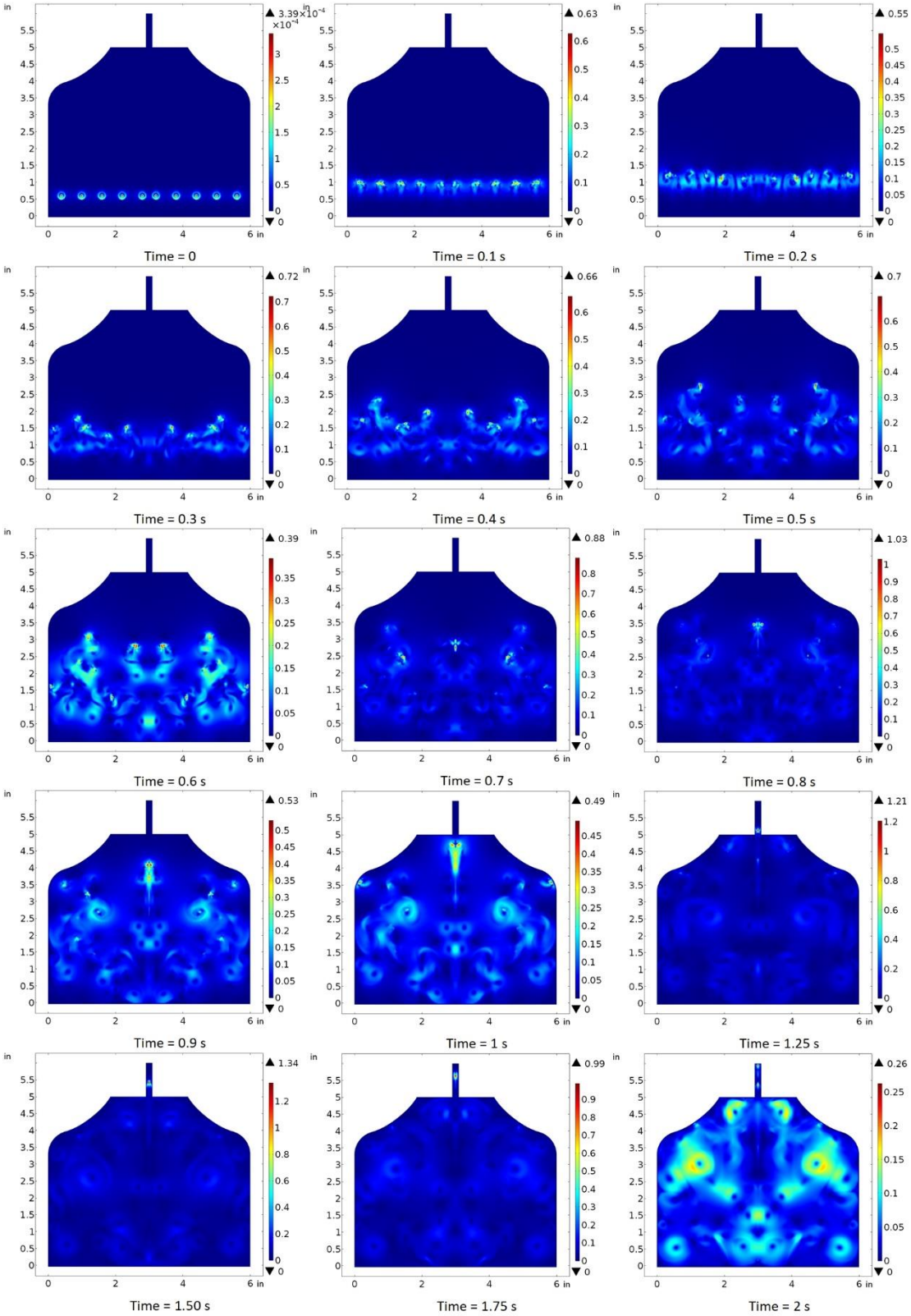

Figure 5.37 Surface plot of velocity magnitude (m/s) of the first iteration design.

5.2.3.3 Designs comparison

The most important criteria to be looked at when comparing the base, square design of the reactor with the two suggested design is that how much hydrogen can flow out of the reactor to be collected in less time. Figure 5.39 shows the variation of the area of hydrogen bubbles in the reactor over time. The area of the hydrogen bubbles is calculated throughout surface integration of the reactor area excluding the outlet pipe. In theory, the optimum design is the one that allows all the hydrogen to leave, which means that the area of the hydrogen bubbles should be zero after a certain time. In addition, the time taken to accomplish this is an important factor to be considered when comparing the different designs since the accumulated hydrogen can cause a pressure build up and manifest the safety concerns. As it's evident in Figure 6.14, the rate of hydrogen escaping the reactor decreases over time. After around the first 1.5 seconds, the amount of hydrogen is almost in a steady state position and stays constant inside the reactor. However, it's noticeable that design 2 results in the least amount of hydrogen in the reactor after 1 seconds compared to the first design iteration and the base square design. Initially, the hydrogen content for the three suggested designs is 1.19 cm^2 . After 2 seconds, the surface area of the hydrogen that is still trapped in the reactor is 0.078 cm^2 in first proposed design and to 0.0581 cm^2 in second proposed design. The improvement achieved in hydrogen released is 32.5% and 34.9% compared to the base design for first and second proposed designs, respectively.

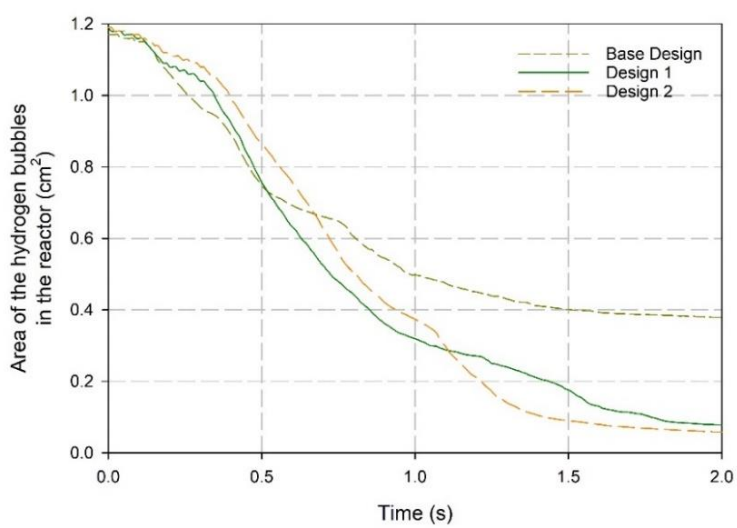

Figure 5.38 Area of the hydrogen bubbles in the base and proposed reactor designs variation with time

Chapter 6: Conclusions and Recommendations

In this chapter, conclusions which are based on the key findings of the experimental study are presented and recommendations are provided for future work.

6.1 Conclusions

This study focuses on experimental investigations of photocatalytic hydrogen production with boron doped TiO_2 and carbon nanotube-TiO_2 coated photoelectrodes. A small scale photoelectrochemical reactor is developed for both hydrogen production and the characterization in order to apply electrochemical techniques.

- The average current densities generated under potentiostatic scan for uncoated stainless steel, boron-doped TiO_2 and carbon nanotube-TiO_2 working electrodes are observed to be 112.51 mA /cm^2, 128.43 mA /cm^{2,} and 164.73 mA /cm^2 under UV light respectively.
- Overall energy and exergy efficiencies of the boron doped TiO_2 photoelectrode under UV light conditions are found 54.9% and 53.7%, respectively. Also, overall energy and exergy efficiencies of the carbon nanotube-TiO_2 photoelectrode under UV light conditions are found 54.3% and 53.2% while uncoated stainless steel has 36.7% and 36.8% energy and exergy efficiencies, respectively.
- The three reactor designs are modeled and simulated on COMSOL Multi-physics software. The amount of hydrogen at the surface of the reactor for the base design is found $1.19\ cm^2$ which drops to $0.078\ cm^2$ in first proposed design and to $0.0581\ cm^2$ in second proposed design. The improvement achieved in hydrogen released is 32.5% and 34.9% compared to the base design for first and second proposed designs, respectively.

6.2 Recommendations

Based on the presented study, the following recommendations would be helpful for future studies:

- Boron-doped TiO_2 and carbon nanotube – TiO_2 should be prepared with same molar ratio and different coating techniques such as spin coating, hydrothermal and chemical vapor deposition to use in the photoreactor for comparative evaluation of hydrogen production to analyze the effect of coating techniques on the photocatalytic activity.
- Because the photocatalytic quality of the coated TiO_2 varies with different conditions, studying with different layer thickness, sample size, irradiated area and light intensity can be beneficial to understand the photocatalytic quality and the resistance mechanism of the samples.
- An experimental study of photoelectrodes with a proposed reactor design should be performed and hydrogen production rates should be investigated.
- Modeling and simulating the conducted electrochemical experiments in COMSOL to compare experimental and theoretical results.

References

[1] BP p.l.c. *BP Energy Outlook: 2019 edition*. London, United Kingdom, June, 2018. Website: Accessed on April 12, 2019.

[2] International Energy Agency. *Key world energy statistics*. Paris: International Energy Agency, 2018. Website: Accessed on December 27, 2018.

[3] International Energy Agency. *Key world energy statistics*. Paris: International Energy Agency, 2014. Website: Accessed on December 27, 2018.

[4] International Energy Agency. *Key world energy statistics*. Paris: International Energy Agency, 2010. Website: (Available from:

http://www.indiaenvironmentportal.org.in/files/key_stats_2010.pdf).

Accessed on December 27, 2018.

[5] International Energy Agency. *Key world energy statistics*. Paris: International Energy Agency, 2006. Website: Accessed on December 27, 2018.

[6] Muradov, Nazim Z., and T. Nejat Veziroğlu. "“Green” path from fossil-based to hydrogen economy: an overview of carbon-neutral technologies." *International journal of hydrogen energy*33.23, 2008, 6804-6839.

[7] Balat, Mustafa. "Potential importance of hydrogen as a future solution to environmental and transportation problems." *International journal of hydrogen energy* 33.15, 2008 4013-4029.

[8] Markandya, Anil, and Paul Wilkinson. "Electricity generation and health." *The lancet* 370.9591, 2007, 979-990.

[9] Acar, Canan, Ibrahim Dincer, and Greg F. Naterer. "Review of photocatalytic water-splitting methods for sustainable hydrogen production." *International Journal of Energy Research* 40.11, 2016, 1449-1473.

[10] Dincer, Ibrahim. "Exergetic and sustainability aspects of green energy systems." *CLEAN–Soil, Air, Water* 35.4, 2007, 311-322.

[11] Awad, Ali H., and Nejat Veziroğlu. "Hydrogen versus synthetic fossil fuels." *International journal of hydrogen energy* 9.5, 1984, 355-366.

[12] Dincer, Ibrahim. "Green methods for hydrogen production." *International journal of hydrogen energy* 37.2, 2012, 1954-1971.

[13] Zamfirescu, Calin, and Ibrahim Dincer. "Environmentally-benign hydrogen production from ammonia for vehicles." *Proceedings of Global Conference on Global Warming. July*. 2008.

[14] Balta, M. Tolga, Ibrahim Dincer, and Arif Hepbasli. "Thermodynamic assessment of geothermal energy use in hydrogen production." *International Journal of hydrogen energy* 34.7, 2009, 2925-2939.

[15] Balta, M. Tolga, Ibrahim Dincer, and Arif Hepbasli. "Potential methods for geothermal-based hydrogen production." *international journal of hydrogen energy* 35.10, 2010, 4949-4961.

[16] Gandia, Luis M., Gurutze Arzamedi, and Pedro M. Diéguez, eds. *Renewable hydrogen technologies: production, purification, storage, applications and safety*. Elsevier B.V., 2013.

[17] Nikolaidis, Pavlos, and Andreas Poullikkas. "A comparative overview of hydrogen production processes." *Renewable and sustainable energy reviews* 67, 2017, 597-611.

[18] Dincer, Ibrahim, and Canan Acar. "Review and evaluation of hydrogen production methods for better sustainability." *International journal of hydrogen energy* 40.34, 2015, 11094-11111.

[19] Dincer, Ibrahim, and Anand S. Joshi. *Solar Based Hydrogen Production Systems*. Springer, New York, NY, 2013.

[20] Fischer, M. "Review of hydrogen production with photovoltaic electrolysis systems." *International Journal of Hydrogen Energy* 11.8, 1986, 495-501.

[21] Bilgen, Ertugrul. "Solar hydrogen from photovoltaic-electrolyzer systems." *Energy conversion and management* 42.9, 2001, 1047-1057. *Energy Conversion and Management*. Web.

[22] Jia, Jieyang, et al. "Solar water splitting by photovoltaic-electrolysis with a solar-to-hydrogen efficiency over 30%." *Nature communications* 7 2016, 13237. *Nature Communications*. Web.

[23] Gibson, Thomas L., and Nelson A. Kelly. "Optimization of solar powered hydrogen production using photovoltaic electrolysis devices." *International journal of hydrogen energy* 33.21, 2008, 5931-5940.

[24] Yilanci, Ahmet, Ibrahim Dincer, and Hasan K. Ozturk. "A review on solar-hydrogen/fuel cell hybrid energy systems for stationary applications." *Progress in energy and combustion science* June 2009, 231-244.

[25] Hogerwaard, Janette. "*Development and Investigation of Integrated Solar Systems for Hydrogen and Methanol Production."* University of Ontario Institute of Technology, 2018.

[26] Steinfeld, Aldo. "Solar thermochemical production of hydrogen—a review." *Solar energy* 78.5, 2005, 603-615.

[27] Dincer, Ibrahim. "Green methods for hydrogen production." *International journal of hydrogen energy* 37.2, 2012, 1954-1971.

[28] Doenitz, W., et al. "Hydrogen production by high temperature electrolysis of water vapour." *International Journal of Hydrogen Energy* 5.1, 1980, 55-63.

[29] Ozturk, Murat, and Ibrahim Dincer. "Thermodynamic analysis of a solar-based multi-generation system with hydrogen production." *Applied Thermal Engineering* 51.1-2, 2013, 1235-1244.

[30] Steinfeld, Aldo. "Solar hydrogen production via a two-step water-splitting thermochemical cycle based on Zn/ZnO redox reactions." *International Journal of Hydrogen Energy* 27.6, 2002, 611-619.

[31] Eroglu, Ela, and Anastasios Melis. "Photobiological hydrogen production: recent advances and state of the art." *Bioresource technology* 102.18, 2011, 8403-8413.

[32] Asada, Yasuo, and Jun Miyake. "Photobiological hydrogen production." *Journal of Bioscience and Bioengineering* 88.1, 1999, 1-6.

[33] Hisatomi, Takashi, Jun Kubota, and Kazunari Domen. "Recent advances in semiconductors for photocatalytic and photoelectrochemical water splitting." *Chemical Society Reviews* 43.22, 2014, 7520-7535.

[34] Ismail, Adel A., and Detlef W. Bahnemann. "Photochemical splitting of water for hydrogen production by photocatalysis: a review." *Solar Energy Materials and Solar Cells* 128, 2014, 85-101.

[35] Chen, Zhebo, Huyen N. Dinh, and Eric Miller. *Photoelectrochemical water splitting*. New York: Springer, 2013.

[36] Li, Jiangtian, and Nianqiang Wu. "Semiconductor-based photocatalysts and photoelectrochemical cells for solar fuel generation: a review." *Catalysis Science & Technology* 4.12, 2014, 4440-4440.

[37] Grätzel, Michael. “Photovoltaic and Photoelectrochemical Conversion of Solar Energy.” *Philosophical Transactions of the Royal Society A: Mathematical, Physical and Engineering Sciences* 365.1853, 2007, 993–1005.

[38] Walter, Michael G., et al. "Solar water splitting cells." *Chemical reviews* 110.11,

2010, 6446-6473.

[39] van de Krol, Roel, Yongqi Liang, and Joop Schoonman. "Solar hydrogen production with nanostructured metal oxides." *Journal of Materials Chemistry* 18.20, 2008, 2311-2320.

[40] Brattain, Walter H., and C. G. B. Garrett. "Surface Properties of Germanium and Silicon." *Annals of the New York Academy of Sciences* 58.6, 1954, 951-958.

[41] Fujishima, Akira, and Kenichi Honda. "Electrochemical Photolysis of Water at a Semiconductor Electrode." *Nature* 238.5358, 1972, 37–38

[42] Zamfirescu, Calin, Greg F. Naterer, and Ibrahim Dincer. "Solar Light–Based Hydrogen Production Systems." *Encyclopedia of Energy Engineering and Technology-Four Volume Set*. CRC Press, 2014, 1722-1744.

[43] Ni, Meng, et al. "A review and recent developments in photocatalytic water-splitting using TiO2 for hydrogen production." *Renewable and Sustainable Energy Reviews* 11.3, 2007, 401-425.

[44] Fujishima, Akira, Xintong Zhang, and Donald A. Tryk. "TiO2 photocatalysis and related surface phenomena." *Surface science reports* 63.12, 2008, pp. 515-582.

[45] Li, Zhaosheng, et al. "Photoelectrochemical cells for solar hydrogen production: current state of promising photoelectrodes, methods to improve their properties, and outlook." *Energy & Environmental Science* 6.2, 2013, pp. 347-370.

[46] Moon, Sang-Chul, et al. "Photocatalytic production of hydrogen from water using TiO2 and B/TiO2." *Catalysis Today*58.2-3, 2000, 125-132.

[47] Khan, Romana, et al. "Comparative study of the photocatalytic performance of boron–iron Co-doped and boron-doped TiO2 nanoparticles." *Materials Chemistry and Physics* 112.1, 2008, 167-172.

[48] Chen, Daimei, et al. "Effects of boron doping on photocatalytic activity and microstructure of titanium dioxide nanoparticles." *Industrial & Engineering Chemistry Research* 45.12, 2006, 4110-4116.

[49] Su, Yaling, et al. "Preparation and visible-light-driven photoelectrocatalytic properties of boron-doped TiO_2 nanotubes." *Materials Chemistry and Physics* 110.2-3, 2008, 239-246.

[50] Quesada-González, Miguel, et al. "Interstitial Boron-Doped TiO_2 Thin Films: The Significant Effect of Boron on TiO_2 Coatings Grown by Atmospheric Pressure Chemical Vapor Deposition." *ACS applied materials & interfaces* 8.38, 2016, 25024-25029.

[51] Simsek, Esra Bilgin. "Solvothermal synthesized boron doped TiO_2 catalysts: photocatalytic degradation of endocrine disrupting compounds and pharmaceuticals under visible light irradiation." *Applied Catalysis B: Environmental* 200, 2017, 30

[52] Siuzdak, Katarzyna, et al. "Thin layer of ordered boron-doped TiO2 nanotubes fabricated in a novel type of electrolyte and characterized by remarkably improved photoactivity." *Applied Surface Science* 357, 2015, 942-950.

[53] Zaleska, Adriana. "Doped-TiO_2: a review." *Recent patents on engineering* 2.3, 2008, 157-164.

[54] Xu, Yi-Jun, Yangbin Zhuang, and Xianzhi Fu. "New insight for enhanced photocatalytic activity of TiO_2 by doping carbon nanotubes: a case study on degradation of benzene and methyl orange." *The Journal of Physical Chemistry C* 114.6, 2010, 2669-2676.

[55] Shahrezaei, Fa, et al. "Preparation of multi-walled carbon nanotube-doped TiO_2 composite and its application in petroleum refinery wastewater treatment." *Desalination and Water Treatment* 57.31, 2016, pp.14443-14452.

[56] Nguyen, Khang Cao, Minh Phan Ngoc, and Minh Van Nguyen. "Enhanced photocatalytic activity of nanohybrids TiO_2/CNTs materials." *Materials Letters* 165, 2016, 247-251.

[57] Xing, Zheng, et al. "On the engineering part of solar hydrogen production from water splitting: photoreactor design." *Chemical Engineering Science* 104, 2013, 125-146.

[58] Minggu, Lorna Jeffery, Wan Ramli Wan Daud, and Mohammad B. Kassim. "An overview of photocells and photoreactors for photoelectrochemical water splitting." *International journal of hydrogen energy* 35.11, 2010, 5233-5244.

[59] Maeda, Kazuhiko, and Kazunari Domen. "Photocatalytic water splitting: recent progress and future challenges." *The Journal of Physical Chemistry Letters* 1.18, 2010, 2655-2661.

[60] Dai, Ke, et al. "Multiwalled carbon nanotube-TiO 2 nanocomposite for visible-light-induced photocatalytic hydrogen evolution." *Journal of Nanomaterials* 2014, 2014, 4.

[61] Abdulrazzak, Firas H., and Falah H. Hussein. "Photocatalytic Hydrogen Production on Nanocomposite of Carbon Nanotubes and TiO2." *Journal of Physics: Conference Series*. Vol. 1032. No. 1. IOP Publishing, 2018.

[62] Carmichael, Penelope, et al. "Atmospheric pressure chemical vapour deposition of boron doped titanium dioxide for photocatalytic water reduction and

oxidation." *Physical Chemistry Chemical Physics* 15.39, 2013, 16788-16794.

[63] Carver, C. et al. “Modelling and Development of Photoelectrochemical Reactor for H 2 Production.” *International Journal of Hydrogen Energy* 37, 2012, 2911–2923.

[64] Chehade, Ghassan et al. Experimental investigation and analysis of a new photoelectrochemical reactor for hydrogen production. International Journal of Hydrogen Energy, 43(27), 2018, 12049–12058.

[65] Jeong, Jae-Hun, et al. "Boron-doped TiO2 anode materials for high-rate lithium ion batteries." *Journal of Alloys and Compounds* 604, 2014, 226-232.

[66] Demir, Murat E. *Experimental investigation of an integrated solar driven wastewater treatment system for trigeneration applications*. 2018. University of Ontario Institute of Technology, PhD thesis. https://ir.library.dc-uoit.ca/handle/10155/958

[67] Akhavan, Omid, et al. "Visible light photo-induced antibacterial activity of CNT–doped TiO 2 thin films with various CNT contents." *Journal of Materials Chemistry* 20.35, 2010, 7386-7392.

[68] Gamry Instuments. "Reference 3000™, Potentiostat/Galvanostat/ZRA Operator’s Manual." *Revision* 6 (2012): 988-00014.

Available: <https://www.gamry.com/assets/Uploads/Reference-3000-Operators-Manual.pdf>. Accessed: Jan 5, 2019.

[69] Zhang, Fang, et al. "Reference and counter electrode positions affect electrochemical characterization of bioanodes in different bioelectrochemical systems." *Biotechnology and bioengineering* 111.10, 2014, 1931-1939.

[70] Elgrishi, Noémie, Kelley J. et al. "A Practical Beginner’s Guide to Cyclic Voltammetry." *Journal of Chemical Education* 95, no. 2, 2017, 197-206.

[71] Cole-Parmer. pH reference half-cell, Ag/AgCl fill, glass body. Available: (https://www.coleparmer.ca/i/cole-parmer-ph-reference-half-cell-ag-agcl-fill-glass-body/0599060). Accessed: Jan. 5, 2019.

[72] Gamry Instruments. Gamry Reference 3000 Potentiostat/Galvanostat/ZRA: Specifications, 2017. (https://www.gamry.com/potentiostats/reference-3000/). Accessed: June 10, 2017.

[73] OAI. Trisol Class AAA, Standard Solar Simulator (TSS) Data Sheet, 2013. Available: (http://www.oainet.com/oai-solarsimulator-pp.html). Accessed: Apr. 13, 2015.

[74] Santangelo, Patrick G., Gordon M. Miskelly, and Nathan S. Lewis. "Cyclic voltammetry at semiconductor photoelectrodes. 1. Ideal surface-attached redox couples with ideal semiconductor behavior." *The Journal of Physical Chemistry* 92.22, 1988, 6359-6367. DOI: 10.1021/j100333a036.

[75] Orazem, Mark E., and Bernard Tribollet. *Electrochemical impedance spectroscopy*. Vol. 48. John Wiley & Sons, 2011. Online ISBN:9780470381588.

[76] Lvovich, Vadim F. *Impedance spectroscopy: applications to electrochemical and dielectric phenomena*. John Wiley & Sons, 2012.

[77] Bicer, Yusuf, and Ibrahim Dincer. "Electrochemical impedance spectroscopic assessment and analysis of a newly developed photoelectrochemical cell." *Chemical Engineering and Processing: Process Intensification* 117, 2017, 141-153.

[78] Andreasen, Søren Juhl, Jakob Rabjerg Vang, and Søren Knudsen Kær. "High Temperature PEM Fuel Cell Performance Characterisation with CO and CO_2 Using Electrochemical Impedance Spectroscopy." *International Journal of Hydrogen Energy* 36.16, 2011, 9815–9830.

[79] Zhou, Jianwei, Mo Zhang, and Yongfa Zhu. "Preparation of visible light-driven gC zN4@ ZnO hybrid photocatalyst via mechanochemistry." *Physical Chemistry Chemical Physics* 16.33 (2014), 17627-17633.

[80] Pichat, Pierre, 2ed. *Photocatalysis: Fundamentals, Materials and Potential*. MDPI AG-Multidisciplinary Digital Publishing Institute, 2016.

[81] Hashimoto, Kazuhito, Hiroshi Irie, and Akira Fujishima. "TiO_2 Photocatalysis: A Historical Overview and Future Prospects." *Japanese Journal of Applied Physics, Part 1: Regular Papers and Short Notes and Review Papers* 44.12, 2005, 8269–8285.

[82] Lingane, Peter James, and Dennis G. Peters. "Chronopotentiometry." 1971.

[83] Acar, Canan, and Ibrahim Dincer. "Energy and exergy analyses of a novel photoelectrochemical hydrogen production system." *International Journal of Hydrogen Energy* 42, no. 52, 2017, 30550-30558.

[84] Bicer, Yusuf, and Ibrahim Dincer. "Performance assessment of electrochemical ammonia synthesis using photoelectrochemically produced hydrogen. " *International Journal of Energy Research* 41.14, 2017, 1987-2000.

[85] COMSOL Multiphysics® Modeling Software Version 5.3 2017.

[86] Ghosh, Sayantan. *Experimental investigation and analysis of a new light-based hydrogen production system*. 2014. University of Ontario Institute of Technology, Master thesis. UOIT library, https://ir.library.dc-uoit.ca/handle/10155/862

[87] Pinar, F. Javier, et al. "Characterization of HT-PEM membrane-electrode-assemblies." *High Temperature Polymer Electrolyte Membrane Fuel Cells*. Springer, Cham, 2016, 353-386.

[88] Zhang, Lan. *Numerical Simulation of Two-phase Flow Using the Level Set Approach*. 2014. (http://hdl.handle.net/10657/1683) University of Houston, PhD dissertation.